
Investigation of Weyl Semimetal Mn_3Ge

Dissertation

zur Erlangung des Doktorgrades der Naturwissenschaften

(Dr. rer. nat.)

der

Naturwissenschaftlichen Fakultät II

Chemie, Physik und Mathematik

der Martin-Luther-Universität

Halle-Wittenberg

vorgelegt von

Herrn Jibo Zhang

Gutachter:

Prof. Dr. Stuart S. P. Parkin

Prof. Dr. Georg Woltersdorf

Prof. Dr. Anastasios Markou

Tag der öffentlichen Verteidigung:

28.06.2024

Content

Abstract	v
1 Introduction.....	1
1.1 Dirac equation and Weyl equation.....	1
1.2 Berry curvature and Weyl semimetal.....	3
1.3 D0 ₁₉ hexagonal compound Mn ₃ Ge	10
2 Experimental methods.....	19
2.1 Homemade molecular beam epitaxy system Quince	19
2.1.1 Introduction of molecular beam epitaxy.....	19
2.1.2 Introduction of Quince system	23
2.2 Structure and composition analysis methods.....	25
2.2.1 Reflection high-energy electron diffraction	25
2.2.2 X-ray photoelectron spectroscopy	28
2.2.3 Quartz crystal microbalance	30
2.2.4 X-ray diffraction	32
2.2.5 Rutherford backscattering spectrometry.....	33
2.2.6 Atomic force microscope.....	33

2.2.7	Scanning tunneling microscope.....	34
2.3	Electrical and magnetic measurement methods.....	35
2.3.1	Physical property measurement system.....	35
2.3.2	Magnetic property measurement system.....	36
2.3.3	Spin torque ferromagnetic resonance	38
3	Sample preparation	47
3.1	Substrate and buffer layers.....	47
3.1.1	Substrate preparation	47
3.1.2	Buffer layer determination and calibration.....	54
3.2	Capping layers.....	58
3.3	Hexagonal D0 ₁₉ Mn ₃ Ge film.....	60
3.3.1	Perfect cut Mn ₃ Ge(0001) film	60
3.3.2	Offcut Mn ₃ Ge(0001) film.....	65
3.4	Device fabrication	66
3.4.1	Hall geometry lithography.....	66
3.4.2	ST-FMR geometry lithography	69
4	Transport and magnetic properties of D0₁₉ Mn₃Ge films	71
4.1	Transport measurement for AHE	71
4.1.1	Shunting effect from buffer layer	71

4.1.2	AHE measurement.....	72
4.2	Magnetic measurement	77
4.2.1	Magnetic measurement for essential magnetic property.....	77
4.2.2	ST-FMR measurement for SHE	80
5	Electrical manipulation of Mn₃Ge/Pt bilayer stack	87
5.1	Sample preparation.....	87
5.2	Magnetic switching measurement.....	89
5.3	The origin of the switching mechanism.....	97
6	Conclusion and outlook	101
	Bibliography	103
	List of Figures.....	109
	List of Tables	115
	Abbreviations	117
	List of publications.....	121
	Acknowledgments	123
	Curriculum Vitae	125
	Eidesstattliche Erklärung.....	127



Abstract

In this thesis, we prepare non-collinear antiferromagnetic Weyl-semimetal Mn_3Ge thin films by MBE method. The crystal structure and chemical composition of the film are characterized by *in-situ* RHEED, LEED, STM and XPS, along with the *ex-situ* AFM, XRD and RBS measurement. Measurements using PPMS, MPMS and ST-FMR reveal the unique magnetic and transport properties of the hexagonal Mn_3Ge film, which are due to the Kagome spin structure of the Mn atoms.

To investigate the possibility of the Mn_3Ge -based AF application, we fabricate the Hall bar devices based on the $\text{Mn}_3\text{Ge}/\text{Pt}$ bilayer structure via ultraviolet lithography and measure the electrical switching of the bilayer's Hall voltage in the absence of the external magnetic field. The observation can be explained by the seed SOT mechanism in the Mn_3Ge layer. This research provides another method of the electrical manipulation of the magnetic material and shows promise for AF spintronics.



1 Introduction

1.1 Dirac equation and Weyl equation

It is well known that materials, according to their electronic energy band structure, can be divided into metals and insulators. Recent studies have shown that insulators can be further subdivided into trivial insulators and topological insulators^[1]. Topological insulators exhibit completely different quantum phenomena and physical properties from those of trivial insulators, for example, topologically protected surface states, weak antilocalization, quantum QSHE, and QAHE, etc. Therefore, since its discovery, topological insulators have become an important research area in condensed matter physics and materials science^[2]. An essential property of topological insulators is that small perturbations do not affect their topology. This allows one to investigate the topological properties of the insulator. If the perturbation does not close the energy gap of the insulator, then the topological properties of the insulator remain unchanged^[3, 4].

In recent years, a special class of metallic systems has been discovered whose low-energy excitations can be described by the 2-component Dirac equation, which is also called the Weyl equation. Therefore, these material systems are named Weyl semimetals. Weyl semimetals have no energy gap but still have topologically nontrivial behavior^[5, 6].

In 1928, Dirac introduced the following description of the free electron relativistic fluctuation equation:

$$i \hbar \frac{\partial}{\partial t} \Psi = H \Psi,$$

$$H = -i \hbar c \boldsymbol{\alpha} \cdot \nabla + m c^2 \boldsymbol{\beta} = c \boldsymbol{\alpha} \cdot \mathbf{p} + m c^2 \boldsymbol{\beta}, \quad (1)$$

with $\boldsymbol{\alpha} = \begin{pmatrix} 0 & \boldsymbol{\sigma} \\ \boldsymbol{\sigma} & 0 \end{pmatrix}$ being the Pauli matrix; $\boldsymbol{\beta} = \begin{pmatrix} \mathbf{I} & 0 \\ 0 & -\mathbf{I} \end{pmatrix}$ and $\mathbf{I} = \begin{pmatrix} 1 & 0 \\ 0 & 1 \end{pmatrix}$ being 2×2 identity matrix; \mathbf{p} being momentum operator.

In addition to its wide application in particle physics, the Dirac equation (1) can also be used to describe the low-energy excitation behavior of several condensed matter systems, which are called Dirac material systems. Several Dirac material systems have been discovered, such as graphene, monolayer boron nitride, high T_c copper oxide d-wave superconductors, topological insulators, etc. In the Dirac material system, the electron is defined by the Bloch state with quasi-momentum \mathbf{p} and energy $E(\mathbf{p})$. The Dirac equation can only describe the low energy excitation near certain points in the Brillouin zone, not the excitation behavior of the whole Brillouin zone. Unlike the Dirac equation used in particle physics in which c is the speed of light, in the Dirac equation of the Dirac material system, c is the Fermi velocity of the system. Therefore, this equation does not satisfy the Lorentz invariance.

A year after the Dirac equation was proposed, Weyl found that when the mass in the Dirac equation is zero, the equation can become as follows, which is called the Weyl equation:

$$i\hbar \frac{\partial}{\partial t} \Psi = H\Psi, H = c\boldsymbol{\sigma} \cdot \mathbf{p}. \quad (2)$$

The Weyl equation is a two-component wave equation satisfied by a particle with zero rest mass and 1/2 half-integer spin. Therefore, this particle is a fermion, and it satisfies the Pauli exclusion principle that two identical fermions cannot simultaneously occupy the same quantum state within a quantum system. These fermions are called Weyl fermions. In equation (2), we have $[\boldsymbol{\sigma}\mathbf{p}, H] = 0$, which means $\boldsymbol{\sigma} \cdot \mathbf{p}$ is conserved quantity, so is the spin projection along the momentum direction $\frac{\boldsymbol{\sigma}\cdot\mathbf{p}}{|\mathbf{p}|}$. Because $\frac{(\boldsymbol{\sigma}\cdot\mathbf{p})(\boldsymbol{\sigma}\cdot\mathbf{p})}{|\mathbf{p}|^2} = 1$, then $\frac{(\boldsymbol{\sigma}\cdot\mathbf{p})}{|\mathbf{p}|} = \pm 1$. The solutions of the Weyl equation are different: they have right-handed (1) and left-handed(-1) helicity, and thus chirality, respectively. This is the origin of the Weyl points, which can be considered as the cross points of 2 non-degenerate energy bands in 3D space^[5-7].

1.2 Berry curvature and Weyl semimetal

It is a typical particle physics perspective to view the excitation near the Weyl point as a massless fermion. From the condensed matter physics point of view, it can be considered as a singularity of Berry curvature. If the Berry curvature can be considered as a magnetic field in momentum space, then the Weyl point is the magnetic monopole corresponding to this magnetic field^[4].

Berry phase is a quantum phase effect arising in systems that undergo a slow, cyclic evolution. It has been widely used in many fields, such as condensed matter physics, particle physics, and optics.

Consider a Hamiltonian $H(\mathbf{R})$ that depends on parameters $\mathbf{R}_1, \mathbf{R}_2, \dots, \mathbf{R}_n$,

components of a vector $\mathbf{R}(t)$, it changes slowly in the parameter space. After a period $t = T$, the system goes along a closed path C, and it goes back to itself. In this process, the state of the system $|\psi(t)\rangle$ obeys the Schrödinger's equation

$$H|\psi(t)\rangle = i\hbar \frac{\partial}{\partial t} |\psi(t)\rangle. \quad (3)$$

Then introduce the instantaneous orthonormal basis $|n(\mathbf{R})\rangle$ from the eigenstates of $H(\mathbf{R})$ at each $\mathbf{R} = \mathbf{R}(t)$, it satisfies

$$H|n(\mathbf{R})\rangle = E_n(\mathbf{R})|n(\mathbf{R})\rangle. \quad (4)$$

According to the adiabatic theorem, if the system is in the state $|n(\mathbf{R}(0))\rangle$ at the beginning, it will evolve with H and reach the state of $|n(\mathbf{R}(t))\rangle$, apart from an additional phase

$$|\psi(t)\rangle = \exp\left\{\frac{-i}{\hbar} \int_0^t dt' E_n(\mathbf{R}(t'))\right\} \exp(i\gamma_n(t)) |n(\mathbf{R}(t))\rangle. \quad (5)$$

In which the first exponential is called the dynamical phase factor. In the second exponential, $\gamma_n(t)$ is unrelated to the path $\mathbf{R}(t)$ and it is not single-valued. By inserting the time-dependent wavefunction in equation (5), we can get

$$\dot{\gamma}_n(t) |n(\mathbf{R}(t))\rangle = i |\dot{n}(\mathbf{R}(t))\rangle = i \nabla_{\mathbf{R}} |n(\mathbf{R}(t))\rangle \dot{\mathbf{R}}. \quad (6)$$

Multiply it by $\langle \mathbf{R}(t) |$ from the left, then integral it along the path C in the parameter space, we can get

$$\gamma_n(t) = i \int_0^t \langle n(\mathbf{R}(t)) | \nabla_{\mathbf{R}} |n(\mathbf{R}(t))\rangle \dot{\mathbf{R}} dt$$

$$\begin{aligned}
&= i \oint_C \langle n(\mathbf{R}) | \nabla_{\mathbf{R}} | n(\mathbf{R}) \rangle d\mathbf{R} \\
&= \oint_C A_n(\mathbf{R}) d\mathbf{R}
\end{aligned} \tag{7}$$

In equation (7), $A_n(\mathbf{R})$ is a single-valued vector function at each vector position \mathbf{R} , obviously. It is called the Berry connection or the Berry vector potential.

At the beginning, we define the path C as a closed loop, so by applying the Stokes's theorem, we can transform the path integral into surface integral,

$$\gamma_n = \int \nabla_{\mathbf{R}} \times A_n(\mathbf{R}) d\mathbf{S}, \tag{8}$$

Where \mathbf{S} here is the surface expanded by the enclosed path C. The curl of the Berry connection, namely the Berry curvature, is defined as follows:

$$\Omega_n(\mathbf{R}) = \nabla_{\mathbf{R}} \times A_n(\mathbf{R}). \tag{9}$$

In fact, the Berry curvature can resemble the magnetic field in parameters space. Thus, the Berry connection can be treated as the analog of the magnetic vector potential, and the Berry phase as the analogue of magnetic flux.

By applying the Berry phase on the electron transports in crystalline solid described by Bloch's theorem, we can get the Berry curvature corrected motion equation of the electron, the element of AHE $\sigma_{\alpha\beta}$, the element of SHE $\sigma_{\alpha\beta}^y$ and the average velocity $v_n(\mathbf{k})$ is described as follows:

$$\sigma_{\alpha\beta} = -\frac{e^2}{\hbar} \sum_{m \neq n} \int_{BZ} \Omega_{n,\alpha\beta}(\mathbf{k}) \frac{d\mathbf{k}}{(2\pi)^3}$$

$$= -2e^2\hbar i \sum_{m \neq n} \int_{BZ} \left[\frac{\langle u_n | \hat{v}_\alpha | u_m \rangle \langle u_m | \hat{v}_\beta | u_n \rangle}{(E_n - E_m)^2} \right] \frac{d\mathbf{k}}{(2\pi)^3}, \quad (10)$$

$$\begin{aligned} \sigma_{\alpha\beta}^\gamma &= -\frac{e^2}{\hbar} \sum_{m \neq n} \int_{BZ} \Omega_{n,\alpha\beta}^\gamma(\mathbf{k}) \frac{d\mathbf{k}}{(2\pi)^3} \\ &= 2e\hbar i \sum_{m \neq n} \int_{BZ} \left[\frac{\langle u_n | \hat{J}_\alpha^\gamma | u_m \rangle \langle u_m | \hat{J}_\alpha^\gamma | u_n \rangle}{(E_n - E_m)^2} \right] \frac{d\mathbf{k}}{(2\pi)^3}, \end{aligned} \quad (11)$$

$$v_n(\mathbf{k}) = \frac{\partial E_n(\mathbf{k})}{\hbar \partial \mathbf{k}} + \frac{e}{\hbar} \mathbf{E} \times \boldsymbol{\Omega}_n(\mathbf{k}). \quad (12)$$

$$\mathbf{k} = \mathbf{q} + \frac{e}{\hbar} \mathbf{A}(t). \quad (13)$$

Here $\hat{v}_\alpha = \frac{\partial H}{\hbar \partial k_\alpha}$ is the α component of the velocity operator. u represents the wave function. The spin current operator $\hat{J}_\alpha^\gamma = \frac{1}{2} \left\{ \frac{\partial H}{\hbar \partial k_\alpha}, \hat{S}_\gamma \right\} = \frac{1}{2} \{ \hat{v}_\alpha, \hat{S}_\gamma \}$, where \hat{S}_γ is the γ component of the spin operator. \mathbf{q} is the crystal wave vector, also known as the quantum number of the state. \mathbf{k} is the gauge-invariant crystal momentum. E denotes the discrete eigenvalue of the system. \mathbf{E} is the electric field. Equation (10) can be explained that the $\sigma_{\alpha\beta}$ is the response of charge current in α direction when the field is in β direction. Similarly, equation (11) is the response of spin current (angular momentum) in α direction when the field is in β direction and the spin is in γ direction. In equation (12), it is evident that the second term is transverse to the electric field, which leads to a Hall current.

As the Berry curvature and spin Berry curvature directly originated from the band structure, they are compatible with the symmetry of the Hamiltonian. Next, we will perform the symmetrical analysis of the Berry curvature^[8].

If the system has the time reversal symmetry \hat{T} , electric field \mathbf{E} should maintain its sign under the operation \hat{T} , and the crystal momentum \mathbf{k} changes sign to $-\mathbf{k}$, velocity $v_n(\mathbf{k}) = -v_n(-\mathbf{k})$, $E_n(\mathbf{k}) = E_n(-\mathbf{k})$, from equation (11), we can get

$$\Omega_n(\mathbf{k}) = -\Omega_n(-\mathbf{k}). \quad (14)$$

If the system has spatial inversion symmetry \hat{P} , \mathbf{E} will change the sign under the operation \hat{P} , \mathbf{k} changes sign to $-\mathbf{k}$, $v_n(\mathbf{k}) = -v_n(-\mathbf{k})$, $E_n(\mathbf{k}) = E_n(-\mathbf{k})$, then

$$\Omega_n(\mathbf{k}) = \Omega_n(-\mathbf{k}). \quad (15)$$

As for the mirror-reflection symmetry \hat{m} on \mathbf{k} , \mathbf{E} and $v_n(\mathbf{k})$, it will change the signs of the components perpendicular to the mirror (parallel with the normal line of the mirror) and maintain the signs of the components parallel with it. As for the Berry curvature, its perpendicular-to-the-mirror components will keep its sign, and components parallel with the mirror will change the sign^[9].

As for the spin berry curvature $\Omega_n^s(\mathbf{k})$, similarly, if the system has the time reversal symmetry \hat{T} , $\Omega_n^s(\mathbf{k}) = \Omega_n^s(-\mathbf{k})$; under spatial inversion symmetry \hat{P} , $\Omega_n^s(\mathbf{k}) = \Omega_n^s(-\mathbf{k})$.

As mentioned above, the solution to the Dirac equation is with four components, so the Dirac point in the Dirac material must be the intersection of 4 energy levels. However, the solutions to the Weyl equation are referred to as the left- and right-handed Weyl spinors, each with two components, which means that the Weyl point in a WSM must be the intersection of two non-degenerate energy levels. For a material system with both spatial inversion symmetry and time reversal symmetry,

each energy band is at least two-component degenerated, so the intersection of these energy bands is at least four-component degenerated. Therefore, no WSM materials shall exist in this system. To discover WSMs, one needs to break either the TRS or SIS^[6].

In a WSM, the conduction and valence bands cross each other linearly through nodes in 3D space called Weyl points. A pair of Weyl points with opposite chiralities(+1 or -1) act as sink or source of the Berry curvature $\Omega_n(\mathbf{k})$. Suppose a material breaks TRS in ferromagnets with possible tilted moments. In that case, the net Berry phase accumulated in the 2D k plane between a pair of Weyl points should induce a non-zero Chern number $C = 1$ with a quantized AHE. Meanwhile, the Berry phase is zero in other planes with $C = 0$. Moreover, $\Omega_n^s(\mathbf{k})$ remains even under SIS, so the system can have non-zero SHE^[10-13]. This should be a pure topological effect caused by the band structure as the bulk Fermi surface vanishes at the Weyl point. On the boundary, topological edge states exist at edges of 2D planes with $C = 1$ and disappear at edges of other planes in which the separation points between two types of planes are these Weyl points. Consequently, the Fermi surface, an energy contour crossing the Weyl points, exhibits an unclosed path that starts from one Weyl point and ends at the other with opposite chirality, which is called a Fermi arc. The Fermi arc is apparently different from the Fermi surface of a TI, an ordinary insulator, or a normal metal. Therefore, the identical Fermi arc of the WSMs offers strong evidence for identifying a WSM by using surface analysis techniques such as ARPES. Magnetic Heusler material GdPtBi and YbMnBi₂ belong to this group of WSM^[14].

If SIS is broken in a Weyl semimetal and TRS remains, at least two pairs of Weyl points may exist, where TRS transforms one pair to the other by reversing the chirality. The Fermi arc should still show up. However, the AHE should not exist in this material because the Berry phase $\Omega_n(\mathbf{k})$ contributed from two Weyl pairs cancel each other. Instead, an intrinsic SHE can show up, which can be considered as the spin-dependent Berry phase $\Omega_n^s(\mathbf{k})$ remains even under the TRS. Transition-metal pnictides such as TaAs and transition-metal dichalcogenides such as WTe₂ and MoTe₂ belong to this group of material^[15, 16].

WSMs can also be classified into type I, which respects Lorentz symmetry, and type II, which does not. The Transition-metal pnictides of WSMs exhibit ideal Weyl cones in the bulk band structure and belong to the type-I class in which the Fermi surface shrinks to a point at the Weyl point. In type-II WSMs, the Weyl cone exhibits strong tilting so that the Weyl point is the contact point between an electron pocket and a hole pocket in the Fermi surface. Type-II WSMs are expected to show very different properties from type-I WSMs, such as anisotropic chiral anomaly depending on the current direction and AHE.

Another important consequence of the 3D Weyl band structure is that WSMs display the chiral anomaly effect. In WSMs, the chiral anomaly is predicted to lead to a negative MR, which is due to the chiral zero modes of the Landau levels of the 3D Weyl cones and the suppressed backscattering of electrons of opposite chirality. The negative MR is expected to reach the largest value when the nonorthogonal magnetic field \mathbf{B} is parallel to the electric field \mathbf{E} , because the $\mathbf{B} \perp \mathbf{E}$ component should show a positive MR induced by the Lorentz force. In addition to the negative

MR, the chiral anomaly is also predicted to induce nonlocal transport and optical properties.

Recently, Mn_3X family of materials (where $X = Sn, Ge, \text{ and } Ir$), which exhibit noncollinear AFM phases even at room temperature, have been reported to show both large AHE and SHE in the system with broken TRS. Calculations have been made to prove the existence of Weyl fermions for Mn_3Ge and Mn_3Sn compounds and the Fermi arcs on the surface by *ab initio* band structure and Berry phase calculations and yet to be proved in experimental investigations such as ARPES. These studies reveal large and anisotropic values of both the intrinsic AHE and SHE of the Mn_3X compounds^[7, 17, 18].

1.3 D0₁₉ hexagonal compound Mn_3Ge

The Heusler alloy was first discovered in 1903 when Heusler reported that by adding *sp* elements (Al, In, Sn, Sb, or Bi) in Cu-Mn alloy, the new alloy Cu_2MnAl becomes ferromagnetic at room temperature even though there are no ferromagnetic elements in the alloy. The crystal structure of Cu_2MnAl alloy remained unclear for a long time. In 1929 Potter ran the X-ray measurements on Cu-Mn-Al alloy and discovered that the atoms of this alloy form a face-centered cubic superlattice. Later, Bradley and Rodgers investigated the Cu-Mn-Al alloy system in detail by X-ray and anomalous scattering. They found out that the composition, chemical order, and magnetic properties have a close relationship with each other, and they all contribute to the unique ferromagnetic behavior. It is found that the Heusler structure is formed from the ordered combination of two binary B2 compounds, XY and XZ, where X and Y are transition metals, with X

being more electropositive than Y, and Z is a main group element. Both compounds share the simple CsCl type crystal structure, for instance, CoMn and CoAl can form Co₂MnAl alloy in an X₂YZ format. Thus, the ability of combining two B2 structure compounds indicates the possibility of forming new Heusler compounds. This L2₁ structure X₂YZ Heusler compound is called full Heusler alloy. It was later discovered that it is also possible to leave one X position of the four interpenetrating face-centered cubic sublattices unoccupied. This C1_b structure compounds are called half Heusler alloys.

One unique property of the Heusler class of compounds is that their crystal structure is quite stable when a wide variety of elements are substituted on any of the three distinct atomic sites X, Y, and Z within the unit cell. Today, the Heusler compounds material family consists of more than 1000 compounds with different compositions and lattice structures. Heusler compounds can be semiconducting, metallic, superconducting, or half-metallic and show a wide range of exciting properties, such as ferromagnetism, antiferromagnetism, thermoelectricity, spin calorificity, and high spin polarization. Moreover, during the past decade, Heusler compounds have been found to exhibit, beyond the conventional properties listed above, several topological properties, including topological superconductivity, Berry curvature driven non-zero AHE, and SHE. Above all, Heusler compounds can potentially be used in many important technological fields^[19].

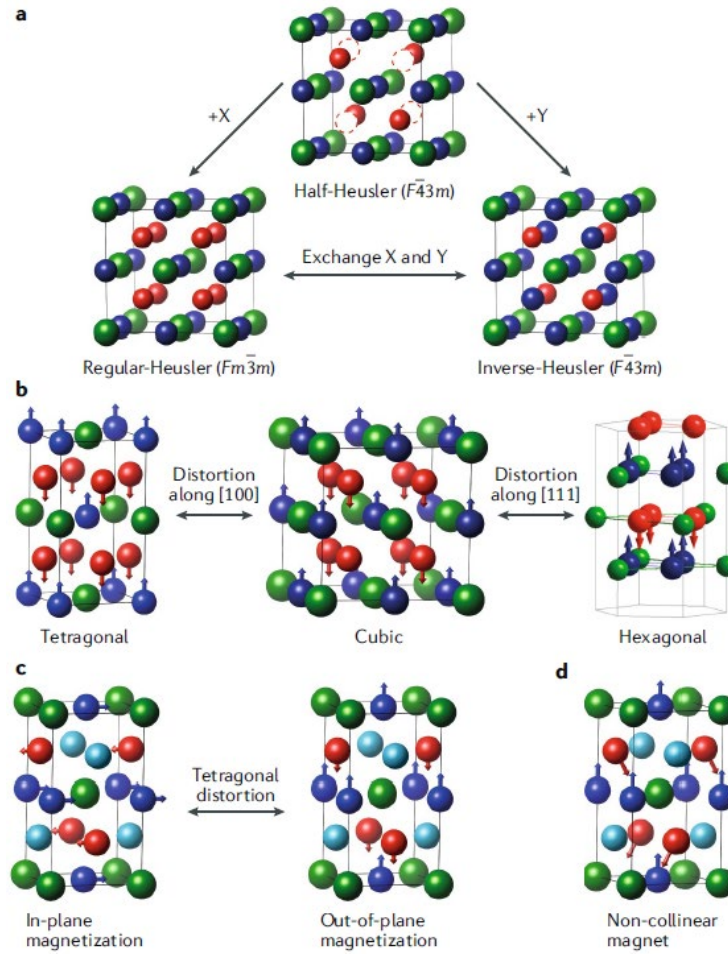


Figure 1: (a) Basic structure of half Heusler alloy (XYZ) and full Heusler alloy (X_2YZ). X (red spheres) and Y (blue spheres) are transition metals, with X being more electropositive than Y, and Z (green spheres) is a main group element. Full Heusler alloy could be one of the two types: regular Heusler and inverse alloy. (b) Illustration of the structure deformation from general cubic structure, by compression or elongation either along the [100] axis of cubic structure to tetragonal lattice with $I4/mmm$ space group, or along the [111] axis to a hexagonal structure with the $P6_3mc$ space group. (c) Due to the large magnetocrystalline anisotropy in tetragonal Heuslers, the preferred magnetization orientation can either be in-plane or out-of-plane by the sign of the magnetocrystalline anisotropy energy. The light blue spheres represent a 3d, 4d, or 5d element that is introduced to alter the strength of the magnetocrystalline anisotropy. (d) for certain value of the anisotropy energy, the spin can form in a non-collinear order. Adapted from reference^[4]

The Heusler compound Mn_3Ge can be crystalized in tetragonal, hexagonal and cubic structures, depending on the annealing temperature. When annealed at a high temperature 1073K for four days, polycrystalline ingots of Mn_3Ge were synthesized by repeated inductive melting of target amounts of the high-purity elements in a high-purity argon atmosphere. Meanwhile, the hexagonal structure

can be transformed to a face-centered tetragonal structure by annealing for a long time at 723 K^[20].

The cubic phase of Mn₃Ge belongs to the X₂YZ full Heusler structure (Fm $\bar{3}$ m). Mn atoms (in X and Y position) and Ge atoms (in Z position) occupy the (1/4, 1/4, 1/4), (1/2, 1/2, 1/2) and (0, 0, 0) sites, respectively. The magnetic moments of Mn in the X position and in Y position orient oppositely. The tetragonal phase (I4/mmm) has an elongated c axis and shortened a axis compared to the cubic lattice. It can be obtained by tetragonal distortion of the cubic phase along the z direction^[9]. The magnetic order in tetragonal phase, similar to the cubic phase, is ferrimagnetic, with magnetic moment μ_B as large as 1.00eV.

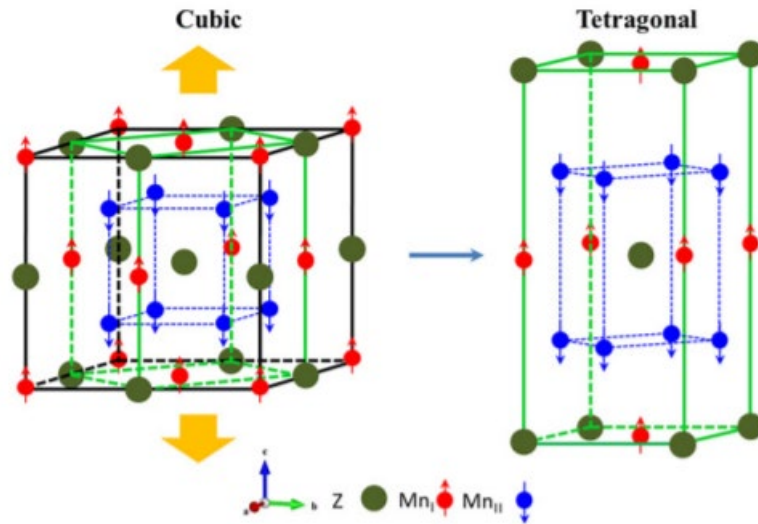


Figure 2: Illustration of phase transition from cubic to tetragonal structure. Adapted from literature^[21].

The phase transition between the hexagonal and tetragonal phases in Mn₃Ge has been reported in experiment. However, by calculations, it is believed that the

Mn_3Ge in tetragonal phase will first be transformed into the cubic structure, which acts as an intermediate phase during the transition and then to the hexagonal phase.

If the cubic lattice is projected along the diagonal direction, one obtains a triangular lattice. To recover a hexagonal phase, four atomic layers, including three Mn layers and one Ge layer, need to be compressed into one layer. However, because this Ge atom overlaps with one Mn atom, it is impossible to realize the transition by one projection. To host the additional Mn atoms inside a layer, the honeycomb lattice for Mn should change into a Kagome lattice.

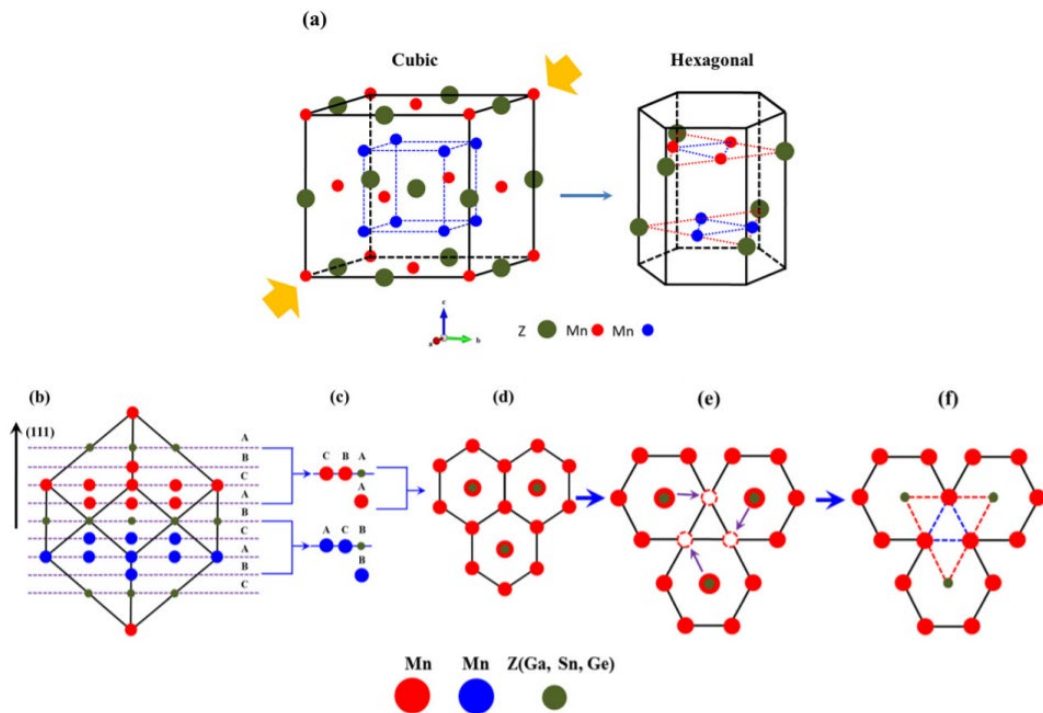


Figure 3: (a) Illustration of phase transition from tetragonal to hexagonal structure. (b)-(f) The projection from the cubic-to-hexagonal structures. Adapted from literature^[1, 21].

First-principles calculations were made to investigate the structural stability and magnetic properties of the hexagonal, cubic, and tetragonal phases of Mn_3Ge . The Tetragonal phase is expected to have the lowest total energy among the three phases,

and the hexagonal phase has the highest total energy. This calculation indicates that it would be challenging to prepare hexagonal phase Mn_3Ge bulk or films^[9].

Hexagonal Mn_3Ge ($D0_{19}$) exhibits triangular antiferromagnetic spin structure with ordering temperature from 365K to 400K, with lattice constant $a=5.34 \text{ \AA}$ and $c=4.32 \text{ \AA}$. One hexagonal unit cell comprises 2 Mn layers stacked along the c axis. In each Mn layer, Mn atoms form the Kagome lattice, with Ge atoms staying in the center of Mn-formed hexagon. Non-collinear antiferromagnetic spin texture exists with neighboring Mn spin moments lying with 120° angle between each other in ab plane, confirmed by neutron diffraction experiment. And the spin texture can be rotated by external magnetic field, with around $0.005 \mu_B/\text{Mn}$ zero field moment and 20 Oe coercive field at 3K when the field lies in ab plane.

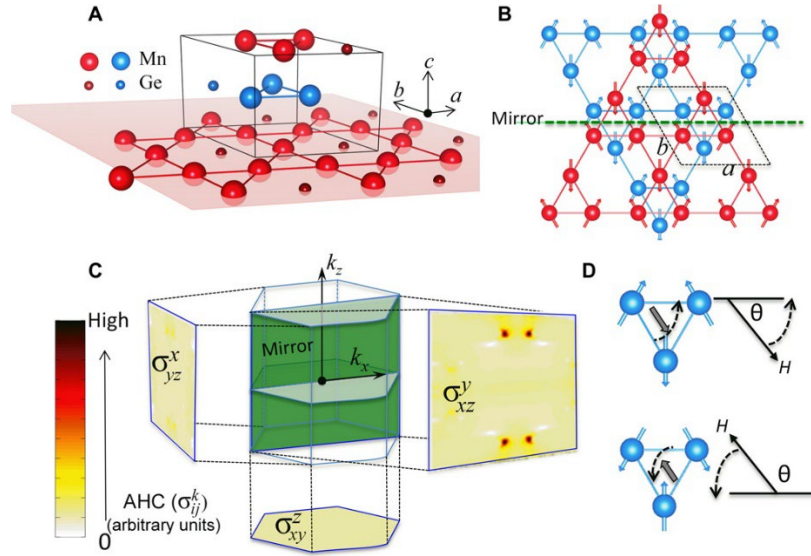


Figure 4: (a) Crystal structure showing the two layers of Mn-Ge atoms stacked along the $c(z)$ axis. (b) Calculated 120° antiferromagnetic configuration in the $z = 0$ and $z = c/2$ planes, respectively. The green dashed line indicates the mirror plane (that is, the xz plane). (c) First Brillouin zone and momentum-dependent AHC. (d) Illustration of the rotation of the triangular spin structure with an IP field. Adapted from literature^[18].

There have been papers focusing on the AHE of the Mn_3Ge single crystalline and

polycrystalline bulk samples, along with the polycrystalline films. Large Anomalous Hall conductivity driven by Berry curvature has been reported. σ_{ij}^K is the Anomalous Hall conductivity tensor representing the Berry curvature of all occupied electronic states integrated over the direction k_k when current flows along k_j direction and Hall voltage is measured along k_i direction. Meanwhile, the external field is applied along the k direction. In the Mn_3Ge system, the Berry phase $\Omega_n(\mathbf{k}) = \Omega_n(-\mathbf{k})$ if only considered the TRS broken. By adding the mirror reflection symmetry, $\Omega_n(\mathbf{k})$ components which are perpendicular to the mirror will maintain, parallel to the mirror components will vanish. As for the spin Berry curvature, $\Omega_n^s(\mathbf{k}) = \Omega_n^s(-\mathbf{k})$ under SIS and mirror reflection. Thus, due to the mirror reflection of the 2 Mn layers in one unit cell with respect to the k_x - k_z plane in momentum space added by an extra translation by $c/2$ along the c axis, and the TMR broken nature, the components of σ_{ij}^k vanish if they are parallel to the mirror plane. Noted that $x \parallel [11 - 20]$, $y \parallel [10 - 10]$ and $z \parallel [0001]$. Then it is obvious that $\sigma_{xy}^z, \sigma_{yz}^x$ should be exact zero, σ_{xz}^y should have nonzero value as it is perpendicular to the xz mirror plane. However, the weak in-plane symmetry broken, owing to the tiny IP residual moment, seems to induce tiny effects in the transport measurement. However, it gives rise to a perturbation of the mirror symmetry, for example, shifting slightly the mirror image of a Weyl point from its position expected, as we will see in the surface states of Mn_3Ge . Thus, it is possible for $\sigma_{xy}^z, \sigma_{yz}^x$ to show tiny non-zero value.

The magnitude of Anomalous Hall conductivity has been reported in single crystal bulk sample to be around $500 \text{ (ohm}\cdot\text{cm)}^{-1}$ at 2K and remains around 50

$(\text{ohm}\cdot\text{cm})^{-1}$ even at room temperature^[7].

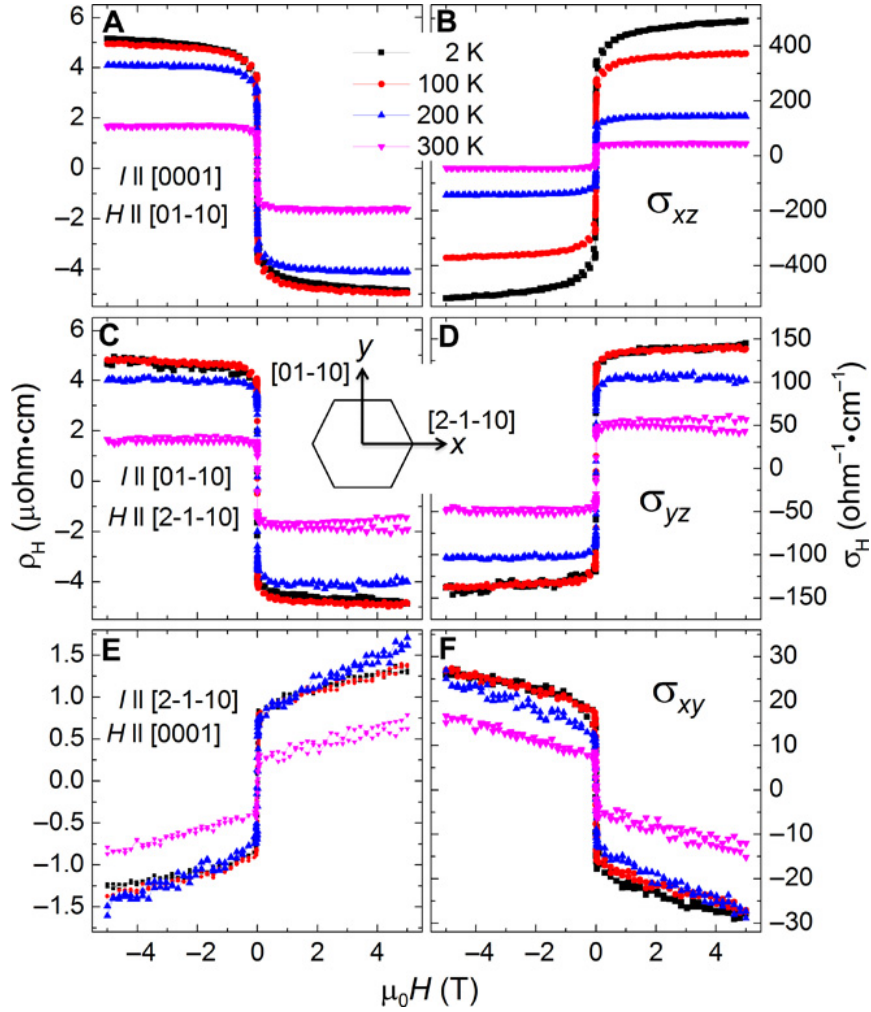


Figure 5: (A to F) Hall resistivity and Hall conductivity as a function of magnetic field measured at four representative temperatures for three different current and magnetic field configurations. Adapted from literature^[18].

As for the SHE, only one paper has been published so far investigating the epitaxial Mn_3Ge film grown by magnetron sputtering. The spin-mixing conductance is 90.5 nm^{-2} at the $\text{Py}/\text{Mn}_3\text{Ge}$ interface and the spin-Hall angle in Mn_3Ge is estimated to be about eight times of that in Pt. These results are consistent with the theoretical prediction of a large spin Hall conductivity in Mn_3Ge sample^[22].

According to the theoretical calculation^[7], to measure the AHE in Mn_3Ge , one

needs to set the current and measure the Hall voltage in xz plane. As for SHE, the charge current and spin current should be set in xy plane. Note that xy plane is the Kagome spin structure plane and z is perpendicular to this plane. In other words, the preparation of $\text{Mn}_3\text{Ge}(0001)$ film is essential for SHE detection. However, to measure AHE, the Mn_3Ge film need to expose the Kagome spin structure with component along the normal axis of the film, thus an offcut $\text{Mn}_3\text{Ge}(0001)$ film might be helpful in this situation.

To further investigate the interesting properties and spintronics application of hexagonal Mn_3Ge system, we need to have high-quality Mn_3Ge films.

Next, I will introduce the MBE system I use for the film deposition and the experimental methods I use during the research.

2 Experimental methods

2.1 Homemade molecular beam epitaxy system Quince

2.1.1 Introduction of molecular beam epitaxy

Molecular beam epitaxy (MBE) technology was invented by Arthur J. R. and Cho A. Y. of Bell Laboratories and it is an advanced thin-film material preparation method that has made a great contribution to the epitaxial growth of semiconductor GaAs films^[23]. After more than half a century of development, MBE technology has been widely used in the semiconductor industry and has played a vital role in the development of information science.

Epitaxy is defined as the process of growing single-crystal films layer by layer in the direction of the crystallographic axis of the substrate material by choosing the suitable substrate and under appropriate conditions. The widely used epitaxy methods include gas phase epitaxy, liquid phase epitaxy and molecular beam epitaxy. As one of the most important tools for growing high-quality thin films today, molecular beam epitaxy is a special coating process that enables precisely controlled growth of single-crystal thin films and nanostructures at the atomic scale^[24].

A typical MBE system consists of a vacuum pumping system, an ion gauge vacuum meter, some evaporation cells, a sample handling station (so called manipulator), a reflective high-energy electron diffractometer (RHEED), Quartz crystal microbalance (QCM), residual gas analyzer and should be operated under ultra-high vacuum (UHV) environment.

The pumping system of the MBE system is crucial for the UHV of the chamber. With the combination of TMP, TSP, IGP and an additional cooling shroud, the chamber can easily reach 10^{-10} mbar after efficient baking out of the chamber.

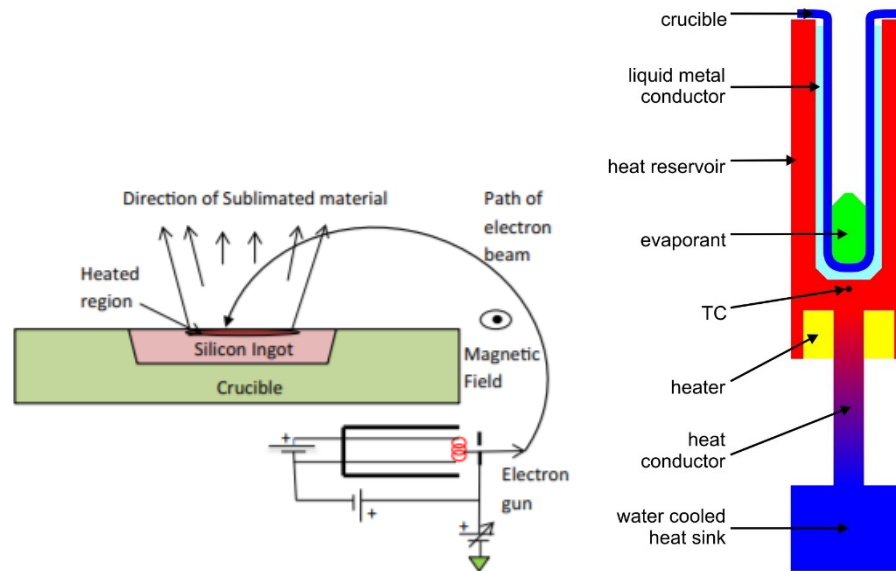


Figure 6: Schematic of a typical electron beam evaporator and K-cell evaporator. From literature^[24].

The most important part of an MBE system is the evaporation source. There are many different kinds of evaporation source used in the MBE system, such as plasma source for gas atoms evaporation, organic evaporation sources, thermal cracker, doping sources, etc. However, by means of heating the material, the sources can be divided into 2 kinds. One is called the Knudsen cell which uses the resistance heating method to heat the crucible with a heating filament. The material is filled in the crucible. When the temperature is high enough, the material will be vaporized and come out of the sources. By monitoring the crucible temperature by a C- or K-type thermocouple and controlling the heating power source with PID controller, one can get a stable beam of the material. The other kind is called electron beam evaporator, which uses a tungsten filament to generate electrons moving from the

filament to the material rod or metal crucible by applying high voltage in between. When the material is hot enough, it will vaporize and come out of the source directionally. By controlling the flux of the material beam, it is pretty convenient to have a stable and continuous beam for deposition. Most of the evaporation source is equipped with a shutter, which makes it easier to control the thickness of the films.

In general, the material is heated in an evaporation source to form atomic or molecular beams in the UHV chamber, which further moves out from the evaporation source in a directional way to the substrate surface. The molecules (atoms or ions) that "hit" the substrate in the beam are involved in epitaxial growth, and the size of the beam is determined by the geometry and temperature of the evaporation source, which is challenging to be scattered under UHV and is easy to achieve precise control of the growth rate, chemical composition, etc. While the other kind of the beam which is not "caught" by the substrate, thus got pumped away from the substrate, which does not affect the film growth process, this is also called desorption. At the right substrate temperature, different atoms nucleate/react and form crystals on the substrate, thus enabling the epitaxial growth of the film^[25].

MBE growth has the following advantageous features^[26]: (1) the entire growth process is carried out in an UHV environment, avoiding the interference of external impurities, and through precise control of chemical ratios, the high purity and high quality samples can be prepared; (2) film growth can be precisely controlled at the atomic scale; (3) superlattices can be prepared to achieve artificial manipulation of energy band engineering; (4) growth is generally carried out at a lower temperature regime for the

substrate, avoiding defects caused by high temperature of the substrate and doping effects caused by interdiffusion between substrate and epitaxial layers; (5) the growth process is accompanied by material gas-solid phase transition, and the epitaxy is subject to the joint action of thermodynamics and molecular dynamics, which is essentially a non-equilibrium growth process, thus it is possible to obtain the crystal structure and composition that cannot be prepared by other deposition methods; (6) an MBE system is preferably combined with *in-situ* UHV analysis technology such as RHEED, STM, XPS and ARPES easily to explore the properties of one material without breaking the vacuum.

The material beam flow J can be calculated as^[27]

$$J = \iint_{\bar{v}, \Omega} n(P, T) d\bar{v} d\Omega = \frac{\sqrt{2}}{8\sqrt{\pi}} \cdot \frac{S \cdot \cos \theta}{L^2} \cdot \frac{P}{\sqrt{mK_B T}} = C \cdot \frac{P}{\sqrt{T}} \quad (16)$$

Where L is the linear distance from the substrate and evaporator outlet surface, θ is the angle between the normal of substrate plane and material outlet direction, S is the size of the outlet, m is the molecule mass of the material from the evaporator, P is the saturated vapor pressure of this material and T is the source temperature. For a certain MBE system C is a constant, the only parameters left to determine the beam flow are saturation vapor pressure and temperature. For different materials, the relationship between P and T can be found in the corresponding literature, and it is possible to roughly estimate the temperature required to have an appreciable molecular beam flow, however, theoretically.

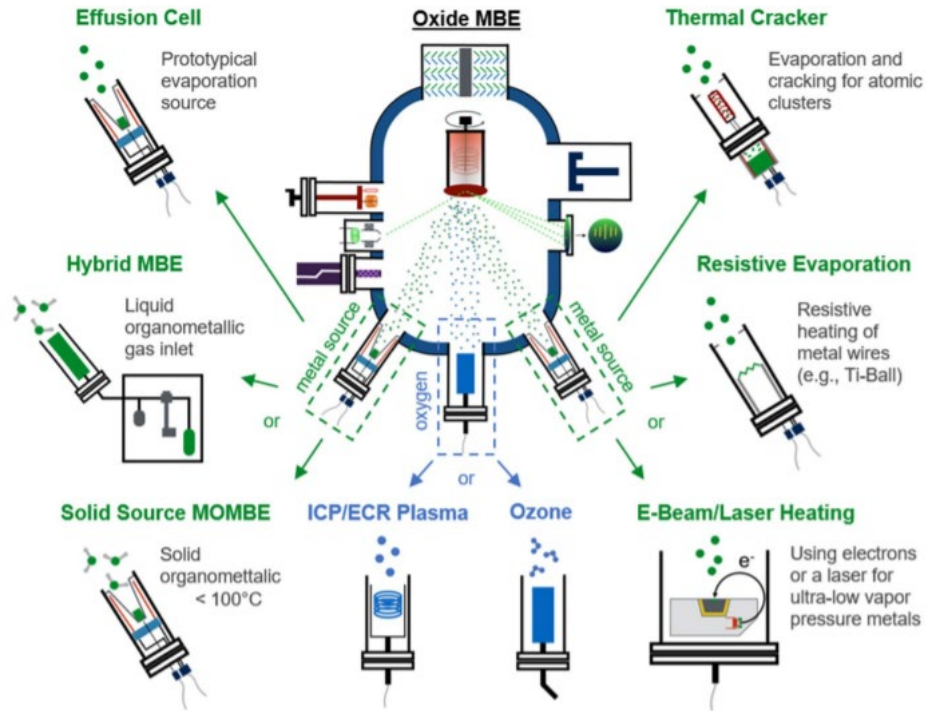


Figure 7: Schematic of the various common methods of delivering metal sources in oxide MBE. Adapted from literature^[28].

To achieve high-quality film deposition, it is favorable for the growth rate of the film to be as slow as possible, and more importantly, choose the suitable substrate or add favorable buffer layers between the film and substrate in order to achieve the high-quality epitaxy growth.

2.1.2 Introduction of Quince system

The Quince system is a homemade MBE system combined with an *in-situ* XPS. There are two DN40CF 4-pocket EBEs, one DN40CF K-cell evaporator (with Sn) and one DN63CF 2-pocket K-cell (filled with Mn and Ge) evaporator mounted on the system which make it possible to have 11 different kinds of materials in one deposition chamber. QCM can be used to monitor the growth rate of each source. TSP, IGP and TMP are used in this system in order to achieve 1.0×10^{-11} mBar as

base vacuum pressure and lower than 3.0×10^{-10} mBar during film deposition. The RGA can help analysis the chamber residual gas in order to achieve the UHV after bake-out and more importantly, used for vacuum leak test.

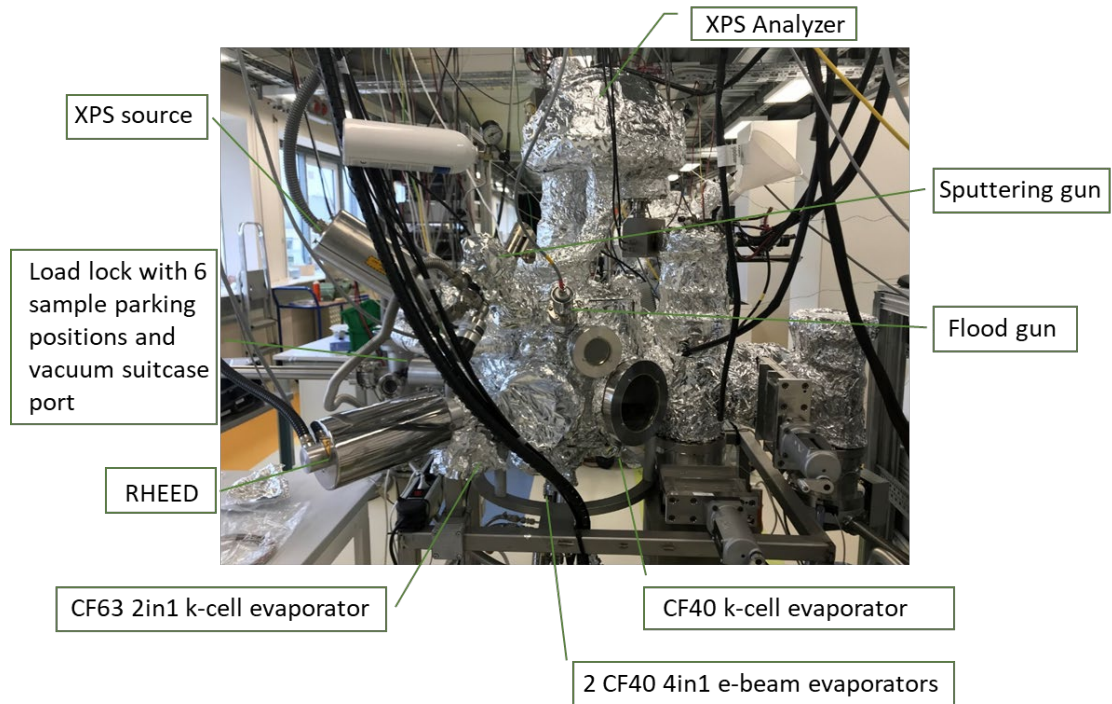


Figure 8: The picture of the Quince MBE system.

The manipulator in this chamber can easily reach the temperature as high as 700°C and as low as -100°C with the help of resistive heating and cooling pipes around the sample stage. The sample stage on the end of the manipulator is designed for flag shape sample holder. An *in-situ* RHEED system is attached to monitor the sample quality. The *in-situ* XPS system along with the sputter gun and flood gun is used to scan the surface of the sample to analyze the composition of the film. Moreover, a load lock system with 6 sample parking slots and a port for vacuum suitcase is attached to the UHV.

The typical procedure of MBE chamber maintenance is: (1) Vent the chamber to replace the broken filament or refill the material. (2) Keep the maintenance time as short as possible and pump the chamber to vacuum as soon as possible. (3) With the TMP

working overnight, the chamber vacuum should reach 10^{-8} mbar range. Run a leak test to ensure no leak before chamber bake out. (4) Check the electric connection of the EBE filament and material circuit by ramping the source emission current around 3mA. Also, check other functions of the chamber if necessary. Then, turn on the TSP. (5) Blow off the cooling water circuit of XPS and evaporators. Take the unbackable parts off from the chamber. (6) Cover the chamber with aluminum foil and mat. Start the bake out process. The setting of the baking out temperature depends on the material in the chamber. (7) Keep the TMP and TSP on during the bake out. Degas the vacuum gauge, TSP filament every 8h. (8) When the chamber vacuum didn't change in 8h, stop the bake out. The typical baking time for Quince chamber is 72h. (9) Degas the EBE filament, vacuum gauge and TSP filament while the chamber is still hot. (10) Run the leak test again on the next day, then degas other parts of the chamber, for example XPS, RHEED, if there is no leak. (11) Degas the K-cell source and E-beam material. (12) Check the purity of the source material by depositing film on a random substrate and check the XPS of the film. Keep degassing until XPS shows pure material peak without oxygen and other possible residual peaks. (14) Run the QCM measurement to determine the growth rate of the material. Now the chamber is ready for normal use.

2.2 Structure and composition analysis methods

2.2.1 Reflection high-energy electron diffraction

RHEED can be used to monitor thin film growth (even for sub-monoatomic layers), in which an electron beam with an energy of 10-100k eV strike the sample at a very small angle relative to the sample surface ($1^{\circ}\sim 3^{\circ}$), and the reflected beam carries information

about the crystal surface is presented on a fluorescent screen^[29]. The RHEED pattern allow for the analysis of the surface reconstruction, the crystal structure of the film or the surface roughness of the film. The change in diffraction intensity can be used to analyze the film surface roughness and thus monitor the film growth rate.

The electron beam, generated by an electron gun, passes through a small aperture, and got focused on a fluorescence screen. The beam is deflected by deflection coils 1 and 2 to irradiate the sample surface with a defined glancing angle θ_g (the complementary angle of the incidence angle). The θ_g should be as small as $1^\circ\sim 3^\circ$. Since the θ_g is very small, the focused area on the sample surface is 1–3mm long along the direction of the beam^[29]. The RHEED pattern observed on the fluorescence screen which is placed inside the viewport vacuum chamber, are normally recorded by a CCD camera from the outside.

In general, Ewald construction theory is widely used for an intuitive understanding of the diffraction phenomena.

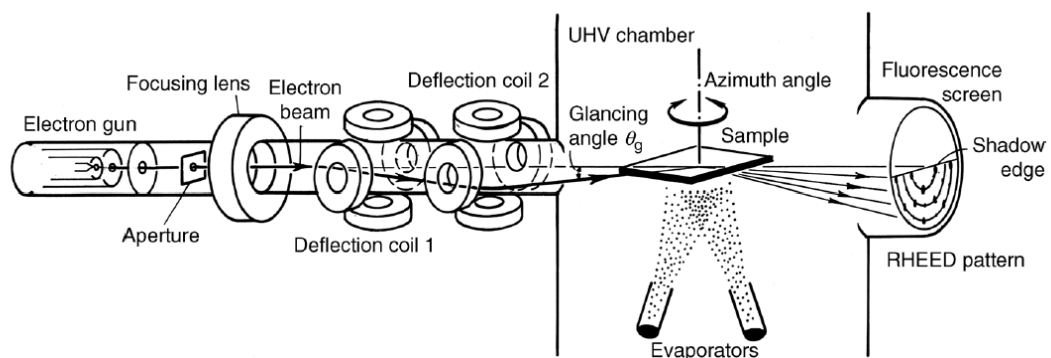


Figure 9: Schematic diagram of RHEED apparatus. Adapted from literature^[30].

We have \mathbf{k}_0 as the wave vector of the incident electron beam. By restricting the

theory in elastic scattering region, we have diffracted waves \mathbf{k}_1 and \mathbf{k}_2 with sample magnitude of wave vector \mathbf{k}_0 . When these vectors are drawn from the same start point as \mathbf{k}_0 , their end points are on a sphere with the radius $|\mathbf{k}_0|$. This is one Ewald sphere^[30].

When the sample which is assumed to be atoms arranged equidistantly on a line along the incident beam, the 2D Fourier transform of this atom row is a series of equidistant planes (reciprocal lattice planes) perpendicular to the atom row on the sample. The crossing point of the Ewald sphere and the reciprocal lattice planes should be series of circles. Concentric circles can be seen on the fluorescence screen (though only half of the circles above the shadow edge can be seen). The rings are called Laue zone L. The circles are slightly distorted near the shadow edge because of the refraction effect of the electron beam^[31].

Next, let us take a 2D square lattice crystal as an example. The reciprocal rods are arranged in square equidistantly and stand perpendicularly to the sample surface. The intersections should be points, as seen on the screen.

The spatial resolution in RHEED structure analysis, which is usually 0.01–0.001nm in shifts of atom positions, is determined by the coherence length of electron beam used. For usual thermal-emission electron beams generated from a heated tungsten filament in RHEED at 10 keV acceleration voltage, the longitudinal coherence length and the transverse coherence length are 100-200nm and 30-80 nm, which are 5-10 times larger than a typical LEED system. This means RHEED scans a larger area than LEED and has higher resolution for the determination of atom positions^[31].

Moreover, by knowing the distance L between the screen and the sample, and the RHEED streak distance d , the lattice constant a along the direction of the beam is $a = \frac{L \times \lambda}{d}$, with λ being the wavelength of the electron^[30]. If the acceleration voltage of electrons is the same, the distance between the sample and the phosphor screen and the angle of grazing incidence are constant, then the distance

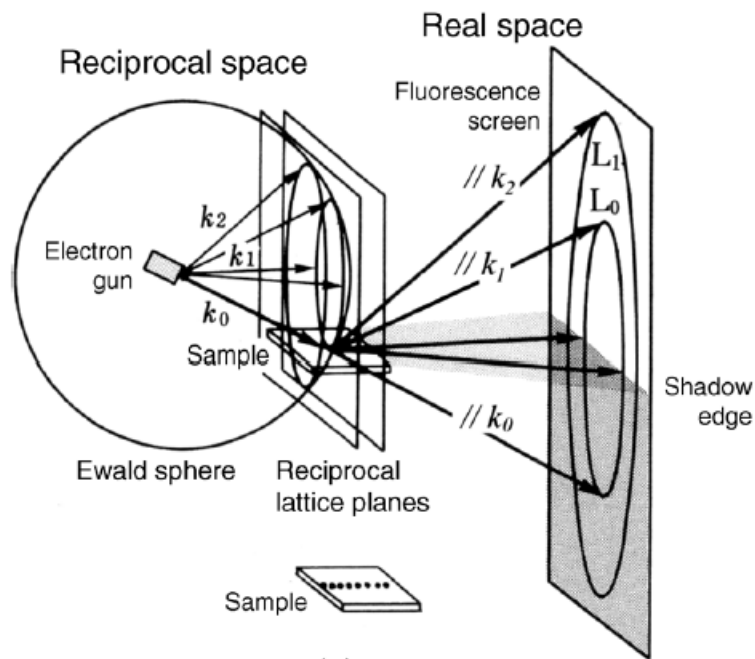


Figure 10: Real space and reciprocal space of RHEED. Adapted from literature^[30].

between the stripes of RHEED and the lattice constant are inversely proportional to each other, and the change in the width of the stripes can be calculated. It is quite accurate to calculate the lattice constant using this method, and the error is generally less than 0.1%^[30].

2.2.2 X-ray photoelectron spectroscopy

X-ray photoelectron spectroscopy is a technique for analyzing the chemical properties

of a material's surface. XPS measures the elemental composition, empirical formulae, elemental chemical states and electronic states of a material. The XPS spectrum is obtained by exciting a solid surface with a beam of X-rays and simultaneously measuring the kinetic energy of electrons emitted within 1-10 nm of the surface of the material for analysis. The photoelectron spectrum records the electrons with kinetic energy above a certain level. The peaks appearing in the photoelectron spectrum are the emission of electrons of a certain characteristic energy from an atom. The energy and intensity of the photoelectron spectral peaks can be used for qualitative and quantitative analysis of surface composition^[32].

In XPS, the sample is irradiated with X-rays and the kinetic energy of the emitted electrons is analyzed. The emitted photoelectron is the result of complete transfer of the X-ray energy to a core level electron.

$$h\nu = BE + KE + \Phi_{\text{spec}} \cdot \quad (17)$$

$h\nu$ is the X-ray energy. BE and KE mean the binding energy and kinetic energy of the electron. Φ_{spec} is the spectrometer work function.

By knowing the X-ray energy(1486.61 eV for Al anode), work function(4.5eV) and scanning the kinetic energy value of the sample, one can easily get the Kinetic energy spectra of the film. Due to the uniqueness of the characteristic energy values of the photoelectron and Auger lines of the elements, comparison with the binding energy of the XPS standard spectroscopy database can help identify the presence of a specific element.

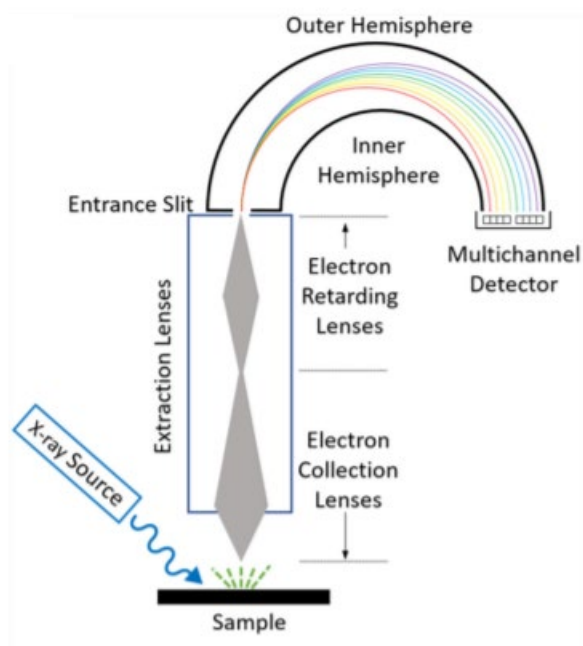


Figure 11: Schematic diagrams show the major components of an XPS instrument. Adapted from literature^[32].

The peak position of the kinetic energy spectra plays an important role in the identification of the element. After excluding the possible heating effect which may be induced by the charging effect on the surface, one can easily identify the element, the chemical valency of the element by analyzing the possible chemical shift and the composition of the sample by calculating the square ratio of specific peaks.

2.2.3 Quartz crystal microbalance

QCM measures the mass per unit area by calculating the change in frequency of a quartz crystal resonator^[33]. It is frequently used in vacuum deposition processes for monitoring the rate of deposition in thin film deposition systems.

The basic principle of quartz crystal microbalance is the piezoelectric effect of quartz crystal: each lattice inside the quartz crystal is in the shape of a hexagon

when it is not affected by external force, if mechanical pressure is applied on both sides of the wafer, it will cause the charge center of the lattice to shift and polarize. Then an electric field will be generated in the corresponding direction of the wafer. Conversely, if an electric field is added to the two electrodes of the quartz crystal, the wafer will be mechanically deformed. This physical phenomenon is called the piezoelectric effect. If an alternating voltage is applied to the two electrodes of the wafer, the wafer will produce mechanical vibration, and at the same time, the mechanical vibration of the wafer will produce an alternating electric field. In general, the amplitude of the mechanical vibration of the wafer and the amplitude of the alternating electric field are minimal. Still, when the frequency of the applied alternating voltage is set to be a specific value, the amplitude increases significantly, and this phenomenon is called piezoelectric resonance. It is actually very similar to the resonance phenomenon of a resonant circuit: when the crystal does not vibrate, it can be regarded as a flat capacitor called electrostatic capacitance C , generally about several pF to several dozens of pF; when the crystal oscillates, the inertia of mechanical vibration can be equated with inductance L . Generally the value of L is several tens of mH to several hundreds of mH. Thus, the oscillation frequency of the circuit is equal to the resonant frequency of the crystal oscillator. Then, the measured resonant frequency is converted into an electrical signal by the controller. Since the resonant frequency of the wafer itself is basically only related to the cutting method, geometry, and size of the wafer, a quartz resonator made by an oscillation circuit can achieve high frequency stability.

For rigid deposits, the crystal oscillation frequency change ΔF is proportional to the change in mass of the deposited film on the working electrode Δm . The change

in mass of the QCM electrode surface can be obtained from this relation. By knowing the mass of the deposited film and size of the QCM, along with the test time and film density and z factor of the film, one can easily calculate the growth rate of the material. The QCM controller can automatically show the growth rate of the film with known Z factor and density of the material.

2.2.4 X-ray diffraction

XRD is a research tool that obtains information on the composition of a material, the structure of atoms or molecules inside the material by emitting X-ray on the material and analyzing its diffraction pattern.

X-rays are generated by an accelerated electron beam of 30-60 kV in an X-ray tube (vacuum 10^{-4} Pa), which impinges on a metal (e.g., pure Cu or Mo) target surface. The commonly used rays are Mo $K\alpha$ rays, including both $K\alpha_1$ and $K\alpha_2$ rays (intensity 2:1), with a wavelength of 71 pm and 63 pm. In our case, a Cu target was used and it can generate x-ray photons from 8 to 9 keV, with a wavelength of 1.546\AA ^[34].

By using the commercial Bruker D8 Discover system in the institute, we can easily obtain the 2θ - ω scan of the sample after carefully calibrating the related system parameters. By comparing the diffraction peaks with the standard PDF database, it is easy to understand the crystallinity of the film along the z axis of the sample. By combining XRD with *in-situ* RHEED, it is definitive to understand the crystallinity of the sample.

2.2.5 Rutherford backscattering spectrometry

RBS is an ion scattering technique for compositional thin film analysis^[35]. RBS is unique that it allows quantification without the use of a reference standard. During RBS analysis, high-energy (MeV) He^{2+} ions (i.e., alpha particles) are guided onto the sample, and the energy distribution of the backscattered He is measured for ions at a given angle. Since the backscattering cross-section is well-defined for each element, quantitative compositional depth distributions can be obtained from the RBS spectra.

An RBS instrument generally includes three basic components. First of all, an ion source for alpha particles (He^{2+} ions) or protons. Secondly, a particle accelerator capable of accelerating incident ions to high energies in the range of 1-3 MeV. Thirdly, a detector capable of measuring the energies of backscattered ions over some range of angles^[36].

We use RBS here to analyze the sample composition of each layer of the film, cross-checked with the *in-situ* XPS data.

2.2.6 Atomic force microscope

AFM is an analytical technique that can be used to study the surface structure of solid materials, including insulators^[37]. It holds a micro-cantilever, which is extremely sensitive to weak forces, at one end and a tiny needle tip at the other end, so that it is in gentle contact with the surface of the sample. Due to the very weak repulsive forces between the atoms at the tip of the needle and the atoms on the sample surface, a small deflection of the cantilever occurs. By detecting the amount of deflection and controlling the constant repulsive force with the feedback loop,

the position change of the micro-cantilever corresponding to each point can be obtained, and thus an image of the sample surface topography can be achieved. We use the commercial Bruker AFM to measure the topography of the substrate and samples.

2.2.7 Scanning tunneling microscope

Scanning tunneling microscopy is a non-optical microscope that uses the quantum tunneling effect^[38]. A very sharp probe with atomic resolution is used to scan the sample surface. When the distance between the tip and the sample surface is close enough, electrons can pass through the gap between the probe and the sample through quantum tunneling to form a tunneling current. The closer the distance, the higher the current. During the scanning process, the probe is moved up and down to keep the current constant, and the surface condition of the sample can be known by recording the up-and-down movement of the probe. Because of the limitations of the operating principle, the microscope can only measure the surface of conductive samples^[39]. However, for Mn₃Ge film, I only use insulating substrate YSZ. To ensure the good surface conductance of the sample, I first deposit an Au stripe on the edge of the substrate (thickness depends on the Mn₃Ge layer thickness), when fixing it on the sample holder for deposition, press the Mo clamp on the stripe to make sure the good contact between the stripe and the ground. After the deposition of Mn₃Ge, the stripe can ensure the good conduction of the film surface. With the help of the Papaya STM research group in the institute, we measure the STM of the Mn₃Ge film without breaking the vacuum to have a better understanding of the surface of the film.

2.3 Electrical and magnetic measurement methods

2.3.1 Physical property measurement system

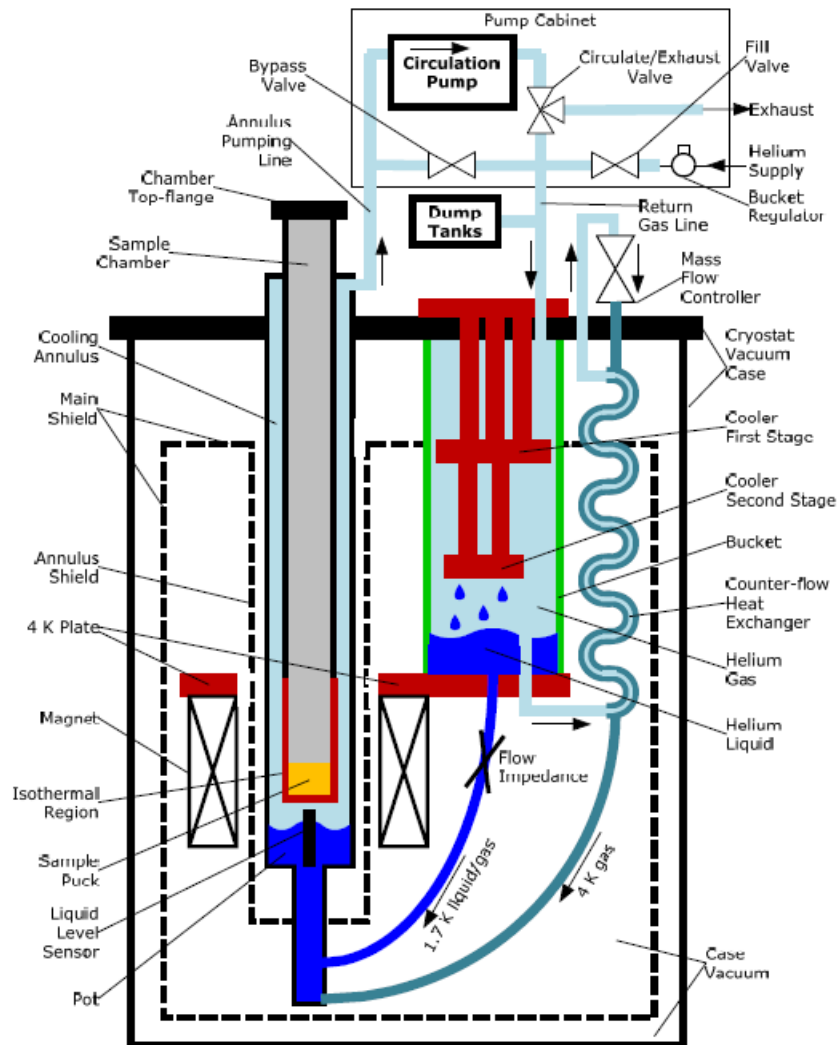


Figure 12: Illustration of the cryostat control system of the PPMS. Adapted from the literature^[40].

The PPMS was introduced by Quantum Design in the middle 1990s after the successful introduction of the MPMS1. A complete PPMS consists of a base system and various options. Depending on the size of the superconducting magnets integrated inside the base system is divided into 7 Tesla, 9 Tesla, 14 Tesla and 16

Tesla systems. However, unlike the MPMS, which focuses exclusively on magnetic measurements, the PPMS performs magnetic measurements, electrical transport measurements, thermal parameter measurements, and thermoelectric transport measurements using various options on the temperature and magnetic field platform built by the base system. The base system mainly consists of a software operating system, a cryostat control system, a magnetic field control system, a sample operating system, and a gas control system.

In this thesis, we use the 9T Dynacool PPMS investigate the transport property of the Mn_3Ge film. First, we need to fabricate Hall bar pattern on the substrate for better variable control. Then we need to glue the sample on the PPMS puck(standard puck, IP rotation puck and OP rotation puck) with Varnish glue which has a good thermal conductivity from room temperature to 2K. After the glue is firm, we need to bond the pad of the hall bar pattern to the contact pad of the puck. Then we can load the sample into the chamber. In electrical switching measurement, we use Keithley 2635B multimeter to inject an electric pulse and reach the transverse voltage. In AHE measurement, I use Keithley 6221 meter as the DC current source and 2182 nano voltage meter to read the voltage signal of the pattern. In switching experiment, I use Keithley 2635B as DC voltage input source and read-out meter. The LabView program I use for the PPMS measurement was created by other colleagues.

2.3.2 Magnetic property measurement system

MPMS is the magnetic property measurement system introduced by Quantum Design Company. It is a very sensitive magnetometer due to the utilization of a SQUID (superconducting quantum interference device) to measure the change of the magnetic

flux, which is converted to or measured as current, as the sample moves through the superconducting detection coil. 7T MPMS allows to measure the magnetic moment and the AC susceptibility with magnetic fields between +7 and -7 T and temperatures between 1.9 K and 400 K.

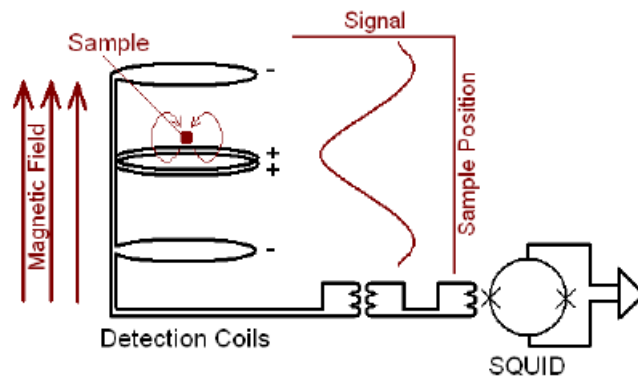


Figure 13: SQUID signal detection schematic. Adapted from the literature^[41].

To use the MPMS to measure the AFM Mn_3Ge film, first we need to prepare the sample in the size of $5mm \times 3mm$, then measure the OP magnetic moment by inserting the sample into a plastic straw. For measuring the IP component, we need to glue the sample on a quartz rod by Varnish glue. Then we can load the sample into the chamber. After calibrating the sample position inside the chamber (around 66 mm), the sample is ready for further measurement.

MPMS is convenient for magnetic property measurement, however we still need to pay attention to the following cautions. First, make sure do not introduce any dirty signal in the chamber as it may cover the actual signal of the sample, what we need to do is to keep the sample clean and use the clean glue. Secondly, we need to subtract the magnetic signal of the substrate (usually it is weak diamagnetic signal for oxide substrates) and buffer layers from the whole stack sample data. To do this, first we need

to measure the substrate signal, then deposit the full stack except the target layer, measure again then we can get the contribution of the buffer and capping layers. Next, measure the data of the newly deposited whole stack sample. By considering the size of the sample, we can carefully get the pure target layer magnetic measurement data. Sometimes, the substrates we cut are in an irregular shape. To determine the volume of the substrate, we need to weigh the substrate and divide the mass by the density of the substrate, thus the answer is the volume of the substrate. For Mn_3Ge sample, as the film has very weak net magnetization, it is essential to use a thick Mn_3Ge sample for magnetic moment measurement.

2.3.3 Spin torque ferromagnetic resonance

ST-FMR is used as a powerful technique for investigating the properties of magnetic materials, such as resonance frequency and field, magnetic anisotropy and Gilbert damping constant α , spin hall angle θ_{sh} and spin mix conductance for evaluating the SOT efficiency, interface transparency of the sample. To use the ST-FMR, usually the sample needs to hold a bilayer structure with one layer of ferromagnetic film on another layer of film with the spin hall effect^[42].

SOT has been employed for exciting magnetization oscillations in the ST-FMR measurement, where the radio frequency current I_{rf} is applied in the film plane, and R_{rf} usually originates from anisotropic magnetoresistance (AMR) or spin Hall magnetoresistance (SMR). AMR usually decreases as the thickness of the film decreases. The intensity of the SMR signal depends on the angle between the magnetization M and the direction of the spin-polarized electrons induced by the spin Hall effect. For heavy metal /ferromagnetic metal structure, the signal relies

more on the interface rather than the thickness of the film which makes it ideal for thin film-based experiment.

Under macrospin approximation, the time domain dynamics of the magnetization vector \mathbf{m} of a ferromagnet in the presence of an effective magnetic field \mathbf{H}_{eff} can be described by the Landau–Lifshitz–Gilbert (LLG) equation, as follows^[43]:

$$\frac{d\mathbf{m}}{dt} = (-\gamma\mu_0\mathbf{m} \times \mathbf{H}_{\text{eff}}) + \left(\alpha\mathbf{m} \times \frac{d\mathbf{m}}{dt}\right) \quad (18)$$

With γ being the gyromagnetic ratio, μ_0 vacuum permeability and α Gilbert damping coefficient. The first term on the right side of equation (18) is a precession term that rotates \mathbf{m} around \mathbf{H}_{eff} , while the second term (damping term) aligns \mathbf{m} along \mathbf{H}_{eff} .

When a spin-polarized current (polarized along $\hat{\sigma}$) interact with the magnetization vector, the equation (18) can be modified as^[42]:

$$\frac{d\mathbf{m}}{dt} = -\gamma\mu_0\mathbf{m} \times \mathbf{H}_{\text{eff}} + \alpha\mathbf{m} \times \frac{d\mathbf{m}}{dt} + \boldsymbol{\tau}_{\text{DL}} + \boldsymbol{\tau}_{\text{FL}}. \quad (19)$$

The damping torque $\boldsymbol{\tau}_{\text{DL}}$ is of the $\mathbf{m} \times (\hat{\sigma} \times \mathbf{m})$ symmetry, The field like torque $\boldsymbol{\tau}_{\text{FL}}$ is of the $\hat{\sigma} \times \mathbf{m}$ symmetry.

By introducing the alternating magnetic field \mathbf{H} , if the frequency of \mathbf{H} is tuned to the natural precession frequency of \mathbf{m} , the amplitude of the forced precession will be maximum due to the FMR resonance. The resonance frequency f ($f = \omega_{\text{res}}/2\pi$) and the resonance field H_0 are related by the Kittel's relation^[43],

$$f = \left(\frac{\gamma}{2\pi}\right) [H_0(H_0 + 4\pi M_{\text{eff}})]^{\frac{1}{2}}. \quad (20)$$

The $4\pi M_{\text{eff}}$ term is the effective demagnetization field of the ferromagnet.

Next, let's take Pt/Py bilayer as an example. when an IP radio frequency charge current I_{rf} is injected into the Pt/Py bilayer, non-equilibrium spins are generated at the Pt/Py interface due to SOC in the Pt layer, the equation (19) can be modified as follows^[43]

$$\frac{d\mathbf{m}}{dt} = -\gamma\mu_0\mathbf{m} \times \mathbf{H}_{\text{eff}} + \alpha\mathbf{m} \times \frac{d\mathbf{m}}{dt} + \gamma \frac{\hbar}{2e\mu_0 M_S t} \times J_{S,\text{rf}} (\mathbf{m} \times \hat{\sigma} \times \mathbf{m}) - \gamma\mathbf{m} \times \mathbf{H}_{\text{rf}}. \quad (21)$$

M_S is the saturation magnetization of Py, t is the thickness of the Py layer, $J_{S,\text{rf}}\hbar/2e$ is the oscillating spin current density injected into Py, \mathbf{H}_{rf} is the Oersted field generated by the rf current. \mathbf{H}_{eff} here is the sum of the external magnetic field \mathbf{H}_{ext} and the demagnetization field $4\pi M_{\text{eff}}$. The third and fourth terms on the right side

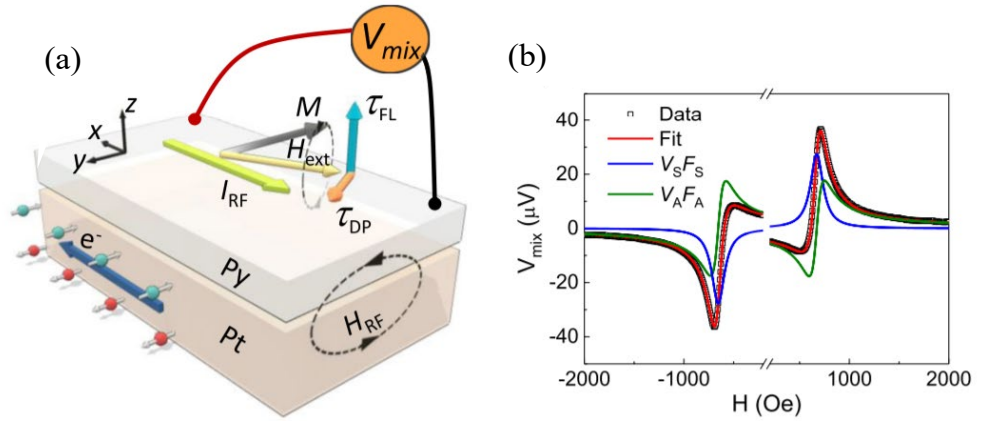


Figure 14: (a) Illustration of spin current generation in Pt/Py system in ST-FMR measurements. Blue arrow denotes the electron flow direction (opposite to the I_{rf} direction). The arrows with green and red balls denote the generated spin polarizations in the Pt layer. (b) A typical ST-FMR signal from a Pt (6 nm)/Py (4nm) device at 6 GHz. The blue and green curves represent the symmetric Lorentzian ($V_S F_S$) and antisymmetric Lorentzian ($V_A F_A$) components. Adapted from literature^[42].

of equation (21) are the result of in-plane spin torque and the out-of-plane Oersted

field induced torque. The mixing voltage signal measured from the sample is the combination of in-plane and out-of-plane torques, which can be written as^[42]

$$V_{\text{mix}} = V_S + V_A = -\frac{1}{4} \frac{dR}{d\theta} \frac{\gamma I_{\text{rf}} \cos \theta}{\Delta 2\pi \left(\frac{df}{dH} \right) \Big|_{H_{\text{ex}} = H_0}} [S F_S(H_{\text{ext}}) + A F_A(H_{\text{ext}})], \quad (22)$$

$$F_S(H_{\text{ext}}) = \frac{\Delta^2}{[\Delta^2 + (H_{\text{ext}} - H_0)^2]}, F_A(H_{\text{ext}}) = \frac{F_S(H_{\text{ext}})(H_{\text{ext}} - H_0)}{\Delta}, \quad (23)$$

$$S = \frac{\hbar J_{S,\text{rf}}}{(2e\mu_0 M_s t)}, A = H_{\text{rf}} \left[1 + \left(\frac{4\pi M_{\text{eff}}}{H_{\text{ext}}} \right) \right]^{\frac{1}{2}}. \quad (24)$$

V_S and V_A are the symmetric and antisymmetric components of the ST-FMR signal V_{mix} . $F_S(H_{\text{ext}})$ is the symmetric Lorentzian function centered at the resonant field H_0 with linewidth Δ , correspond to the in plain spin torque. $F_A(H_{\text{ext}})$ is the antisymmetric Lorentzian function induced by the out of plain Oersted field generated torque. R is the resistance of the pattern.

The Oersted field H_{rf} can be calculated from the geometry of the sample. Since the microwave skin depth is much greater than the Py thickness, the current density in Py should be spatially uniform, thus the Oersted field from the charge current in the Py should produce no net torque on itself. The charge current density in Pt layer $J_{c,\text{rf}}$ should be responsible for the Oersted field induce torque, so $H_{\text{rf}} = J_{c,\text{rf}}d/2$. Then, it is obvious that to calculate the ratio of the spin current density injected into the Py layer to the charge current density in Pt layer, one can simply use the ratio of the symmetric and antisymmetric components of the resonance curve, this ration is the spin hall angle θ_{SH} ^[43].

$$\theta_{SH} = \frac{J_{S,rf}}{J_{C,rf}} = \frac{S e \mu_0 M_s t d}{A \hbar} \left[1 + \left(\frac{4\pi M_{\text{eff}}}{H_{\text{ext}}} \right)^2 \right]^{\frac{1}{2}}. \quad (25)$$

This way of calculating the θ_{SH} , also called the line shape method, may give rise to a wrong estimation in the case of a non-negligible field-like torque $\boldsymbol{\tau}_{FL}$, which might be induced by the interfacial effects, such as the Rashba effect and it can produce an antisymmetric Lorentzian line shape signal similar to H_{rf} , the value of θ_{SH} might be underestimated from the method of V_S/V_A . $\boldsymbol{\tau}_{FL}$ can be evaluated by the equation $\boldsymbol{\tau}_{DL} = \theta_{sh} J_C \hbar / (2eM_s t)$.

An additional possible contribution V_{SP} to the measured mix voltage signal is the spin pumping due to the inverse SHE by $J_{C,rf} = \theta_{sh} (J_{S,rf} \times \hat{\sigma})$.

$$V_{SP} = \theta_{sh} \frac{eW\lambda_S R}{2\pi} \tanh\left(\frac{d}{2\lambda_S}\right) \times \text{Re}(g_{\uparrow\downarrow}^{\text{eff}}) \omega(\theta_c)^2 \sin(\theta_H) \sqrt{\frac{H_0}{(H_0 + 4\pi M_{\text{eff}})}}, \quad (26)$$

$$\theta_c = \frac{1}{\frac{dR}{d\theta_H}} \frac{2}{I_{\text{RF}}} \sqrt{(V_S)^2 + (V_A)^2}, \quad (27)$$

where W is the pattern width, R is the device resistance, d is the Pt thickness, $\text{Re}(g_{\uparrow\downarrow}^{\text{eff}})$ is the real part of the effective spin mixing conductance ($\approx 2 \times 10^{19} \text{ m}^{-2}$ for Pt/Py), θ_c is the maximum precession cone angle in the device plane. Noted that V_{SP} is proportional to the device resistance^[42].

From the Pt/Py layer ST-FMR measurement, we can clearly see that the Symmetric peak changes sign as we use the reversed the magnetic field, this is coincided with the equation (21). However, suppose there are large perpendicular Oersted field torque,

which won't change sign with the sweeping field and yield a symmetric peak compatible with the spin torque. In that case, you will see the noticeable symmetric peak difference in magnitude from the positive and negative sweep field measurements.

As mentioned before interface effect, like Rashba effect, interface defect (rough surface or oxidation problem) may give rise to the asymmetric voltage signal. So, to avoid this situation, we can use the symmetric part signal only to calculate the sin hall angle.^[43]

$$V_S = -\frac{I_{RF}\gamma \cos \theta_H}{4} \frac{dR}{d\theta_H} \tau_{DL} \frac{1}{\Delta} F_S(H_{ext}), \sigma_S = \frac{J_S}{E} = \frac{\tau_{DL} M_S t}{E}, \theta_{sh} = \frac{\sigma_S}{\sigma}. \quad (28)$$

$dR/d\theta_H$ is the angular dependent magnetoresistance at θ_H , θ_H is the constant angle between H_{ext} and I_{rf} . Δ is the linewidth of the ST-FMR signal in the frequency domain, E is the microwave electric field across the ST-FMR device, and σ_S and σ are the spin Hall and longitudinal charge conductivities of the spin current generation layer. τ_{DL} can be derived from

$$V_A = -\frac{I_{RF}\gamma \cos \theta_H}{4} \frac{dR}{d\theta_H} (\tau_{FL} + \tau_{Oe}) \frac{\left[1 + \left(\frac{\mu_0 M_{eff}}{H_{ex}}\right)^2\right]^{\frac{1}{2}}}{\Delta} F_{asym}(H_{ext}). \quad (29)$$

The resistance of the HM/FM pattern can be written as $R = R_0 + \Delta R \cos^2(\theta_H)$ due to the AMR effect. We obtain $\frac{dR}{d\theta_H} = -2\Delta R \sin(\theta_H) \cos(\theta_H) \propto \sin(\theta_H) \cos(\theta_H)$, thus $V_{mix} \propto \cos^2(\theta_H) \sin(\theta_H)$ and $V_{mix} \propto \frac{dR}{d\theta_H} \cos(\theta_H)$. Thus, it is observed that even though the best angle for maximum AMR is at 45° the largest ST-FMR signals are achieved at $\theta_H \sim 35^\circ$.

V_S -only technique requires additional measurements to determine the $dR/d\theta_H$ and

σ , and requires quantitative determination of I_{rf} through the whole device by considering the device resistance and RF power losses using the microwave network analysis measurement. On the other hand, a Cu with negligible SOC or other insertion layers can be inserted between the HM and FM layer to eliminate or modify the interface SOT effect.

Another method, named the modulation of damping method (sometimes referred as linewidth method), was used for HM/FM bilayer systems in the spin Hall scheme and the magnetization can be tuned by applying a DC current in the HM layer. From the STT theory, the damping α and the linewidth Δ will increase or decrease depending on the relative direction of spin polarizations with respect to the magnetization direction^[42].

$$\Delta = \Delta_0 + \Delta_{sh} = \frac{2\pi f}{\gamma} \alpha + \frac{2\pi f}{\gamma} \frac{\sin \theta_H}{(H_{ext} + 2\pi M_{eff})\mu_0 M_s t} \frac{\hbar}{2e} J_C \theta_{sh}. \quad (30)$$

Δ_0 is the non-biased linewidth, Δ_{sh} is the modulated linewidth due to the DC bias induced spin currents, f the RF power supply frequency. By fitting the data of linewidth dependence of DC current or damping coefficient dependence of DC current, the SOT efficiency θ_{SH} is obtained accordingly.

Recently, the linewidth method has been utilized for the SOT efficiency evaluation of metallic antiferromagnetic materials^[44], however, due to the weaker ST-FMR signals, it is difficult to evaluate the SOT efficiency θ_{SH} .

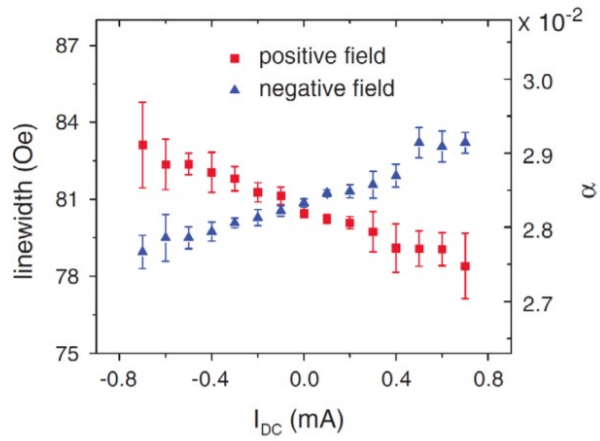


Figure 15: The FMR linewidth and Gilbert damping coefficient α as a function of the DC current, I_{dc} , in the Pt (6nm)/Py (4nm) bilayer device at $f = 8$ GHz. Adapted from literature^[43].

To use the homemade ST-FMR in the institute, we first need to fabricate the ST-FMR pattern, align the pattern stripe in the ST-FMR with the angle of field to reach the maximum signal. Then we can choose the stripe to carry out the line shape and line width measurement.



3 Sample preparation

3.1 Substrate and buffer layers

3.1.1 Substrate preparation

To prepare the hexagonal $\text{Mn}_3\text{Ge}(0001)$ film for magnetic and transport measurement, we investigate the widely used substrates and try to find the best candidate for the deposition of the Mn_3Ge and possible buffer layers by calculating the lattice mismatch between different substrates and Mn_3Ge .

Material	Structure	Constant a	Constant c	substrate orientation	Atom distance a'
Mn_3Ge	Kagome hexagonal	5.28	4.22	(0001)	2.64
Graphene	hexagonal	2.46	3.35	(0001)	2.46
BN	hexagonal	2.5	6.66	(0001)	2.5
MgO	cubic	4.212		(111)	2.98
SiC	hexagonal	3.0730	10.053	(0001)	3.0730
ZnO	hexagonal	3.25	3.13	(0001)	3.25
YSZ	cubic	5.12		(111)	3.62
Si	cubic	5.431		(111)	3.83
BaF_2	cubic	6.196		(111)	4.38
Al_2O_3	hexagonal	4.763	13.003	(0001)	4.763
STO	perovskite	3.905		(111)	5.50
LAO	Perovskite	3.821		(111)	5.402

Table 1: commonly used substrate data.

From the above table, we can find out that the Graphene and BN substrates might be

possible for bare Mn₃Ge film deposition as the lattice mismatch is lower than 3%.

MgO, SiC, ZnO, and YSZ need an additional buffer layer as the large lattice mismatch. STO and LAO are also possible as the IP atom distance a' of Mn₃Ge(0001) film times 2 is quite close to the a' of STO and LAO substrate, by adding favorable inserting layers between these substrates and Mn₃Ge film, it is possible to make up for the large lattice mismatch.

Large-scale BN substrate can not be produced by standard crystal growth method and the commonly used way to have BN substrate is to transfer small-scale BN flake on Si substrate. The scale of BN flake will be too small for MBE deposition.

The MgO(111) substrate from the supplier is way too rough for MBE thin film deposition. Due to the nature of the oxide cubic substrate (111) surface, most of the suppliers only use physical polish as final treatment which will lead to deep scratches on the substrate surface. Some suppliers use chemical etching treatment, which will create deep holes on the surface of the substrate.

In figure (16), one can check the AFM picture of MgO(111) substrate right out of the box and after solvent cleaning and annealing test, for physically grounded and chemically etched substrate, respectively. The depth of the scratched line is around 10nm and for the hole about 50nm. After annealing, the substrates show seesaw steps but the defects are still there.

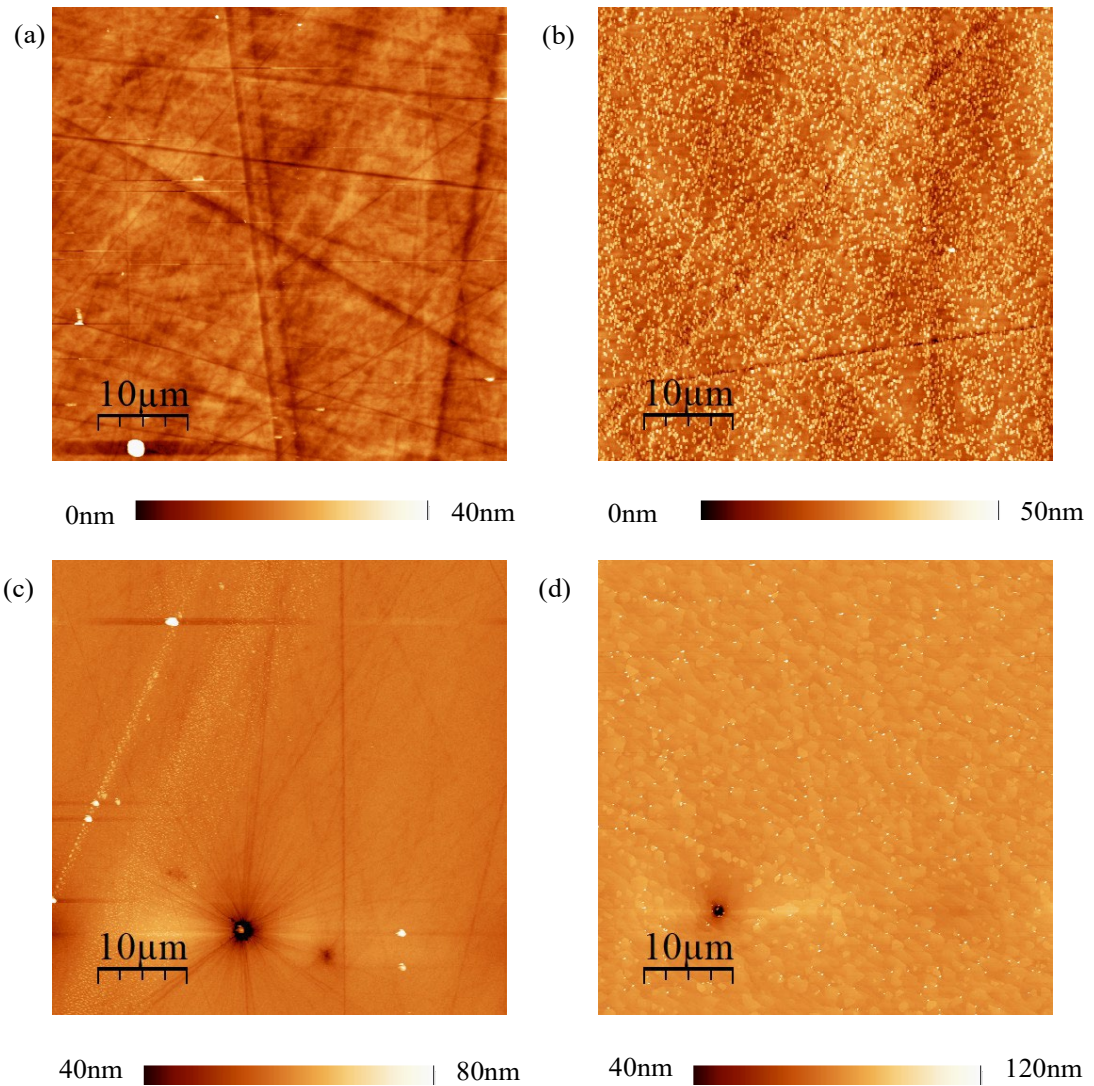


Figure 16: (a) Physical grounded MgO(111) before annealing. (b) physical grounded MgO(111) after cleaning and annealing test. (c) chemical etched MgO(111) substrate before annealing. (d) chemical etched MgO(111) after cleaning and annealing treatment.

After the failure of MgO substrate treatment, the realistic candidates of the substrates are Graphene, SiC, ZnO, YSZ, STO and LAO. However, after couple of test deposition, Mn_3Ge films grown directly on atomically flat Graphene, SiC and ZnO substrates shows island growth behavior when monitoring the films growth by *in-situ* RHEED. Using the buffer layer Ru on graphene will not help with the crystallinity, the sample even shows light polycrystalline rings from RHEED. However, the basic orientation of Mn_3Ge films is still (0001) orientation, as confirmed with the RHEED for Mn_3Ge on YSZ(111).

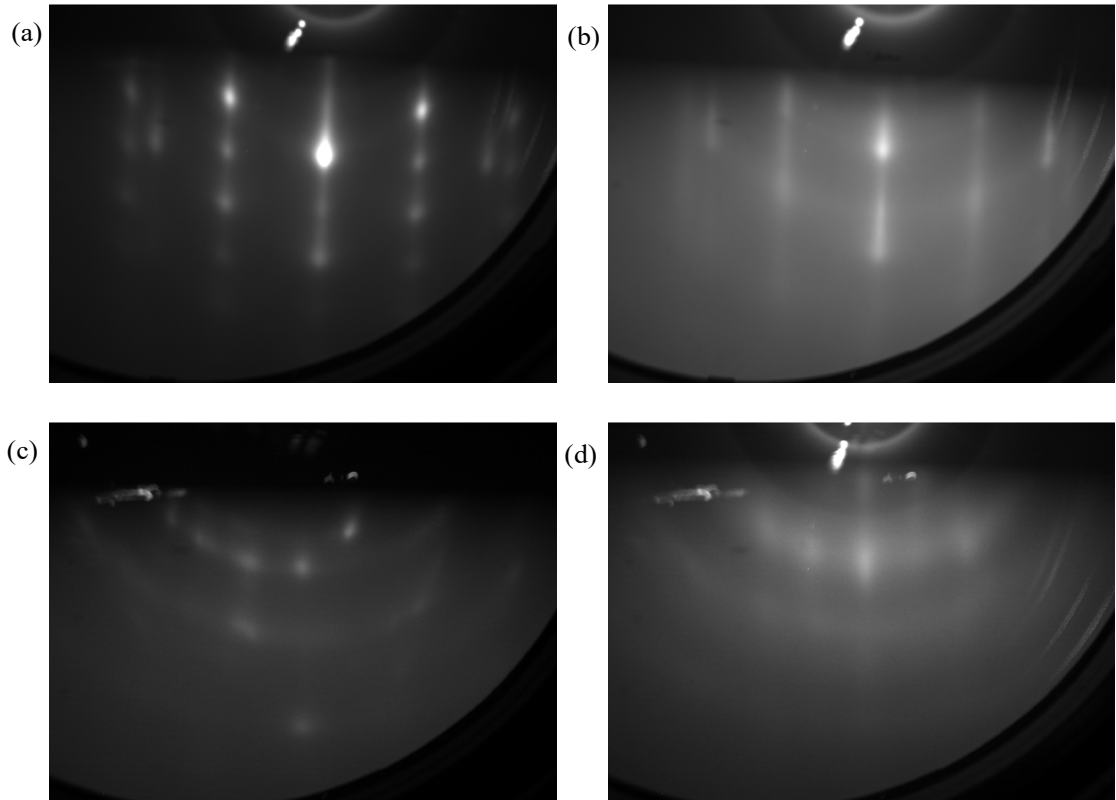


Figure 17: The RHEED picture of Mn_3Ge film directly on (a) graphene and (c) LAO and with a Ru buffer on (b) graphene and (d) LAO.

Mn_3Ge films deposited directly on STO (111) and LAO (111) shows polycrystalline structure with rough surface and island growth behavior, as shown in RHEED picture. By adding a Ru(0001) buffer layer, the situation do not getting any better. Mn_3Ge films directly grown on the YSZ(111) substrate shows similar quality as it on STO(111) and LAO substrate. However, by adding a layer of Ru(0001) film with the thickness between 1.5nm and 5nm, clear $Mn_3Ge(0001)$ RHEED streaks show up and indicate a smooth layer film.

There are 2 kinds of YSZ(111) substrates used in the following experiment. One is perfect YSZ(111) substrate with offcut angle less than 0.1deg, the other one is 3° offcut YSZ(111) substrate with large offcut angle in order to have offcut $Mn_3Ge(0001)$ films so that the IP spin texture of Mn atoms can be tilted with OP

component for transport measurement. Details will be explained in later section.

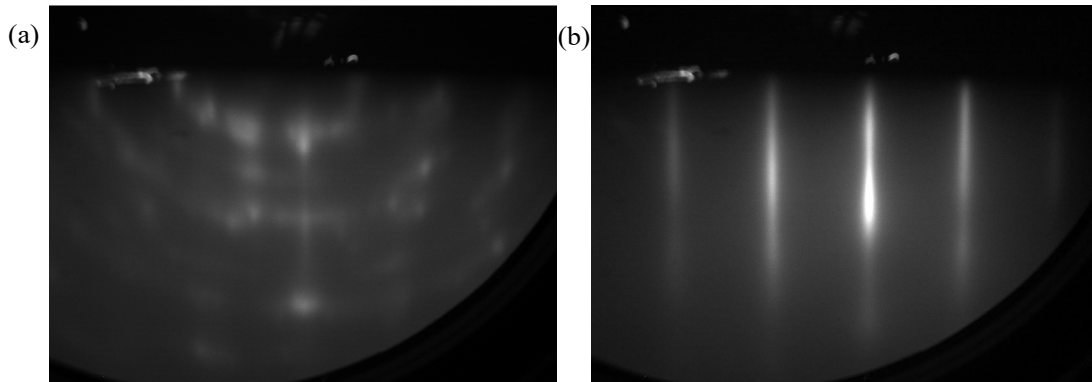


Figure 18: RHEED pattern of $\text{Mn}_3\text{Ge}(0001)$ grown (a) directly on $\text{YSZ}(111)$ substrate and (b) with Ru buffer layer.

Substrate treatment is crucial to have an atomic flat substrate surface. Below is the cleaning method I use for YSZ substrate preparation. Sample cleaning method can also be used for sapphire substrate.

- 1) Soak the substrate in ethanol for 12 hours.
- 2) Clean the substrate in ultrasonic bath of acetone or Isopropanol for 10 min to remove bulky dissolvable contaminants and particulate materials.
- 3) Rinse thoroughly in DI water thoroughly and blow with dry nitrogen gas.
- 4) Heat the substrate in $\text{NH}_4\text{OH}(25\%): \text{H}_2\text{O}_2(30\%): \text{H}_2\text{O}(10\%) = 1: 1: 5$ to about 80°C for 10 min. NH_4^+ ions in the cleaning solution will complex with heavy metal on the substrate surface to form a soluble metal salt which can be removed.
- 5) Rinse thoroughly in DI water thoroughly and dry with pure nitrogen gas.
- 6) Soak the substrate in solution of $\text{HCl}(36\% \text{ hydrochloric acid}): \text{H}_2\text{O}_2(30\%): \text{H}_2\text{O}$

=1: 1: 3 at about 80°C for 10 min. H⁺ ion in the cleaning solution will be replaced with the light metal impurities to form soluble salt and got removed.

- 7) Rinse thoroughly in DI water thoroughly and dry with pure nitrogen gas.
- 8) Clean in H₂SO₄(98% Sulphuric acid): H₃PO₄(Orthophosphoric acid)=1:3 at about 250°C for 10min to move the oxide layer on the substrate.
- 9) Fully rinse with deionized water and dry with a stream of high-speed pure nitrogen.

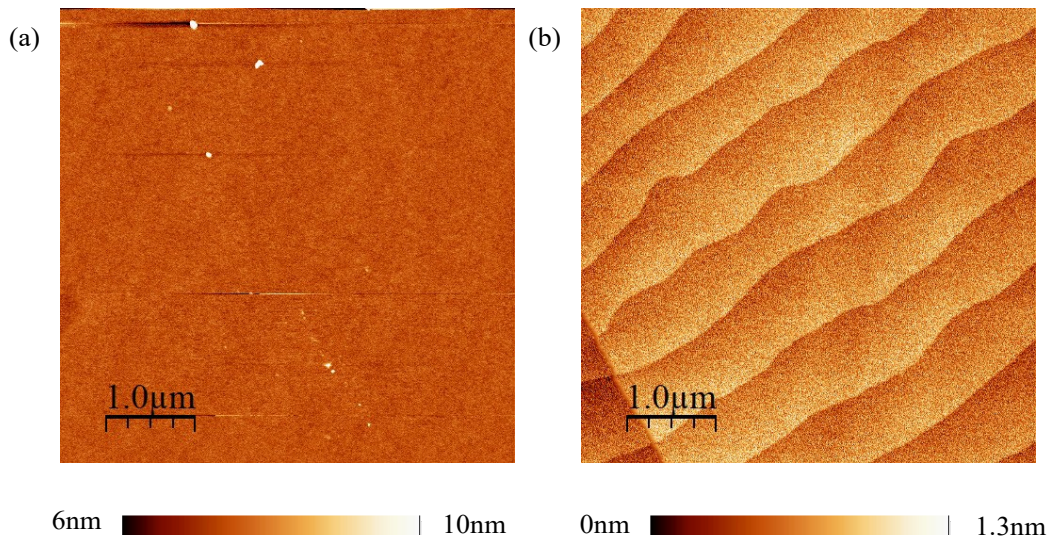


Figure 19: AFM of perfect cut YSZ(111) substrate (a) before annealing and (b) after annealing.

After the cleaning, the substrate needs to be annealed in muffle furnace at 1200°C for 4 hours to achieve the atomic flat surface situation.

In figure (19), the AFM image of the YSZ(111) substrate before annealing is quite smooth with rms of 3.43Å. After sufficient annealing process, the rms of the same substrate reaches 1.85Å, and there are atomic flat steps shown on the surface with step height of 3.41Å. The width of the step is between 700nm to 800nm. The results

mean it is sufficient to anneal the YSZ(111) to have a smooth surface.

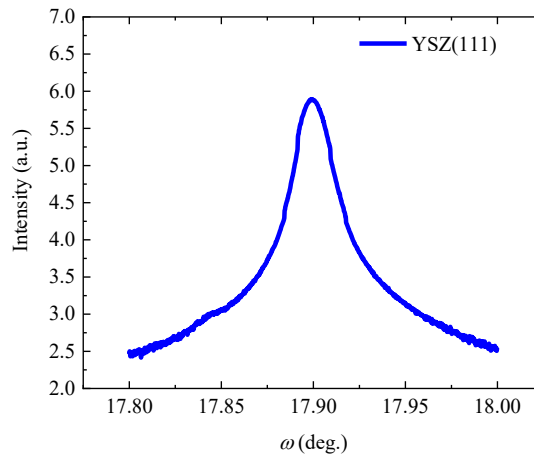


Figure 20: XRD measurement of the rocking curve of perfect cut YSZ(111) peak.

After annealing the substrate, it is better to check the rocking curve of the substrate. Substrates from the suppliers, even from same batch or same sample box, will have different cutting qualities. Some may have split rocking curves indicating there are large miscut of the substrates or the single crystal from which the substrate was cut from, has tiny domains. We can choose the substrates with the best quality for sample deposition and other less perfect substrates for calibration of deposition parameters.

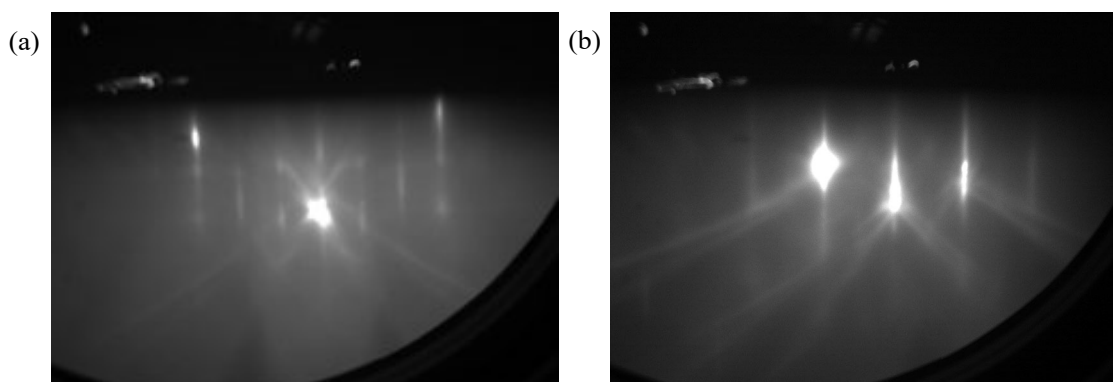


Figure 21: The RHEED pattern of perfect cut YSZ(111) substrate along d (a) YSZ[11-2] and (b) YSZ[10-1] direction.

In figure (21) we can see the typical RHEED pattern of the perfect cut YSZ(111) substrate. Before deposition, it is preferable to measure the XPS to check the surface's chemical cleanness.

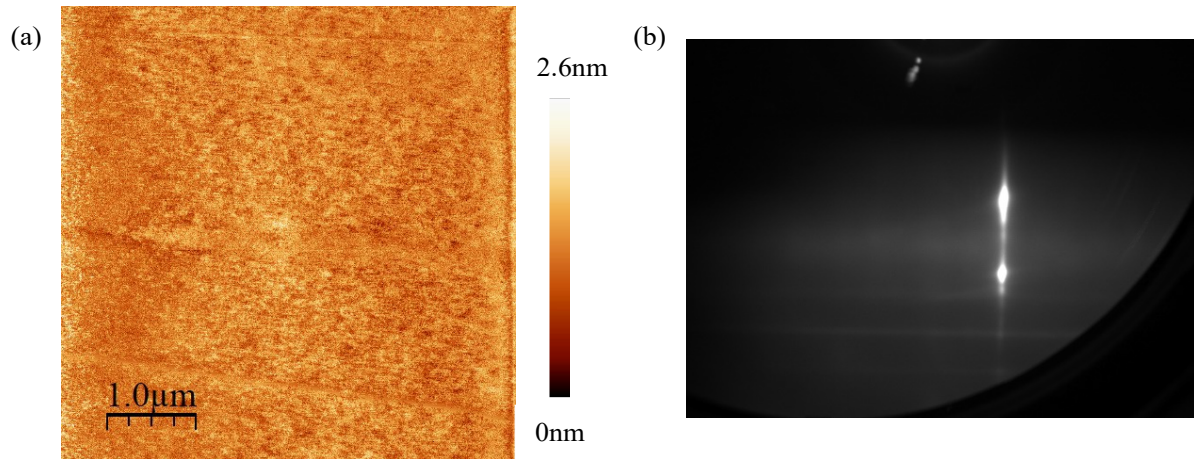


Figure 22: (a) The AFM of annealed 3° offcut YSZ(111) substrate. (b) RHEED pattern of the same piece of substrate.

As for the 3° offcut YSZ(111) substrate, after the sample cleaning and annealing process, it also has a very smooth surface with rms being 1.93 Å, but without atomic flat steps. The RHEED pattern of the offcut substrate has only one visible streak which is different from the perfect RHEED pattern. It is quite acceptable as RHEED is a surface sensitive technology, as the crystal structure changes with 3° offset, the RHEED pattern will change obviously.

3.1.2 Buffer layer determination and calibration

In accordance with the substrate candidates, Ru is chosen as the best candidate as it has a hexagonal crystal structure and the lattice mismatch between Ru(0001) and Mn₃Ge(0001) is less than 0.74%. The lattice constant of Ru are $a=2.70 \text{ \AA}$ and $c=4.28 \text{ \AA}$. To have the best Ru film quality, substrate temperature

dependence of Ru crystal quality measurement has been carried out. From the RHEED pattern, the Ru deposition temperature should be as high as possible in Quince chamber for long-term deposition, so I need to deposit the Ru(0001) film at 600°C, followed by post annealing at 500°C for 30min to make it smoother.

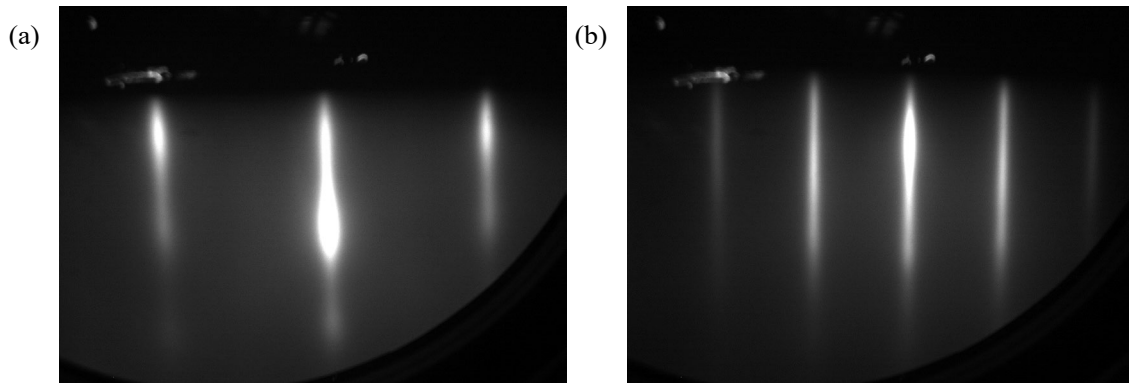


Figure 23: RHEED pattern of 5nm Ru(0001) film deposited at 600° on perfect YSZ(111) substrate, along (a) [10-10] and (b)[11-20] azimuthal direction.

As shown in figure (23) Ru shows good crystal quality and smooth surface according to RHEED data. The epitaxial relationship among them is YSZ(111)[11-2] // Ru(0001)[10-10] and YSZ(111)[10-1]//Ru(0001)[11-20]. By calculating the ratio of the distance between RHEED stripes in two directions to be 1.78 which is close to $\sqrt{3}$, we can confirm it is in hexagonal phase. By analyzing the distance between the strips, we can calculate the in-plane lattice constant to be 2.77Å. The growth rate of Ru layer is usually around 160 s/Å, confirmed by QCM, RBS and TEM measurement. The resistivity of 5nm Ru layer is 23.103 μohm·cm.

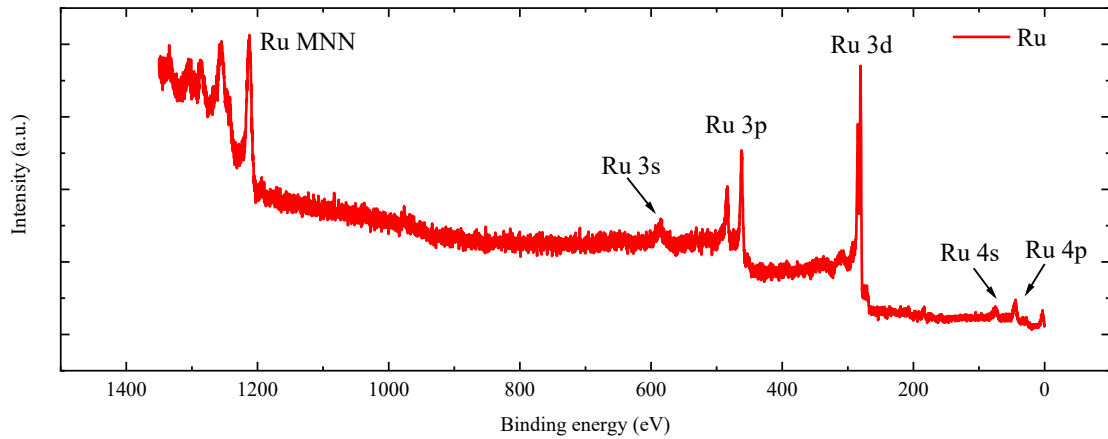


Figure 24: *In-situ* XPS spectra of 5nm Ru(0001) film by the XPS in Quince system.

The chemical cleanness of the film can be tested by *in-situ* XPS measurement, as shown in figure (24). The spectra only show the Ru peaks without oxygen 1s peak. From the RHEED monitoring of the whole deposition procedure, we can clearly see that the Ru follows the layer-growth mechanism. As the film grows thicker, the crystallinity turns better.

However, the thickness of Ru should be as thin as possible because of the shunting effect of the Ru layer in PPMS and ST-FMR measurement. After multiple deposition tests, the best thickness of Ru(0001) layer is found to be 5nm, in agreement with the RHEED data. However, 8.56Å(2UC) thickness can be achieved when the YSZ substrate has excellent quality. The crystal quality of Ru(0001) film can also be confirmed by *ex-situ* XRD measurement showing good out-of-plane crystallinity with Ru(0002) peak at 42.124°. The calculated out-of-plane lattice constant is 4.24Å.

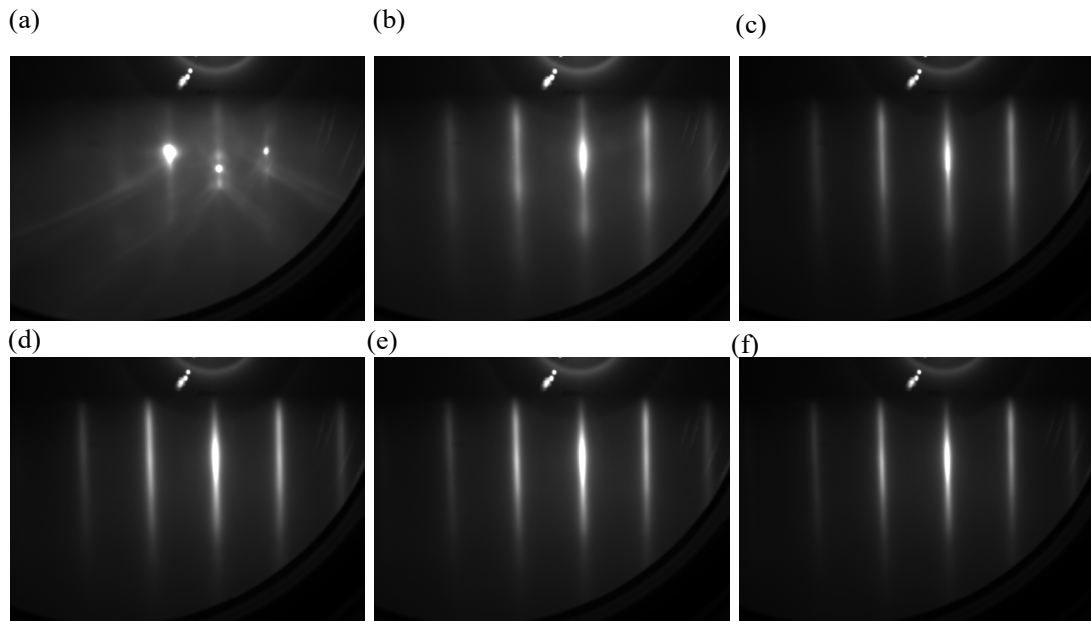


Figure 25: RHEED streaks of Ru(0001) film deposited on YSZ(111) perfect cut substrate. All pictures are taken along the YSZ(111) [10-1] direction. (a) YSZ substrate. (b) 1UC, (c) 2UC, (d) 4UC, (e) 8UC and (f) 12UC thick Ru(0001) film.

As for the Ru film deposited on the offcut substrate, the RHEED pattern also shows single crystal layered growth, with domains showing up slightly larger than on the offcut substrate. The typical thickness for Ru buffer layer is 5nm which is used for AHE and ST-FMR detection, the thinnest we can achieve is 1.5nm by carefully choosing the best quality offcut substrates. The 1.5nm Ru buffer has been used in switching experiment because with adding Pt layer, the shunting effect will be significant, so it is crucial to decrease the thickness of Ru layer and if possible, Pt layer.

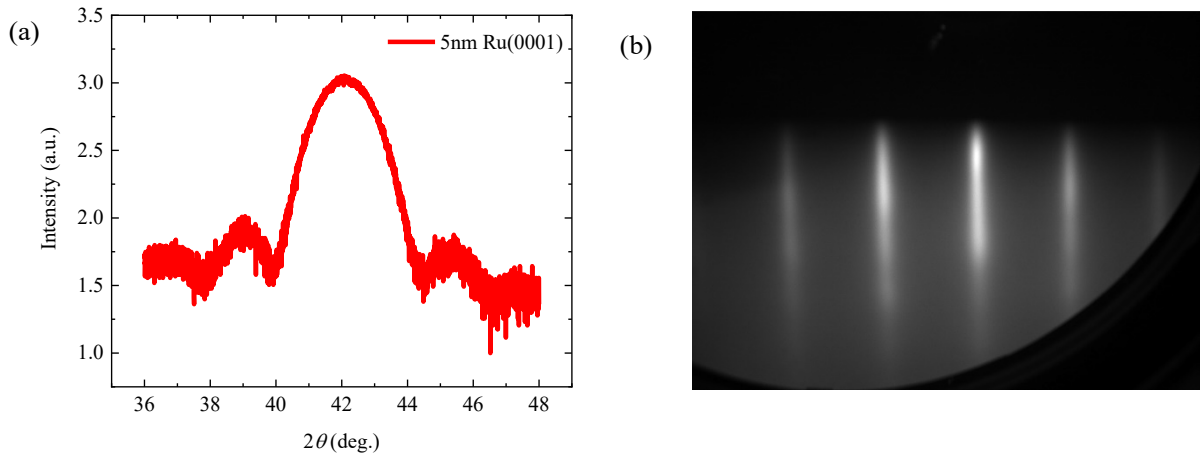


Figure 26: (a) XRD peak of Ru(0001) film on perfect cut substrate.(b) RHEED of 5nm Ru film deposited on YSZ(111) 3° offcut substrate.

3.2 Capping layers

I choose MgO as the capping layer of the stack as it can form transparent, solid and smooth layers on Ru(0001) and Mn₃Ge(0001). Note that the insulating MgO deposition at room temperature from the EBE can destroy a few layers of the stack below to form an insulating dead layer even if the deposition is carried out at room temperature. In order to control the thickness of the film below the MgO capping, we prefer to deposit 6.5Å Ru protective layer before the MgO deposition. By carefully estimating the thickness of the dead layer by depositing Ru films with different thicknesses followed by more than 3nm MgO deposition, one can see the split Ru 3d peak shows up when the Ru is thicker than 0.65nm from the XPS spectra of the Ru/MgO stack. This means the insulating dead layer thickness is around 0.65nm. The 0.65nm dead layer is also insulating, confirmed by the resistance measurement. So the protective layer consisting of metallic Ru layer should be around 0.65nm deposited at room temperature, then 10nm insulating MgO film. It is sufficient to protect the film after lithography and the sample stored in atmosphere more than one year.

From the RHEED and AFM images, it is evident that the MgO film is a smooth and continuous polycrystalline layer with RMS 3.6Å. XPS data shows MgO is clean and covers the whole sample stack.

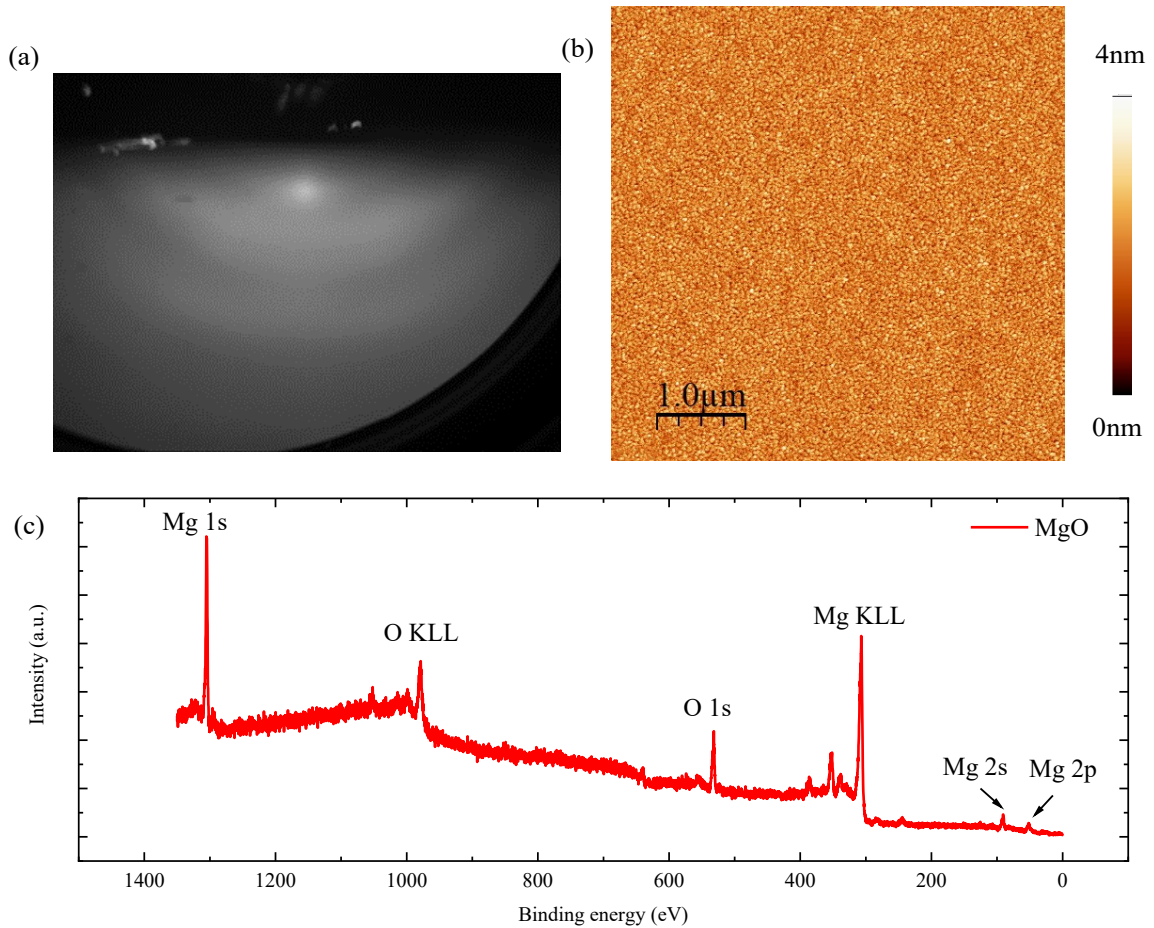


Figure 27: (a) RHEED, (b) AFM and (c) *in-situ* XPS of 10nm MgO capping on Mn₃Ge sample.

The growth rate of MgO layer is controlled to be around 250 s/Å, confirmed by QCM, RBS and TEM measurement. Slow growth rate secures the smooth surface and less interdiffusion.

3.3 Hexagonal D0₁₉ Mn₃Ge film

3.3.1 Perfect cut Mn₃Ge(0001) film

The composition of the Mn₃Ge film need to be carefully calibrated as when the Mn/Ge ration is higher than 3, the extra Mn can occupy the Ge atom position and introduce uncompensated Mn moment along the Z axis of the film. Moreover, extra Mn may form different kinds of Mn-Ge compounds which we don't want. First, to find the right composition, we try to deposit film on perfect cut YSZ(111) substrate.

With the help of XPS and RBS, the film deposited at 350° followed by 15min annealing at the sample temperature shows the composition of Mn₃Ge with non-split of Mn 2p and Ge 2p peaks meaning it is single phase. By measuring the RHEED pattern of the Mn₃Ge film along different in-plane direction, we calculate the distance of stripes from different direction to be around 1.76 which is close to be $\sqrt{3}$, this can confirm that the film is in hexagonal phase. If it is tetragonal or cubic phase, the ratio won't be close to 1.73. The epitaxial relationship among them is Mn₃Ge(0001)[11-20] // Ru(0001)[11-20] and Mn₃Ge(0001)[10-10]//Ru(0001)[10-10]. The calculated in-plane lattice constant of Mn₃Ge film is 5.34Å.

Moreover, with the help of XRD, we measure the 2theta-omega scan of 25nm Mn₃Ge(0001)/5nm Ru(0001) sample stack. From the XRD database, the position of Ru(0002) peak is at 42.152°, for hexagonal Mn₃Ge(0002) peak the position is at 41.866°. The measured peak at 41.9139° could be a mixed peak. By trying to separate the two possible sub-peaks, as we can see from the figure (29), it is clear that the peak we see is truly a mix of Ru(0002) peak at 42.222° and hexagonal Mn₃Ge(0002)

peak at 41.866° . The calculated out-of-plane lattice constant is 4.22\AA .

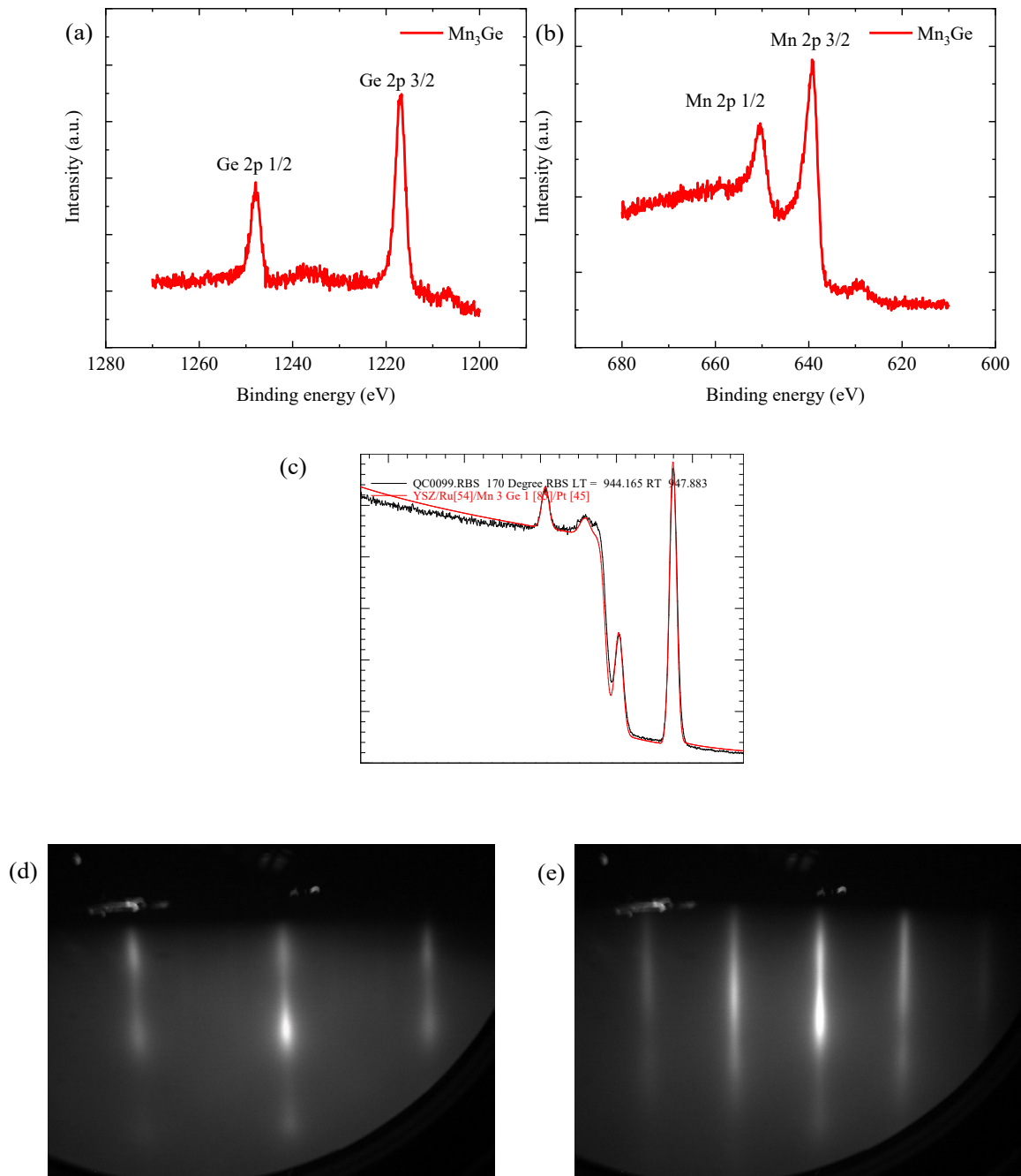


Figure 28: XPS spectra of (a) Ge-2p peak and (b) Mn-2p peak. (c) RBS data of the $\text{Mn}_3\text{Ge}/\text{Ru}$ stack. (d) Mn_3Ge RHEED pattern measurement along the $\text{Ru}(0001)$ $[11-20]$ direction. (e) Mn_3Ge RHEED pattern measurement along the $\text{Ru}(0001)$ $[10-10]$ direction.

Because Mn_3Ge will easily get oxidized if taken out to atmosphere without proper capping, we need to measure the surface topography with *in-situ* technology STM. With the help of STM, we measure the $10\text{nm } \text{Mn}_3\text{Ge}(0001)/5\text{nm } \text{Ru}(0001)$ sample

on perfect YSZ(111) substrate. The surface is smooth with RMS around 3.81\AA for 0.5nm scan range. The step height of the surface is 2.11\AA , which is close to thickness of one single layer of Mn_3Ge 2.16\AA , or we can see 0.5 unit cell thickness of $\text{Mn}_3\text{Ge}(0001)$. However, as the lattice mismatch in the sample, we can observe some screw dislocation on the surface.

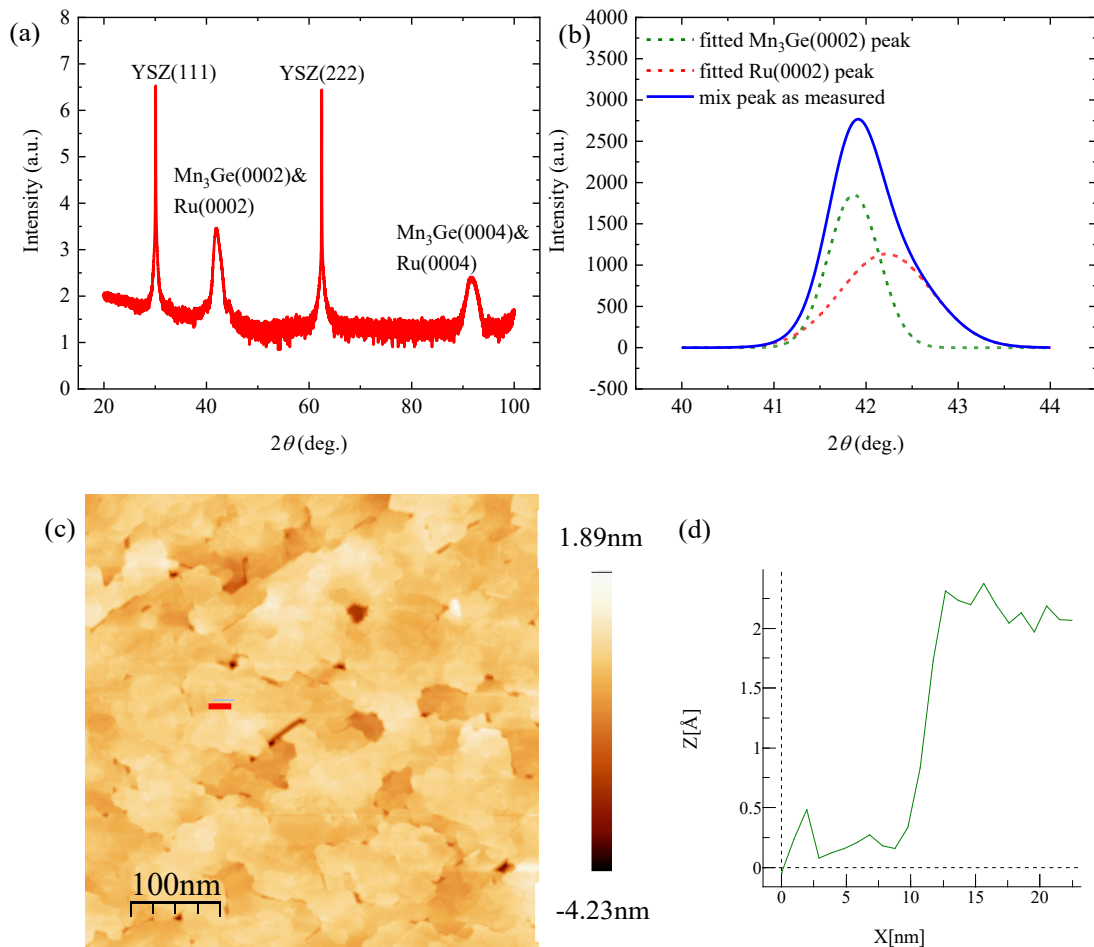


Figure 29: (a) XRD 2theta-omega scan spectra of 25nm $\text{Mn}_3\text{Ge}/5\text{nm}$ Ru sample with MgO capping. (b) the 41.9139° XRD mix peak with fitted subpeaks of $\text{Mn}_3\text{Ge}(0006)$ and $\text{Ru}(0006)$. (c) STM scan of 50nm $\text{Mn}_3\text{Ge}/5\text{nm}$ Ru stack. (d) height of one layer thickness of Mn_3Ge sample chose from figure (c).

By using the in situ QCM, we can find the preferred growth rate of Mn and Ge from 2 in 1 K-cell evaporator for Mn_3Ge deposition. The growth rate defines the amount of Mn and Ge atoms reaching the surface of the substrate to form the Mn_3Ge film. So

when the temperature of Mn and Ge source changes, the Mn/Ge ration will change in the sample. We already know that the material flux, or we can say the atom reaching the substrate, is only defined by the substrate temperature and the saturated vapor pressure of the source. if other chamber configuration didn't change, and we use a fixed substrate temperature during deposition, the flux can only be affected by the vapor pressure, or we can see the source temperature. So the source temperature is of extreme important for Mn₃Ge film deposition. However, when we refill the k-cell evaporator which may change the growth rate at the same source temperature as before or maintain the chamber which may change the chamber vacuum thus affect the source growth rate. It is more reliable to know the growth rate of each source as it can also reflect the beam flux value and the atoms reaching the sample position.

As we have the right film at 350°C deposition temperature, next we need to find the relationship of the Mn and Ge K-cell evaporator temperature (T_{Mn} and T_{Ge}) and the QCM growth rate of Mn and Ge. From my calibration, the composition of the films is Mn₃Ge when $T_{Mn}=670^{\circ}C / T_{Ge}=1000^{\circ}C$ or $T_{Mn}=710^{\circ}C / T_{Ge}=1050^{\circ}C$ or $T_{Mn}=730^{\circ}C / T_{Ge}=1080^{\circ}C$, with the growth rate to be $G_{Mn}=104 \text{ s}/\text{\AA} - G_{Ge}=201 \text{ s}/\text{\AA}$, $G_{Mn}=31 \text{ s}/\text{\AA} - G_{Ge}=59 \text{ s}/\text{\AA}$, $G_{Mn}=16.5 \text{ s}/\text{\AA} - G_{Ge}=31 \text{ s}/\text{\AA}$, respectively. The growth rate of Mn₃Ge film at different source temperature is $G_{Mn_3Ge}=60 \text{ s}/\text{\AA}$, $18 \text{ s}/\text{\AA}$ and $9 \text{ s}/\text{\AA}$ with respect to the 3 temperature conditions found. The relation of the source growth rate and composition of Mn₃Ge is quite solid, as I tested after a couple of maintenance. As the source growth rate is the sample as before, no matter what the source temperature is, we can always have Mn₃Ge film with the right temperature.

By keeping the Mn and Ge growth rate, Mn₃Ge films grown at temperature higher than

350°C tend to be amorphous with mixed phase of Mn-Ge compounds. Mn₃Ge films grown at temperatures lower than 350°C tend to be polycrystalline, also with mixed phase of Mn-Ge. Only the sample deposited at around 350°C, followed by 15min annealing at the sample temperature, can form single crystal Mn₃Ge(0001) film. Of course, we can repeat the calibration of the growth rate at new substrate temperature, however it is quite time consuming. So, we prefer to keep the growth temperature always at 350°C, annealing at the sample temperature for 15min.

The growth mode of Mn₃Ge keeps being layer growth even the film thickness is more than 50nm, as shown in figure (30).

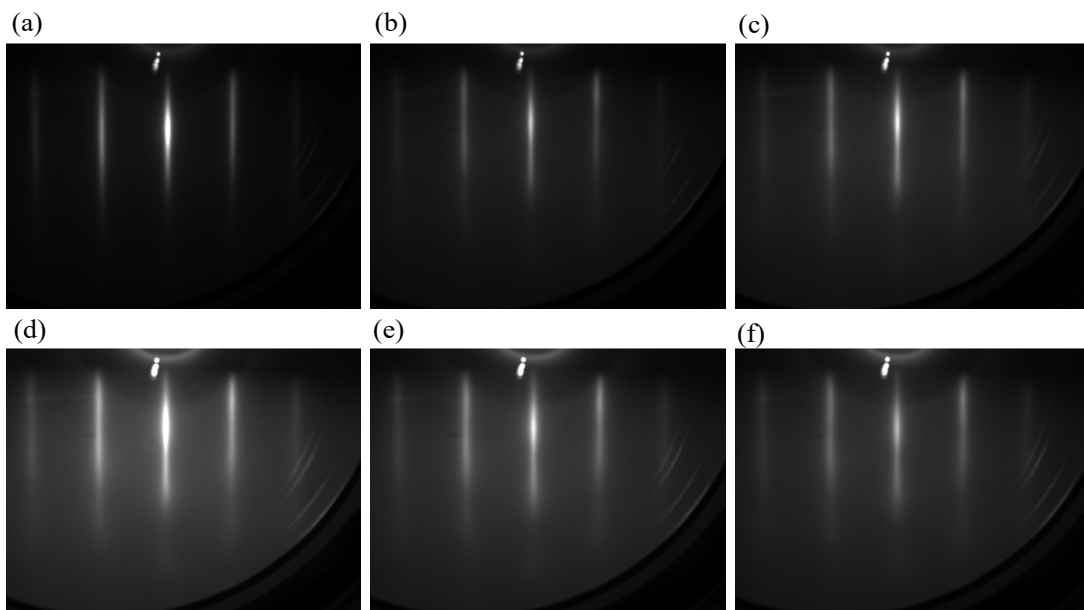


Figure 30: RHEED measured along the Ru(0001) [11-20] direction. (a) Ru film, (b) 2 nm, (c) 5 nm, (d) 25 nm, (e) 40 nm (f) 50 nm Mn₃Ge(0001).

To conclude, my approach to get the hexagonal Mn₃Ge film is, first, at a certain deposition temperature, calibrate the source temperature to grow the single crystal Mn₃Ge film, quality determined by RHEED and composition determined by XPS and RBS. The Mn/Ge ratio calculated from XPS spectra should be around 3 with no splitting

peaks which coincides with the RBS measured value around 3. Then measure the growth rate of each source by QCM and keep it at the same value after each chamber maintenance.

3.3.2 Offcut Mn₃Ge(0001) film

The Mn₃Ge film grown on the 3° offcut YSZ(111)K(211) substrate shares the sample deposition parameters as perfect cut YSZ(111) substrate. We have ordered the offcut YSZ(111) substrate with offcut angles being 3°, 6° and 10°. The roughness of the Mn₃Ge layer increases with the increase of the angle. So, for the AHE detection, we use YSZ(111)K(211) 3° offcut substrate for offcut Mn₃Ge(0001) films. K(211) means the (111) plane rotated to the (211) plane with the rotation axis along[011]. The reason to use the offcut substrates will be explained in chapter 4 in detail.

By analyzing the RHEED pattern, it seems the quality of the Mn₃Ge film is a little worse as it on the perfect cut YSZ(111) with multilevel stepped surface because the streaks are more or less modulated. This is quite acceptable as the offset Mn₃Ge should show a rougher surface as it is 3° tilted from the (0001) plane. STM data also confirm a rough surface with RMS being 8.46 Å. By measuring the XRD of different sample thicknesses, we find out as the thickness of Mn₃Ge layer increases, the full width at half maximum of the mix peak gets smaller, which indicates the crystallinity gets better. The calculated lattice constant from RHEED and XRD are $a=5.44 \text{ \AA}$, $c=4.20 \text{ \AA}$.

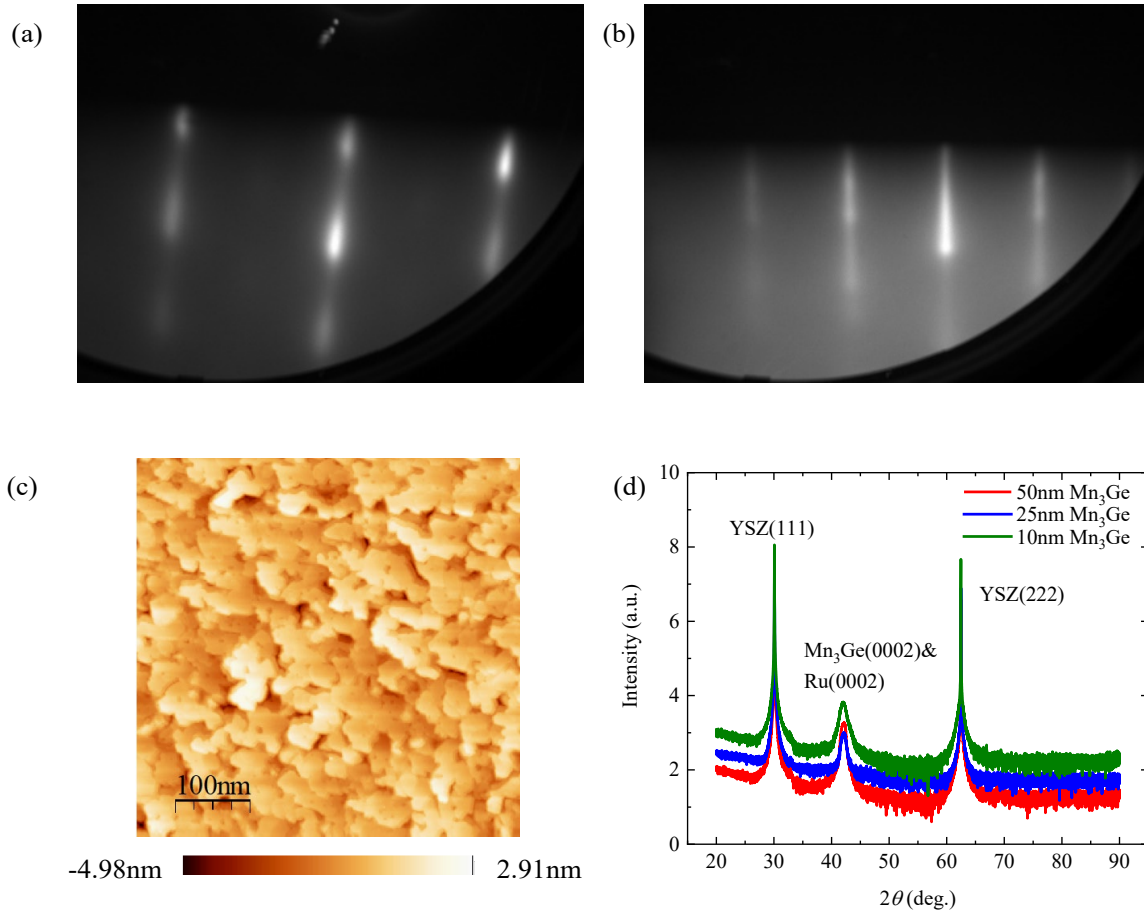


Figure 31: RHEED of $\text{Mn}_3\text{Ge}(0001)$ grown on YSZ offcut substrate, measured along (a) $[10-10]$ and (b) $[11-20]$ direction. (c) STM of 50 nm $\text{Mn}_3\text{Ge}/5$ nm Ru sample. (d) XRD of Mn_3Ge sample with different thicknesses from 10 nm, 25 nm and 50 nm.

3.4 Device fabrication

3.4.1 Hall geometry lithography

To measure the AHE and switching behavior of the Mn_3Ge films in a more precise and controllable way, it is better to fabricate Hall bar pattern on the sample. For me, I use two different hall geometries for the transport measurement. One is a 6-foot hall bar device that can allow us to measure the R_{xx} and R_{xy} at the same time. The other one is a 4-foot hall bar pattern that can be used to measure the switching voltage vertical to the direction of current.

The ratio of the length and width of the 6-foot hall bar is fixed to be 4:1 and the width of the hall bars are 100 μm , 50 μm , 25 μm and 10 μm . The length of the 6-foot hall bar is the distance between the R_{xx} measuring feet. The 4-foot hall bar has two size standards. One is fixed ratio like 6-foot pattern with the width being 50 μm , 100 μm and 10 μm , the other one has fixed hall bar width 10 μm with different length being 40 μm , 60 μm , 80 μm and 100 μm . The width of the 4-foot pattern is defined as the length of the charge electron flow path. The width of the feet in the mentioned patterns above is 5 μm .

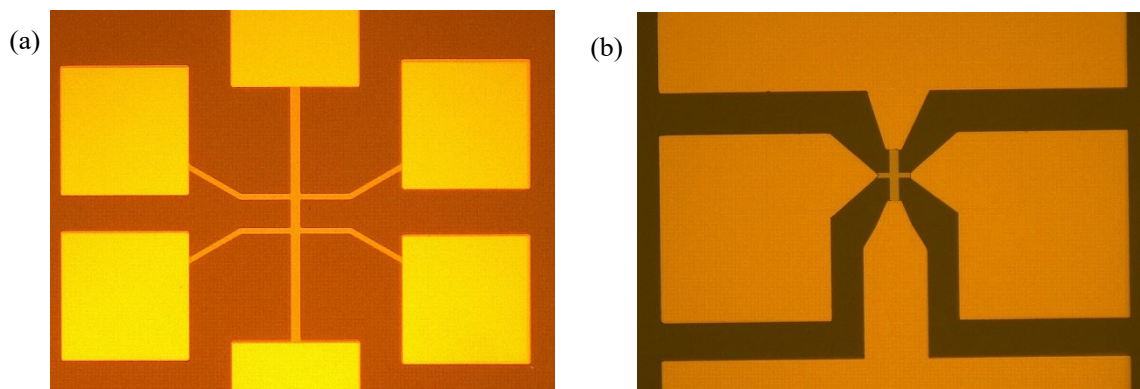


Figure 32: (a) 6-foot hall bar device with 10 μm width and 40 μm length. (b) 4-foot hall bar width 10 μm width and length 60 μm length.

When designing the pattern using the LayoutEditor software, we need to set different hall bars with 90° angle with hall bars in the sample size, so that we can measure the data along [11-20] and [10-10] directions of the hexagonal (0001) sample. Also, we need to have two overlay designs. First layer is for having the hall bar pattern and second layer is for the Ru/Au contact deposition on the hall bar.

The optical lithography is carried out in the institute cleanroom. The typical steps for the hall bar pattern lithography are: (1) Clean the sample with solvent, then spin-coat the sample using commercial ARP-3540T positive Photoresist. (2) Use the UV laser writer to expose the design of pattern on the resist. (3) Lift off the sample in the AR300-

44 developer. (4) Check the quality of the developing process and size of the pattern on the sample. (5) Put the sample in the ion milling system to etch the pattern on the surface of the sample, use the RGA in the system to monitor the etching rate of each layer. (6) After the etching, soak the sample in acetone and clean it by ultrasonic machine. (7) Check the quality of the etching and size of the structure after cleaning. Now there are hall bar patterns on the sample.

Next, we need to deposit the Ru/Au contact pad on the hall bar as the sample is covered with insulating MgO capping. Directly bond the wire on the capping is possible as the bonding machine will penetrate through the whole sample, however there will be large barrier on the contact that can affect the movement of the electrons. To deposit Ru/Au contact on the hall bar, we need to first repeat step (1) to (4), then in the ion milling machine, first etch off the capping layer on certain regions using the etching rate obtained from previous step (5), then deposit 2 nm Ru and 50 nm Au in the sample chamber. Then repeat the step (6) to (7). Now we can have hall bars on the sample with Ru/Au contact.

This 2-step overlay lithography need to align the second contact pattern with the first hall bar pattern during the UV writing process, so that the sample is at the right position for the second contact pattern to be lift off at the desired part of the hall bar.

Another important step is the UV laser writing. We need to set the dose for the UV laser machine. For a chosen resist thickness (normally 1.4 μm for the resist I choose), if the dose is too small, resist will not be removed as desired after development; If the dose is too high, the size of the pattern will be smaller than design. So normally, at the beginning we need to run a dose test to have pattern exposed at different dose power,

after developing, we can choose the best-exposed pattern (the one with clean resist pattern and sharp edge with right size) to use its dose for later lithography.

As for the development time during the developing process, we calibrate the time of development to ensure that structures are not swollen, meanwhile maintaining the unexposed resist as the hall bar pattern (meaning the right size). So, we also need to run a developing test to find the right time.

After a successful lithography, the sample will be ready for transport development.

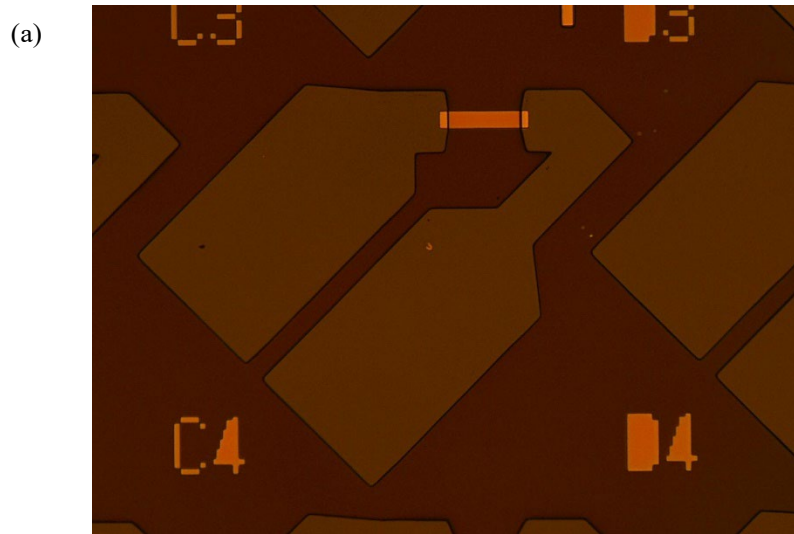
3.4.2 ST-FMR geometry lithography

ST-FMR pattern lithography shares the sample procedure as the hall bar pattern lithography. The only difference is the pattern design itself.

The basic ST-FMR pattern can be seen in the figure below. The angle between the pattern bar and the edge of the bottom contact is fixed at 45° and the bar is parallel to the sample edge, so when we align the sample in ST-FMR, we can set external field parallel to the edge of the bottom contact when the pattern bar is parallel to one of the in-plane directions so we can have more or less the maximum signal.

So, we need to set 2 groups of pattern series, with sample bars one group parallel to one edge of the sample and the other group perpendicular to it. As seen in figure (33).

By using the same lithography process as for the Hall bar pattern fabrication, we can have high-quality film bar and Ru/Au contact forming a ST-FMR device ready for measurement.



(b)

A1	L = 100 W = 50	B1	L = 100 W = 50	C1	L = 90 W = 50	D1	L = 80 W = 50	E1	L = 75 W = 50	F1	L = 70 W = 50	G1	L = 60 W = 50	H1	L = 50 W = 50
A2	L = 100 W = 25	B2	L = 80 W = 25	C2	L = 75 W = 25	D2	L = 70 W = 25	E2	L = 60 W = 25	F2	L = 50 W = 25	G2	L = 40 W = 25	H2	L = 25 W = 25
A3	L = 100 W = 20	B3	L = 80 W = 20	C3	L = 70 W = 20	D3	L = 60 W = 20	E3	L = 50 W = 20	F3	L = 40 W = 20	G3	L = 30 W = 20	H3	L = 20 W = 20
A4	L = 100 W = 15	B4	L = 80 W = 15	C4	L = 75 W = 15	D4	L = 50 W = 15	E4	L = 45 W = 15	F4	L = 40 W = 15	G4	L = 30 W = 15	H4	L = 15 W = 15
A5	L = 100 W = 10	B5	L = 75 W = 10	C5	L = 60 W = 10	D5	L = 50 W = 10	E5	L = 40 W = 10	F5	L = 30 W = 10	G5	L = 20 W = 10	H5	L = 10 W = 10
A6	L = 100 W = 5	B6	L = 75 W = 5	C6	L = 50 W = 5	D6	L = 40 W = 5	E6	L = 30 W = 5	F6	L = 20 W = 5	G6	L = 15 W = 5	H6	L = 10 W = 5

Figure 33: (a) One design of the ST-FMR device C4 with 75 μm length and 15 μm width. (b) Size of different ST-FMR patterns. L means length and W means width. The values showed are in μm unit.

4 Transport and magnetic properties of $D0_{19}$ Mn_3Ge films

4.1 Transport measurement for AHE

4.1.1 Shunting effect from buffer layer

The resistivity of 5nm Ru layer is $23.103 \mu\text{ohm}\cdot\text{cm}$. For Mn_3Ge film resistivity, we need to measure the resistance of 5 nm Ru/50 nm Mn_3Ge capped sample, then consider the conductive layer Ru and Mn_3Ge are in parallel connection. By Kirchhoff Circuit Law and Ohm law, we can extract the Mn_3Ge resistance from the total resistance, thus we can get the resistivity of Mn_3Ge layer is $329.987 \mu\text{ohm}\cdot\text{cm}$. By comparing the two value, it is obvious that in the bilayer structure with Ru thickness being d_{Ru} and Mn_3Ge thickness d_{Mn_3Ge} , $\frac{I_{Ru}}{I_{Mn_3Ge}} = \frac{\rho_{Mn_3Ge}}{\rho_{Ru}} \times \frac{d_{Ru}}{d_{Mn_3Ge}} = 14.283 \times \frac{d_{Ru}}{d_{Mn_3Ge}}$. For 50nm Mn_3Ge /5nm Ru stack, $\frac{I_{Ru}}{I_{Mn_3Ge}} = 1.4283$, meaning 55% of the current flow through the Ru layer, which is obviously a shunting effect. When measuring the bilayer structure voltage under field, there will be a mix of Ru layer Hall voltage, Mn_3Ge layer ordinary Hall voltage and berry-curvature-driven Mn_3Ge layer voltage.

To extract the Mn_3Ge film transport data from the mixed data for AHE measurement, we need to do as follows. (1) Measure the sample with Ru/ Mn_3Ge stack, let's say, for the voltage versus field data, voltage versus temperature and voltage versus rotation angle data. (2) Measure the sample with only 5 nm Ru layer, with the same sample hall bar parameters and the same measurement current. (3) By knowing the resistance of the

Ru and Mn₃Ge layer at zero field, we can calculate the current flow through the Ru and Mn₃Ge separately, we can transform the Ru data from step (3) to the new Ru layer voltage data with the same Ru layer current in Ru/ Mn₃Ge sample. (4) According to the new Ru layer voltage data, calculate the ordinary Mn₃Ge layer voltage data. (5) For field dependence measurement, pure berry-curvature driven Mn₃Ge layer voltage can be acquired by subtracting the ordinary Ru layer and Mn₃Ge layer voltage curve directly from the mixed voltage data. For angular dependence measurement under specific field and temperature dependence measurement for field cooling and zero field cooling, follow the sample protocol as the field dependence data. The berry curvature-driven AHE conductivity calculated from above method is $14.8 \Omega^{-1}\cdot\text{cm}^{-1}(\mu_0H = 0\text{T})$ and it is nearly independent from film thickness changing, meaning that we observe Berry curvature driven AHE down to thickness as low as 25 nm. For the subsequent AHE measurement, all the data shown are pure Mn₃Ge layers without the ordinary voltage data, using the method introduced in this section.

4.1.2 AHE measurement

To measure the AHE of the Mn₃Ge layer, use the offset substrate. As from the introduction in chapter 1, $\sigma_{xy}^z, \sigma_{yz}^x$ should be exact zero, σ_{xz}^y should have nonzero value. However, with the weak in-plane symmetry broken owing to the tiny IP residual moment, it gives rise to a perturbation of the mirror symmetry, for example, shifting slightly the mirror image of a Weyl point from its position expected, as we will see in the surface states of Mn₃Ge. Thus, it is possible for $\sigma_{xy}^z, \sigma_{yz}^x$ to show tiny non-zero value. If there are no extra Mn atoms in the Mn₃Ge film with out-of-plane tilted moments, σ_{xy}^z should be zero. To measure the Anomalous Hall signal from

the Mn₃Ge sample, we have to make sure that the field should have a component along the [10-10] or [11-20] direction of the Mn₃Ge(0001) film. For now, all the published papers about Mn₃Ge and Mn₃Sn thin films targeting the AHE measurement have two ways to grow the films, they can either grow polycrystalline film or grow the (10-10) films on MgO(110) substrate, all by magneton sputtering method. The Mn₃Sn(10-10) films have in-plane direction of [0001] and [11-20], so the out-of-plane field is along the [10-10] direction which will give rise to the highest anomalous Hall conductivity signals. However, for films grown by MBE method, it is almost impossible to have high quality (10-10) films as they do not favor the lowest surface energy states of the films, the film will be pretty rough following the island growth mode, along with polycrystalline behavior and multi Mn-Ge phase, sometimes even shows amorphous behavior. Recently there is a Nature paper published about full switching Mn₃Sn Stack prepared by MBE method which could get very high-quality sample.

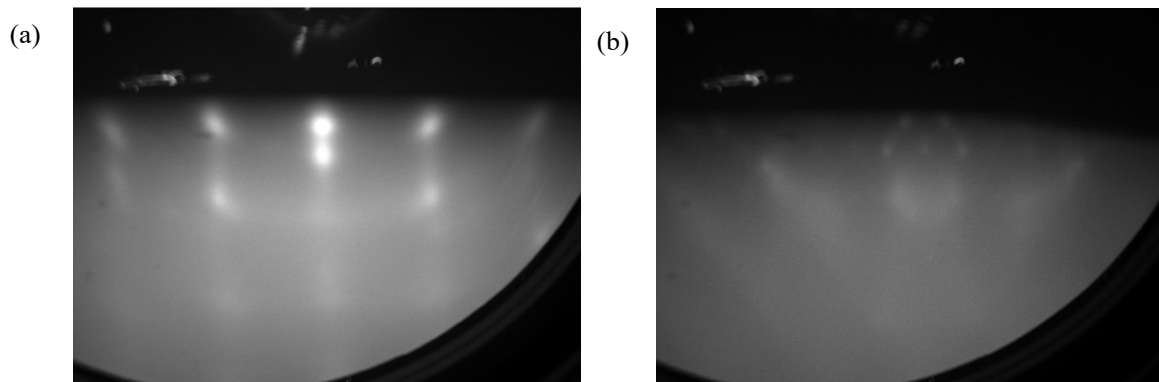


Figure 34: RHEED pattern of Mn₃Ge films grown on (a) YSZ(110) and (b) MgO(110) substrates.

So, based on the fact that I can grow high-quality Mn₃Ge(0001) films on YSZ(111) substrate, I come up with an idea of growing the offset Mn₃Ge(0001) films on offset YSZ(111)K(211) substrate. The film is tilted from [0001] normal axis and (0001) plane

is tilted with the rotation axis of [11-20], the angle between the basal plane of the film and the (0001) plane of the film equals to the angle of the offcut substrate (111) plane to the basal plane. When applying the out-of-plane field on the in-plane Hall geometry pattern, there will be a [10-10] component of the field lies in the Kagome plane which will induce anomalous Hall signals. When current flows along [11-20] direction, the Hall voltage signal will have [0001] direction component with respect to the [10-10] direction magnetic field component. As for the current flows along the direction perpendicular to [11-20] direction, the [0001] direction current component and [10-10] direction field component will induce Hall signal along [11-20] direction. Note that in the offcut $\text{Mn}_3\text{Ge}(0001)$ film, the direction [10-10] and [0001] are all tilted, for simplicity, we still call them [10-10] and [0001] direction in the following thesis discussion.

To measure the AHE of the Mn_3Ge film, I grow 5 nm Ru(0001) film as buffer layer on YSZ(111)K(211) 3° offcut substrate, followed by the deposition of Mn_3Ge film with variable thickness and the capping stacks. Considering the high conductivity of the Ru layer, I use Mn_3Ge layer with 50nm thickness for AHE measurement. After various calibrations for lithography, we set the hall bar size to be 10 μm width, 40 μm length and 5 μm hall bar feet width.

To keep the consistency of the data, we use 9T and 14T Dynacool PPMS for AHE measurement. Samples are mounted on the same standard puck, OP rotation puck for measurement. First, we measure the offcut Mn_3Ge stack, then the Ru background stack. By subtracting the Ru signal from the raw data, we could have the pure Mn_3Ge layer data. By repeating the subtracting process for every measurement sequence, we can get

the data needed to investigate the Mn₃Ge film. The current source is set to 1 mA during the experiment.

First, we measure the transverse conductivity of the Mn₃Ge versus the external field with current along different in-plane directions, external magnetic field along the [0001] direction at room temperature 300K, as shown in figure 35(a). When current flow along [11-20] direction, the zero-field conductivity, saturated conductivity, coercive field are all larger than the [10-10] direction. However, the zero-field conductivity of the offcut Mn₃Ge film along [10-10] is smaller than the bulk value which is around 50 ohm⁻¹·cm⁻¹, as expected as in the offcut sample, the output signal only reflects part of the in-plane property of Mn₃Ge. Then we keep the direction of the field out-of-plane and current along [10-10] direction, we measure the transverse conductivity as the function of field at different temperatures at 5K, 100K, 200K, 300K, 400K, shown in figure 35 (b). Mn₃Ge bulk samples have been reported to have a transition temperature varies from 380K to 420K^[18], normally when Mn₃Ge has a better crystal quality with large-scale AF order, it needs more thermal energy to break the AF order, thus leading to higher transition temperature. In figure 35 (b), as the temperature increases from 5K to 300k, the zero-field conductivity and 9T conductivity decrease as expected. However, at 400K, the two values did not change too much as they are at low temperature which means the thermal effect on the AHE of the film has more or less saturated. Moreover, this means the sample can keep the AF order at as high as 400K, Same behavior can also be observed when current flows along [11-20] direction in Figure 35 (c). Figure 35 (d) shows the negative magnetoresistance behavior of the Mn₃Ge film at 300K when current flows along [11-20] direction. The peak of the longitudinal resistivity is at the same field value of the coercive field of the transverse conductivity.

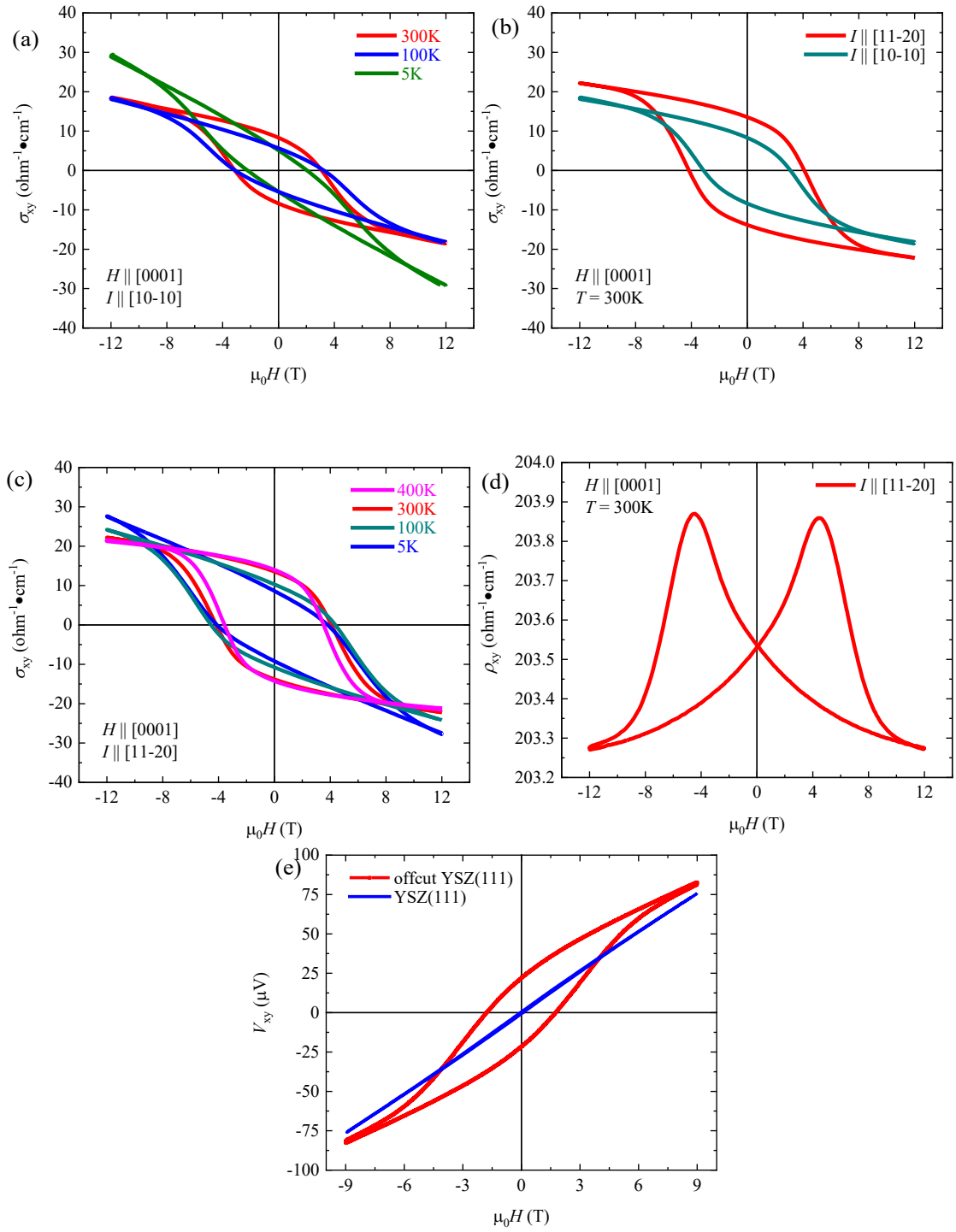


Figure 35: AHE measurement data. Transverse conductivity as a function of out-of-plane external magnetic field with current (a) along different in-plane directions at 300K, (b) along [10-10] direction at 5K, 100K, 200K, 300K, (c) along [11-20] direction at 5K, 100K, 200K, 300K. (d) longitudinal resistivity versus external magnetic field of the Mn₃Ge film at 300K with current along [11-20]. (e) comparison of the V_{xy} versus field loop of Mn₃Ge films grown on offcut YSZ(111) substrate and perfect cut YSZ(111) substrate with the sample stack thickness of 50nm.

Compared with the linear behavior of the transverse resistivity versus field of the

Mn₃Ge film grown on perfect cut YSZ(111) substrate, offcut Mn₃Ge film can not only keep the high quality of the sample as same as the perfect grown Mn₃Ge, but also can allow us to probe the in-plane property of the AF order by exposing it under tilting. As shown in figure 35(e), compared with the linear Hall behavior of Mn₃Ge(0001) grown on perfect cut YSZ(111) sub, Mn₃Ge film with the same thickness of 50nm Grown on offcut YSZ(111) indeed shows AHE behavior as expected. However, as the (0001) plane of Mn₃Ge is not fully out-of-plane, the conductivity value we detect are much smaller compared with bulk sample and the typical coercive field is much larger. Nevertheless, by successfully detect the AHE signal of the Mn₃Ge film, we can add spin sink layer to the stack to manipulate the spin texture of the Mn₃Ge film, as already reported on polycrystalline and single crystalline Mn₃Sn film. It is worth mentioning that Nakatsugi group grows high-quality Mn₃Sn[10-10] film on MgO(110) substrate with W(211) as middle layer^[45].

4.2 Magnetic measurement

4.2.1 Magnetic measurement for essential magnetic property

As Mn₃Ge are reported to show AF behavior with very small magnetization in all three direction($\sim 0.005 \mu_B/\text{Mn}$ in-plane and $\sim 0.0007 \mu_B/\text{Mn}$ along [0001] direction)^[18], to achieve the best accuracy for the MPMS measurement, we need to follow specific steps for the measurement. During the sample preparation, we need to use metal-free plastic or ceramic tools and keep the working space free from metallic contamination.

(1) Cut the YSZ(111) substrate into around 3.2 mm×5.2 mm smaller pieces before

deposition. As YSZ(111) is quite harder than most substrates and can easily crack into irregular shape pieces when pushed with too much force, we must be very careful when cutting it with a diamond pen. Sometimes the shape of the substrate may not be rectangular, we can weigh the piece to record the weight value instead of size so that we can easily calculate the volume of the substrate.

(2) Deposit 5 nm Ru/500 nm Mn₃Ge and capping layers on one piece and 5 nm Ru with the same capping on the other piece as the background piece. Thick Mn₃Ge layer leads to larger output signal. However, as the thickness increases from 200 nm, the Mn₃Ge layer is likely to get rough and protentional polycrystalline behavior. Hence, during deposition, one need to check the *in-situ* RHEED pattern to decide if the Mn₃Ge sample has a good quality for further measurement.

(3) Measure the two pieces using the same straw for the out-of-plane field and quartz rod for in-plane field measurement. Then subtract the background loop from the full stack loop, so we could have pure Mn₃Ge diagram.

To investigate the magnetic property of the Mn₃Ge film, we measure the Magnetization versus field at 5K and 300K along [0001], [10-10] and [11-20] direction of the 500nm Mn₃Ge grown on offcut substrate, as shown in figure 36 (a) and (b). In Figure 36 (a), there is no in-plane anisotropy regarding the magnetization at 5K. The value of the out-of-place magnetization at zero field is around 0.0003 $\mu_B/\text{Mn}_3\text{Ge}$, which is smaller than the in-plane value 0.009 $\mu_B/\text{Mn}_3\text{Ge}$. This out-of-plane magnetization indicates possible Mn spin tilting along *c* axis. The coercive force is 25 Oe at 5K. The loops measured at 300K are similar to 5K data,

except that the high field magnetization along (0001) direction is highly suppressed at room temperature while the in-plane values do not get obviously affected by temperature change.

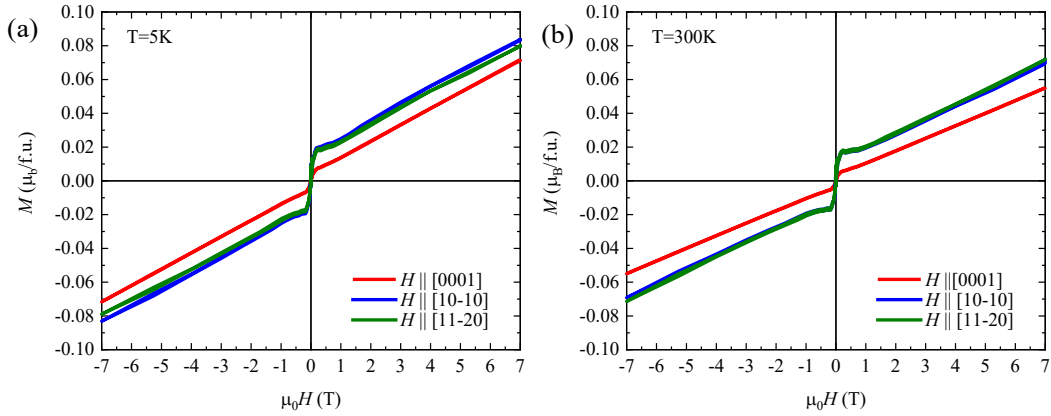


Figure 36: Field dependence of magnetization measured at (a) 5K and (b) 300K along three different directions.

Figure 37 shows the 9T field cooling and zero field cooling diagram of the 500 nm offcut Mn_3Ge film from 5K to 400K with field along $[10-10]$ direction. During measurement, we apply a small field of 0.1T field when collecting data to make sure the output signal is large enough. By comparing the two curves, we can conclude that the transition temperature of the Mn_3Ge film is higher than 400K which already exceeds the maximum temperature of the MPMS system. With the temperature getting close to the transition temperature, the magnetization value decreases.

To precisely determine the transition temperature of the Mn_3Ge film, we need to reach at least 450K for magnetic property measurement so that the transition can be seen in the diagram. Unfortunately, typical MPMS can only reach 400K. However, we can conclude that the Mn_3Ge film shows extremely small in-plane

and out-of-plane magnetization which coincides with the in-plane spin texture and the values are comparable with the published papers. The magnetization versus temperature measurement confirms the high transition temperature of more than 400K.

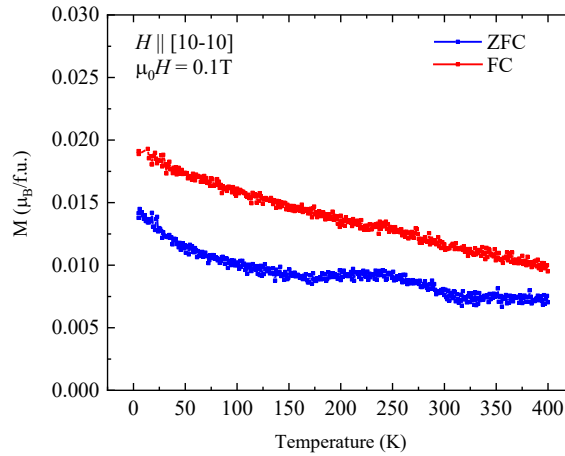


Figure 37: 9T field cooling and zero field cooling measurement of 500 nm offcut Mn_3Ge film along [10-10] direction.

4.2.2 ST-FMR measurement for SHE

The stack we use in the research is Ru(5 nm)/ Mn_3Ge (50 nm)/Py(6 nm)/MgO capping(10 nm), with Cu layer(0.6 nm) between Mn_3Ge layer and Py layer if necessary.

In-situ XPS and RBS are used to determine the purity of the evaporation of the material and the composition of the Mn-Ge layer to be Mn_3Ge . Structural analysis is performed by XRD using a Bruker d8 discover diffractometer. STM and AFM measurements are performed to probe the surface topography of Mn_3Ge layer and the whole stack.

ST-FMR devices were fabricated using ultra-violet (UHV) lithography and Ar ion milling. Stripes are first patterned along the in-plane direction [10-10] and [11-20] of

Mn₃Ge (0001) film, followed by the deposition of 100nm Au contact electrodes to form an efficient ST-FMR pattern. A homemade room temperature ST-FMR system is used for the measurement, with 20 dBm RF power and RF frequency varying from 9 to 13 GHz.

As shown in figure 38 (a), the *in-situ* RHEED images of the Mn₃Ge layer along the different in-plane directions show sharp streaks, which indicate the excellent in-plane crystallinity and smooth surface of the Mn₃Ge film during the layered growth process. By rotating the sample by 30° along the normal axis of the sample, one can change the RHEED pattern from one to the other. This also indicates the hexagonal crystallinity of the Mn₃Ge film. The epitaxial relationship among them is YSZ (111) [10-1] || Ru (0001) [11-20] || Mn₃Ge (0001) [11-20]. The STM image of the Mn₃Ge layer shown in figure 38 (c) also confirms the smoothness of the 50nm Mn₃Ge layer surface with a rms of 3.81 Å over the 500×500 nm² scanning area, with a monolayer thickness of 2.11 Å of in-plane hexagonal domains. The lattice constant of Mn₃Ge (0001) layer calculated from the RHEED^[29, 46] and STM data is $a = 5.43 \text{ \AA}$, $c = 4.22 \text{ \AA}$, which is close to the bulk value of $a = 5.35 \text{ \AA}$, $c = 4.31 \text{ \AA}$ ^[7, 18, 22]. Figure 38 (b) shows a representative XRD 2θ-ω scan of the standard sample with 10nm MgO capped 6nm Py (111)/50nm Mn₃Ge (0001)/5nm Ru (0001) stack on YSZ (111) substrate. Clear Py (111) peak and the mixed peak of Mn₃Ge (0002) and Ru (0002) can be seen in the scan range. After splitting the Mn₃Ge and Ru diffraction peak from the mixed peak, the Mn₃Ge peak position ($2\theta = 41.865^\circ$) gives $c = 4.31 \text{ \AA}$. The XPS measurement confirms the film's purity and the composition of the Mn₃Ge layer along with the RBS measurement. AFM image shown in figure 38 (d) gives the rms 3.6 Å scanned on the MgO capping layer over 5×5 μm² area. All the above measurement confirms the high quality of the sample which is

crucial for the ST-FMR measurement.

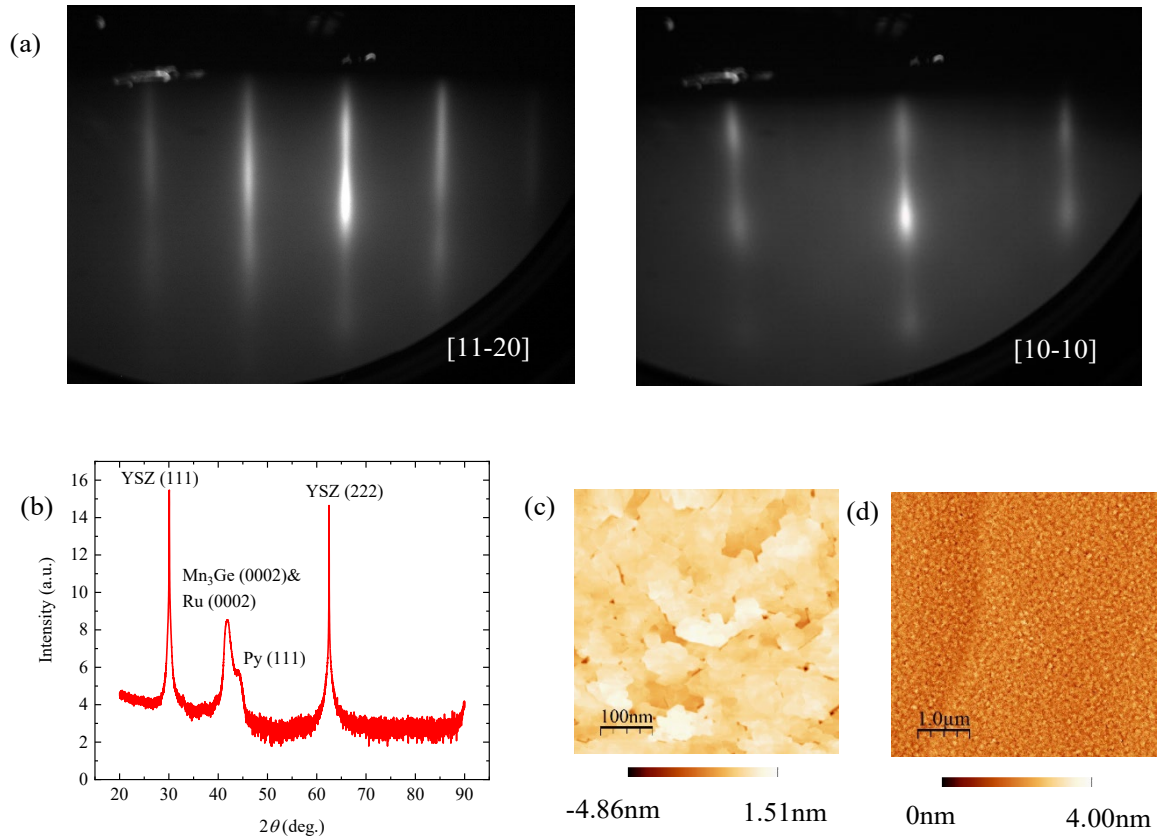


Figure 38: (a) RHEED pattern of 50nm Mn_3Ge (0001) film grown on 5nm Ru buffer layer, along [11-20] and [10-10] direction. (b) XRD spectra of 10nm MgO capped 6nm Py (111)/50nm Mn_3Ge (0001)/5nm Ru (0001) stack on YSZ (111) substrate. (c) STM topography of 50nm Mn_3Ge (0001) film over $500 \times 500 \text{ nm}^2$ area with the rms of 3.81 Å. (d) AFM image of the whole stack over $5 \times 5 \mu\text{m}^2$ area showing the rms of 3.6 Å.

After fabricating the sample into ST-FMR pattern via UHV lithography and ion milling/deposition, room temperature ST-FMR measurement is employed on the pattern with the stripe along the Mn_3Ge (0001) [10-10] and [11-20] in-plane direction, as shown in figure 39 (a) and (b) for the 50 nm Mn_3Ge /6 nm Py stack, (c) and (d) for the 50 nm Mn_3Ge /0.6 nm Cu/6nm Py stack.

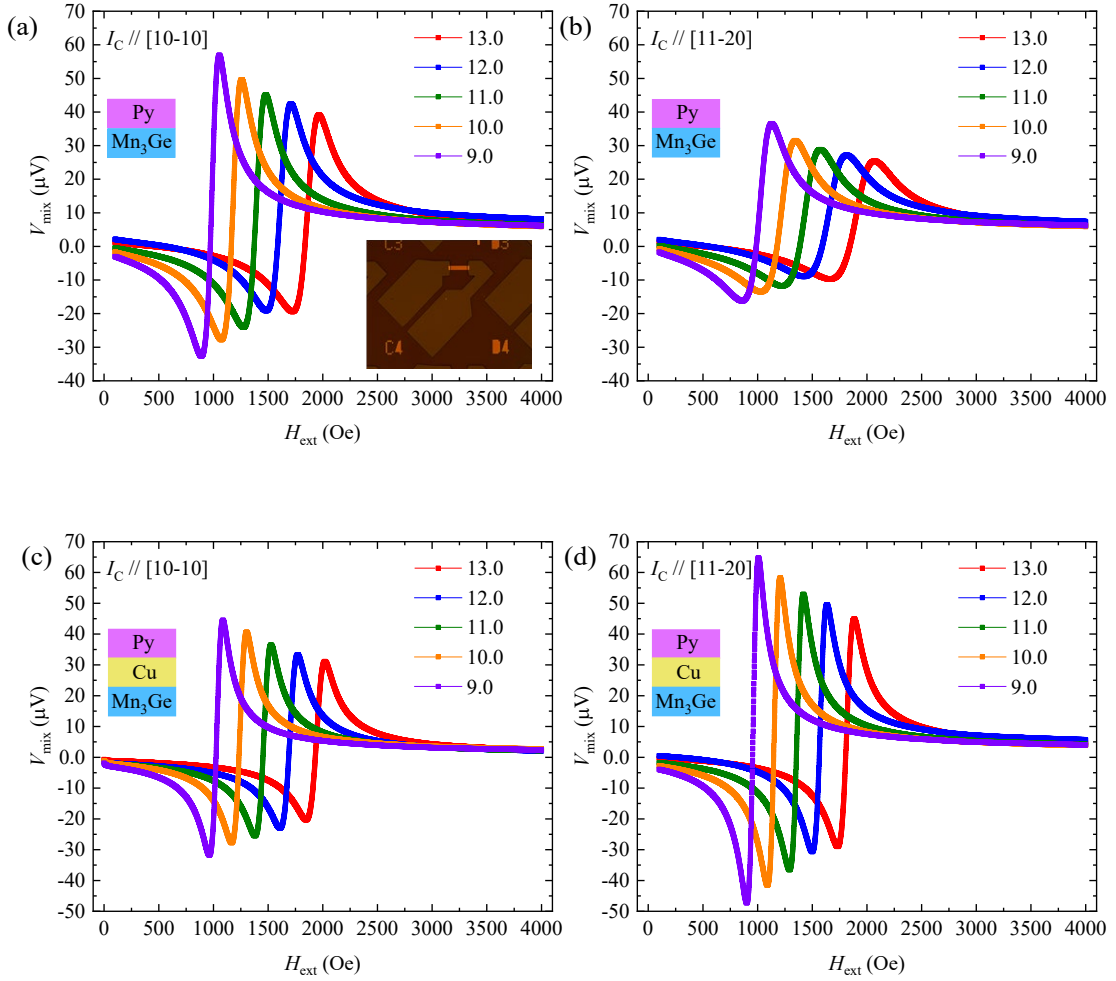


Figure 39: ST-FMR spectra of a 6 nm Py (111)/ 50 nm Mn₃Ge (0001) sample along (a) [10-10] and (b) [11-20] directions. Inset: a device C4 for ST-FMR measurements with a length of 75 μm and a width of 15 μm . ST-FMR spectra of the structure 6nm Py (111)/0.6 nm Cu (111)/50 nm Mn₃Ge (0001) along the (c) [10-10] and (d) [11-20] directions.

By fitting the ST-FMR spectra into the equations above, we can first obtain the resonance field H_0 , linewidth Δ and other useful parameters at different resonance frequencies f varying from 9 GHz to 13 GHz, then plot Δ over f to calculate the Gilbert damping coefficient α from the slope of the plot. Then plot f over H_0 for the fitting of Kittel formula to determine the demagnetization field of the ferromagnet layer Py, then we can calculate the SHC and SHA from the equations above.

Determined from the ST-FMR spectra of the 50 nm Mn₃Ge/6 nm Py stack shown in figure 39 (a) and (b), the damping coefficient of the stack is $\alpha = 0.028$ for the [10-10] charge current direction and 0.054 for the [11-20] charge current direction at 11 GHz RF frequency. Both values are higher than the 6nm Pt/6nm Py stack sample ($\alpha = 0.015$). The enhanced damping is the result of the spin pumping at the interface^[22, 47]. The calculated SHA and SHC at 11GHz for the [10-10] direction is $\theta_{SH} = 0.177$ and $\sigma_S = 2226 (\hbar/e)(\Omega \cdot m)^{-1}$, for the [11-20] direction is $\theta_{SH} = 0.196$ and $\sigma_S = 2528 (\hbar/e)(\Omega \cdot m)^{-1}$ (figure 40 (a) and (b)), which are all comparable with the reported value^[7, 21, 22].

To further investigate the possible interface contribution to the SHA and SHC, 6Å of Cu is used as the inserting layer between the AF Mn₃Ge and FM Py layer. The ST-FMR spectra are shown in figure 39 (c) and (d). Cu is considered as the spin transparent layer so that the spin current can flow freely through it. Moreover, as an inserting layer with the effective thickness of 6 Å, it could eliminate the interface exchange bias between Mn₃Ge and Py while still allowing for the spin current generated from the Mn₃Ge layer to be injected into the Py layer via SOT^[47-50].

The calculated damping coefficient is $\alpha = 0.016$ for both in-plane directions. Compared with the non-inserting Mn₃Ge/Py stack, the lower α indicates lower spin pumping at the interface. The calculated SHA and SHC at 11GHz for the [10-10] direction is $\theta_{SH} = 0.129$ and $\sigma_S = 1624 (\hbar/e)(\Omega \cdot m)^{-1}$, for the [11-20] direction is $\theta_{SH} = 0.128$ and $\sigma_S = 1615 (\hbar/e)(\Omega \cdot m)^{-1}$ (figure 40 (c) and (d)), which are much lower compared with the value for the non-inserting stack, as expected from the inserting stack. However, the θ_{SH} in the inserting stack is still much larger than the $\theta_{SH} = 0.05$ in the Pt/Py reference

sample. Moreover, the anisotropic behavior of α , θ_{SH} and σ_{S} are severely suppressed which is due to the almost vanishing exchange bias at the interface thanks to the Cu inserting layer.

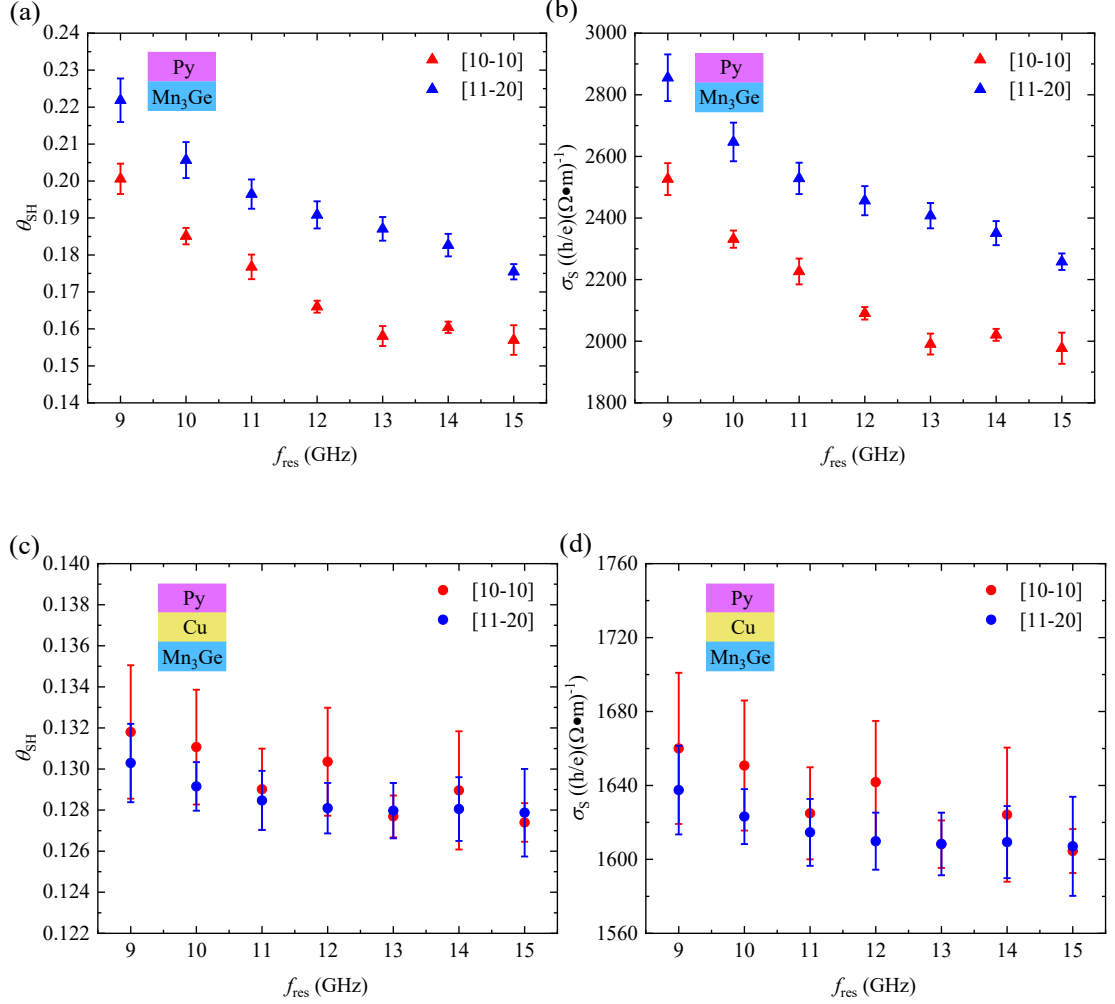


Figure 40: (a) SHA value and (b) SHC value versus the resonance frequency determined from the ST-FMR spectra of Mn₃Ge/Py stack along [10-10] and [11-20] directions. (c) SHA value and (d) SHC value versus the resonance frequency determined from the ST-FMR spectra of Mn₃Ge/Cu/Py stack along [10-10] and [11-20] directions.

We can also estimate the interface spin pumping efficiency by calculating the spin-mixing conductance $g_{\text{r}}^{\uparrow\downarrow}$ of the stack^[22, 47]. By keeping the 50 nm thickness of the Mn₃Ge layer and depositing stack with different thicknesses t of Py layer ($t = 5, 6, 7, 8,$

9, 10 nm), we can determine the $g_r^{\uparrow\downarrow}$ of the Mn₃Ge/Py and Mn₃Ge/Cu/Py interface to be 237 nm⁻² and 13.7 nm⁻². For comparison, $g_r^{\uparrow\downarrow} = 15.2$ nm⁻² for the Pt/Py reference stack. The higher spin-mixing conductivity at the Mn₃Ge/Py interface is consistent with the large SHC calculated from the ST-FMR spectra. The Cu inserting layer effectively reduces the $g_r^{\uparrow\downarrow}$ in the Mn₃Ge/Cu/Py interface, which coincides with the lower SHC of the stack. Even the value of $g_r^{\uparrow\downarrow}$ of Mn₃Ge/Cu/Py and Pt/Py interface are very close, the SHA of the former stack is still much higher than the latter as the Mn₃Ge film has much smaller longitudinal conductivity ($\sigma_{\text{Mn}_3\text{Ge}} = 3037$ (ohm • cm)⁻¹ and $\sigma_{\text{Pt}} = 23821$ (ohm • cm)⁻¹).

In summary, we have prepared high-quality hexagonal Mn₃Ge (0001) film by MBE for the first time reported so far. We have observed a significant spin Hall effect in the D0₁₉ Mn₃Ge thin film by ST-FMR technique as predicted by theoretical calculation and investigated the interface contribution of the AF/FM stack which is essential for the application of the AF spintronics.

5 Electrical manipulation of Mn₃Ge/Pt bilayer stack

5.1 Sample preparation

Ferromagnetic related study has already established that the SOT switching of the perpendicular magnetization is beneficial in spintronic device applications. Also, the full switching of the stack is important to maintain its reliable operation. These have been widely studied already. Meanwhile, in recent years AF spintronics has attracted attention as the antiferromagnets are insensitive to the external field and the terahertz dynamics of antiferromagnets may lead to higher storage density and ultrafast spintronics devices^[44, 45, 51]. One way to achieve the AF switching is to use the same protocol as the ferromagnetic device. To use the same protocol for the perpendicular full switching, there are two requirements for antiferromagnets. First, it needs to break the time-reversal symmetry (TRS) macroscopically. Second, the AF state must show perpendicular magnetic anisotropy. For the Mn₃X(X=Sn, Ge) family, the in-plane chiral AF spin texture can be seen as the ferroic order of a cluster magnetic octupole, and it also breaks TRS macroscopically^[52]. The AHE, ANE and MOKE properties of Mn₃X family lead to the possibility of large response detection of the change in the AF order. There have been reports from 2020 about switching research on Mn₃Sn^[45, 53, 54], however, the switching behavior of Mn₃Ge has yet to be reported so far. The main reason is for Mn₃Sn film, you can easily grow high-quality hexagonal Kagome (0001) and (10-10) phase film by sputtering

and MBE as it is easy to use two metal phase sources for growth, however as for Mn_3Ge , the high diffusion rate of Ge makes it challenging to control during deposition, thus only few published Mn_3Ge film papers can be seen so far, and many of their samples show polycrystalline behavior. It is challenging to grow single crystal $\text{Mn}_3\text{Ge}(0001)$ film, especially about (10-10) film similar to Mn_3Sn .

In my research, by using the offcut growth technology to prepare offcut $\text{Mn}_3\text{Ge}(0001)$ film with Pt on top, we successfully prepare the AF/HM stack for switching behavior detection. Using the same protocol as the ferromagnetic spintronics and Mn_3Sn research, we find the unusual switching behavior of Mn_3Ge offcut film.

The stack we use is $1.5\text{nm Ru}(0001)/t\text{ nm Mn}_3\text{Ge}(0001)/t'\text{ nm Pt}(111)$ with 6.5\AA Ru/10 nm MgO capping layer grown on offcut YSZ(111)K(211) 3° substrate. The growth condition of Ru, Mn_3Ge and capping layer is same as the AHE experiment, the Pt layer is prepared at 100°C without following annealing. Note that to prevent the Pt rod melting problem in EBE, the growth rate of Pt is set to be $800\text{s}/\text{\AA}$ so that the temperature of Pt rod won't get close to or exceed the melting point of Pt. For the thickness of Mn_3Ge layer, we tried 25 nm, 40 nm and 150 nm for comparison. For Pt thickness, we tried 4 nm, 5 nm, and 7 nm at the beginning then due to the high conductivity of Pt which may cause huge shunting, we decided to use 4 nm Pt as spin sink layer. All three options show good crystal quality of Mn_3Ge and Pt. From figure 41 (a), the Pt RHEED pattern shows single crystal steaks with stepped surfaces, similar to Ru and Mn_3Ge layer, this confirms the epitaxy growth mode of the stack. Figure 41 (b) shows the excellent crystal quality of Mn_3Ge and Pt films

from thin to thick.

After successfully prepare the sample, we can proceed to the sample lithography. We etched 4-foot hall bar on the sample with the size to be 10 μm width, 60 μm length and 5 μm hall bar feet width. Same 4-foot hall bar sample are used for switching measurement and AHE measurement so that we can compare the electrical switching efficiency.

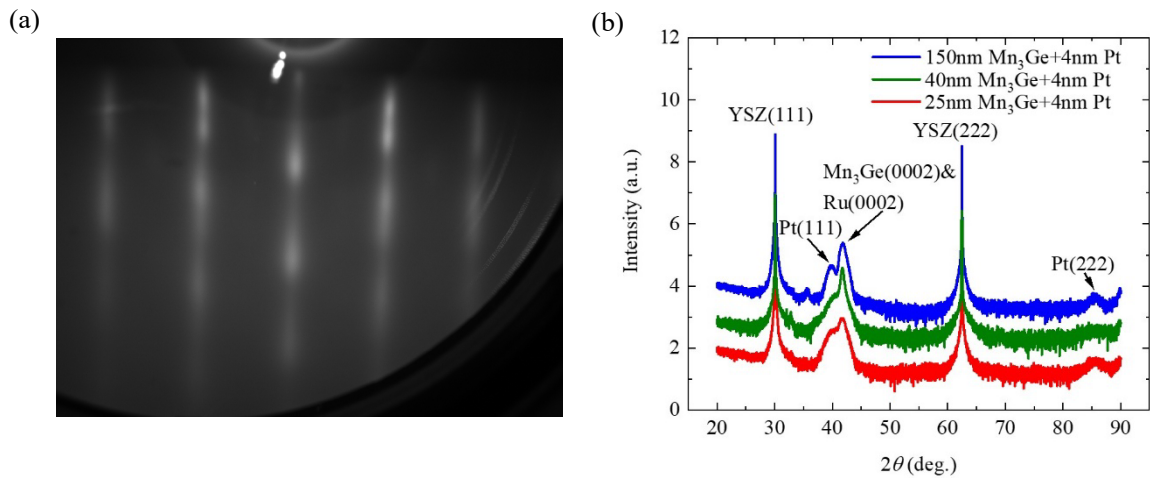


Figure 41: (a) The RHEED pattern of 4 nm Pt(111). (b) the XRD spectra of the switching sample with different Mn₃Ge thicknesses of 25 nm, 40 nm, and 150 nm.

5.2 Magnetic switching measurement

All the switching experiment has been carried out in the same PPMS Dynacool system as the AHE experiment. The investigation is carried out at 300K unless specified. We use OP and IP rotation puck for the measurement. As mentioned before, we use Keithley 2635B as DC input source and read-out meter. The thickness of Mn₃Ge layer is 40nm unless specified. Pt layer is 4nm thick.

The illustration of the measurement can be seen in figure 42 (a). The input voltage source injects current flow along the x direction which is along the length of the

hall bar. Then we measure the output voltage along y direction. The measurement sequence we use is illustrated in figure 42(b). First, we apply input voltage pulse for 100 ms, then wait for 700 ms to let the sample cool down so that the output signal will not be affected by the joule heating. In fact, after 700 ms waiting time, we apply the read current along the hall bar and measure the output transverse voltage signal. The read current is set to be 1mA according to the previous AHE measurement. The read current is large for the switching measurement because of the huge shunting effect of the device.

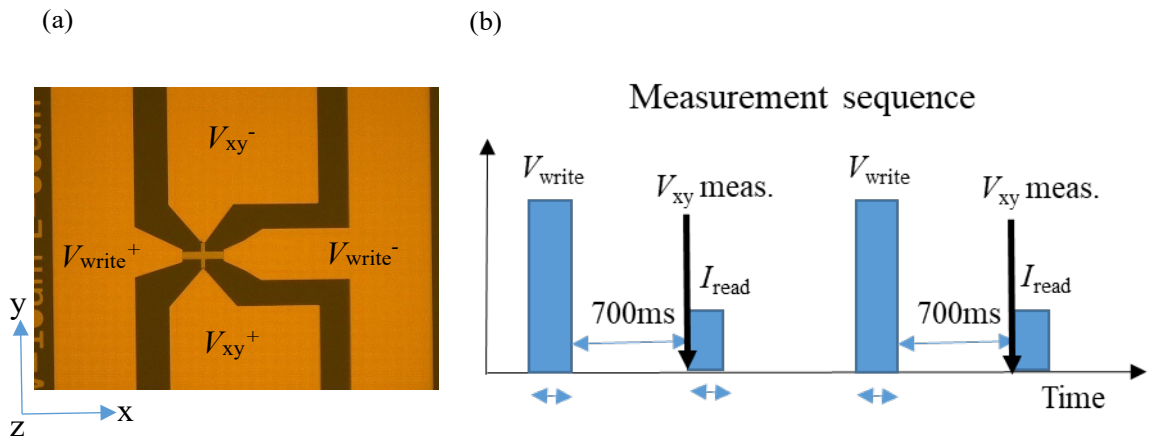


Figure 42: (a) Optical picture of the fabricated Hall bar devices. Input voltage is applied from left to right along the Hall bar which the x direction. V_{xy} is measured along y direction. (b) Measurement sequence of the experiment.

First, at 300K, we measure the input voltage versus the transverse output voltage with current flow along [10-10] and [11-20] direction of the Mn_3Ge in the absence of an external magnetic field, as shown in figure 43 (a). All the switching loops are plotted with two full switching loops. Apparent switching behavior can be observed in the absence of an external magnetic field. By slowly increasing the input voltage from 0V to 3.7V with the instep of 0.24V, the switching behavior shows up from

3.5V with the clockwise switching behavior when read current flow along [11-20] direction and anticlockwise for [10-10] direction. The magnitude reaches the maximum when the increased voltage reaches 3.7V for the size of the hall pattern we use. If we increase the voltage, there will be fluctuation in the device which will make the switching behavior unstable, and the device will burn out at around 3.75V for a couple of measurement loops. This fluctuation is predicted theoretically due to the chiral spin rotation^[53, 55-58]. At 3.7V, the device can stand for at least one thousand times of switching loop measurement without burning. The zero-field switching has been reported for MBE-prepared Mn₃Sn(10-10) film^[45], the author found the probabilistic switching behavior of the Mn₃Sn film without field and they conclude that the large-sized domain of the MBE-prepared film and PMA suppress the cancellation of the AHE in the Mn₃Sn film, and thus induce a clear zero-field switching which is not the SOT induced switching. However, in my Mn₃Ge film, it is different as shown in figure 43 (b). We insert a 6.5Å Cu layer between Pt and Mn₃Ge and use the same measurement parameters for the switching investigation. As the Cu is relatively thin, the shunting effect can be neglected so we use the same input power limit of 3.7V and read current 1mA for test. Notably, derived from the input voltage and the resistance of the hall bar device, the electrical switching current density is 14.55 MA/cm² in Mn₃Ge sample, which is comparable to the reported Mn₃Sn sample^[54, 55].

If the zero-field switching behavior originates from the large-sized domain and PMA of the Mn₃Ge layer which suppresses the cancellation of the AHE, then by inserting the Cu between the Mn₃Ge and Pt will not cancel or affect this mechanism, which means with Cu inserting, there will still be switching behavior in the sample,

contract to the results shown in figure 43 (b). This approves the interface of Pt and Mn_3Ge plays a vital role for the switching behavior.

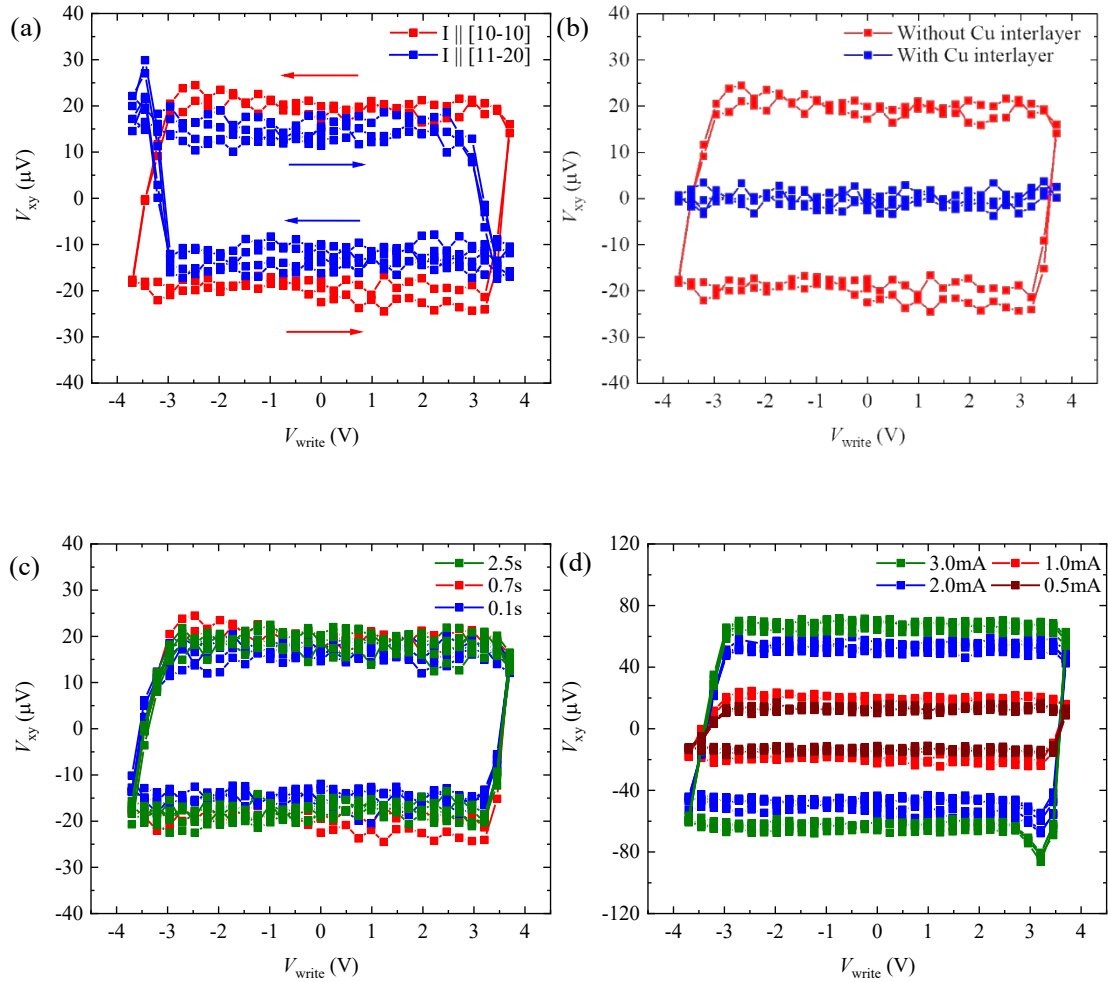


Figure 43: (a) Dependence of the transverse voltage V_{xy} on the input voltage V_{write} in the absence of external magnetic field along [10-10] and [11-20] of Mn_3Ge film. (b) transverse voltage V_{xy} versus input voltage V_{write} for $\text{Mn}_3\text{Ge}/\text{Pt}$ sample and $\text{Mn}_3\text{Ge}/\text{Cu}/\text{Pt}$ sample current flows along the [10-10] direction of the sample. Transverse voltage versus input voltage with read current flow along [10-10] direction in the absence of field with (c) different waiting time and (d) with different value.

After we find the switching behavior in the sample, we calibrate the waiting time and the read current. As shown in figure 43 (c), there is no obvious heating fluctuation in the stack in the time scale of ms which may affect the switching

behavior. But we still choose to use 0.7s waiting time for consistency. When calibrating the read current value, we tried the read current dependence of the switching experiment at 300K without field. We can see from figure 43 (d), with increasing current value, the magnitude of the switching loops increases to, but not a linear response. 0.5mA and 1mA measurement shows close magnitude while 2mA and 3mA measurement gives similar results. The positive correlation can be explained as with increasing read current, more current flows through the Mn₃Ge layer, thus increasing the magnitude of V_{xy} . This increment should be proportional to the read current value. However, more read current flowing through the stack will also induce larger vortex field which may suppress the magnitude of the switching as shown in field dependence measurement. Meanwhile, higher current generates more heat in the sample, thus affect the spin texture of the Mn₃Ge layer. Thus, 3mA read current may give rise to 1-time larger magnitude than 2mA current, but because of the existence of the vortex field, the increment in V_{xy} magnitude is suppressed. Same story for the 0.5mA and 1.0mA comparison situation. For 2 mA read current, the magnitude of V_{xy} is 2.2 times of it in 1mA situation which is different from 3mA-2mA and 1mA-0.5mA situation. I believe this is because when we increase the increase read current, the switching behavior originated from the read current is enhanced. The 1mA read current is equal to the read current density 0.84 MA/cm².

Moreover, we also apply field when measuring the switching behavior. We set the input voltage along the [10-10] direction, then set the field in the same direction as the input voltage as shown in figure 44 (a). With increasing field from 0T to 9T, the switching of the stack is suppressed with smaller magnitude of V_{xy} . The external

field aligns the Mn₃Ge domains after switching to reduce the change in V_{xy} magnitude. IP field induces unneglectable ordinary Hall effect in stack during switching which suppress the alignment by increasing the spin current in the stack as field and current may not be fully parallel. With OP field, the switching behavior shows similar results. This indicates that the switching in the sample is relatively insensitive to the external magnetic field even up to 9T.

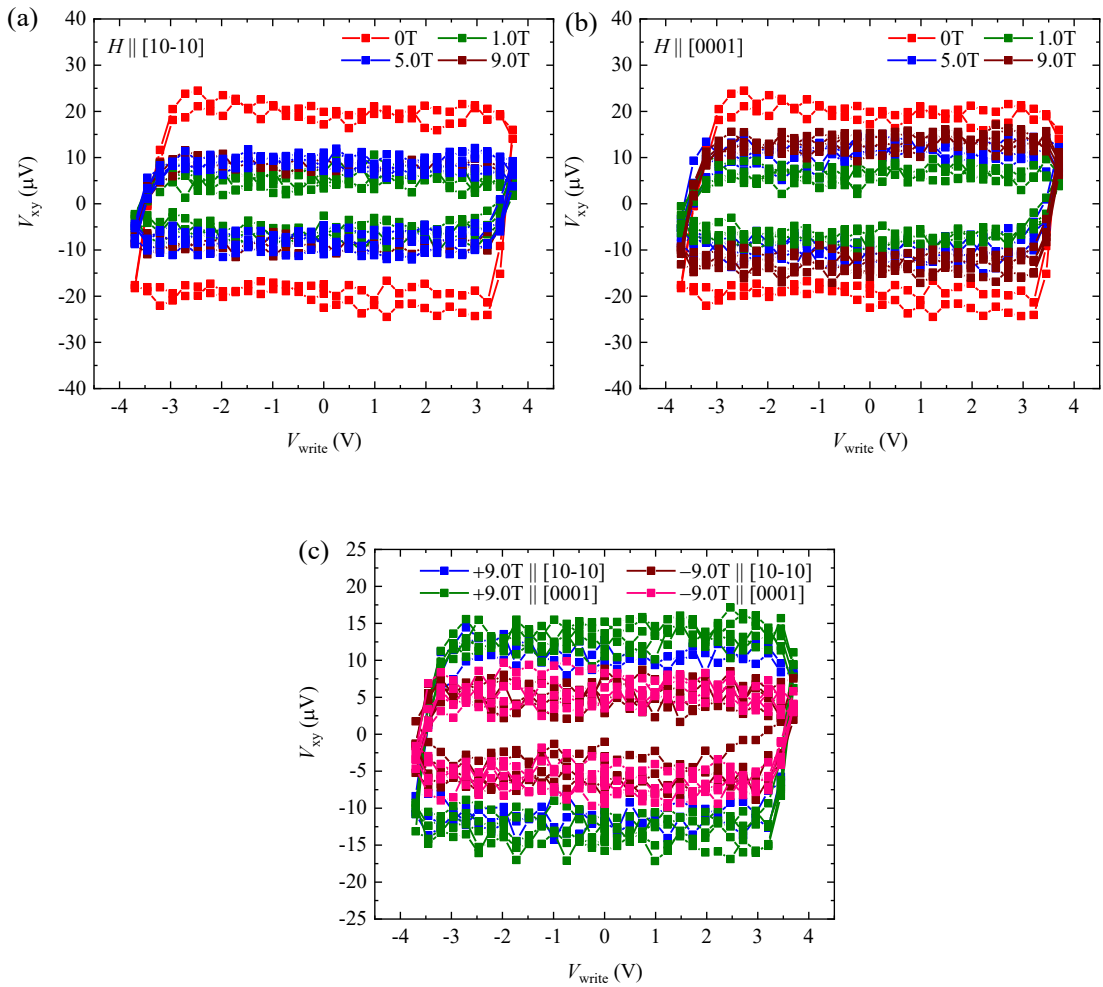


Figure 44: Transverse voltage as the function of input voltage with read current flow along [10-10] direction, field along (a) [10-10] in-plane direction, (b) out-of-plane [0001] direction, (c) with field in different polarity.

By comparing the switching loops with different field polarity along in-plane [10-10] direction and out-of-plane [0001] direction, we can see that the magnitude of transverse voltage is larger with positive field in figure 44 (c). This is because the field helps align the domains in the Mn₃Ge layer and it has favorable direction. It also induces ordinary Hall effect in the stack and enhances the switching behavior by increasing the spin current. These ensures that at 9T, the sample still shows switching behavior. The Hall voltage changes sign with opposite field direction thus the relevant spin current too, but the spin seed layer defined by the interface DMI remains the same with current flow on the same direction. That's why V_{xy} has different magnitude with field in opposite direction.

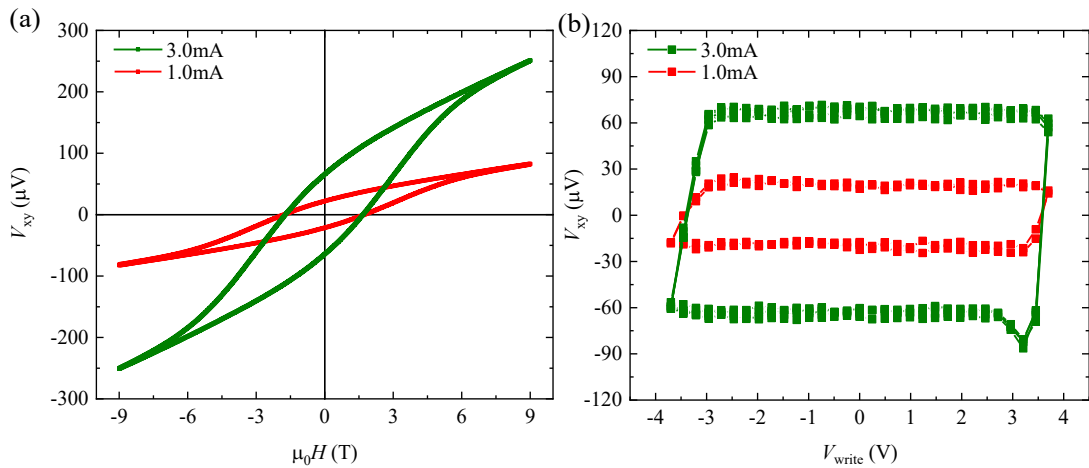


Figure 45: (a) AHE measurement on 4-foot switching hall bar with 1mA and 3mA read current and out-of-plane field. (b) switching measurement with 1mA and 3mA read current in the absence of field.

By using the same hall bar, we carry out the AHE measurement and switching measurements with the same read current 1mA and 3mA. In the AHE loop as shown in figure 45 (a), with increasing read current the whole stack shows larger zero field transverse voltage which the contribution of the Mn₃Ge layer. The larger

Magnitude with 3mA input current should also come from the chiral spin texture contribution of Mn₃Ge layer. As we discussed before, it is not from the contribution of the large domain size of the Mn₃Ge layer. By comparing the ratio of $\Delta V_{xy}^{\text{current}}/\Delta V_{xy}^{\text{field}}$, the volume fraction of the electrically controllable switching can be 100% for 1mA read current and 93% for 3mA read current.

To further investigate the full switching behavior of the sample, we use 25 nm Mn₃Ge/ 4 nm Pt and 150 nm Mn₃Ge/4 nm Pt stacks to carry the same ratio experiment. We use different Mn₃Ge and Pt thicknesses from previous experiments for diversity. As the thickness changes, the input voltage limit also changes for switching measurement, but we keep the critical current density unchanged for the thickness dependence measurement. The read current is set to be 1mA. In figure 46 (a), with thin Mn₃Ge, the shunting effect of Pt is too strong that AHE won't give obvious AHE signal, but for switching experiment, it shows obvious and stable deterministic switching of 10 loops. This approves the high sensitivity of the switching signal and the advantage of electrical manipulation of the AF domain in Mn₃Ge film over the conventional field manipulation. For 150 nm Mn₃Ge/4 nm Pt stack, the ratio of $\Delta V_{xy}^{\text{current}}/\Delta V_{xy}^{\text{field}}$ is calculated to be 26%. The low volume value is due to the thick Mn₃Ge layer. The interface-driven electrical switching can not manipulate the whole thick Mn₃Ge layer, instead, it leaves many layers of Mn₃Ge spin texture unchanged during switching, so the magnitude of the electrical switching is smaller than expected full stack switching. But for the AHE effect, the field can easily manipulate the full stack and the thick Mn₃Ge enables enough read current flowing through the AHE layer to carry the AHE signal.

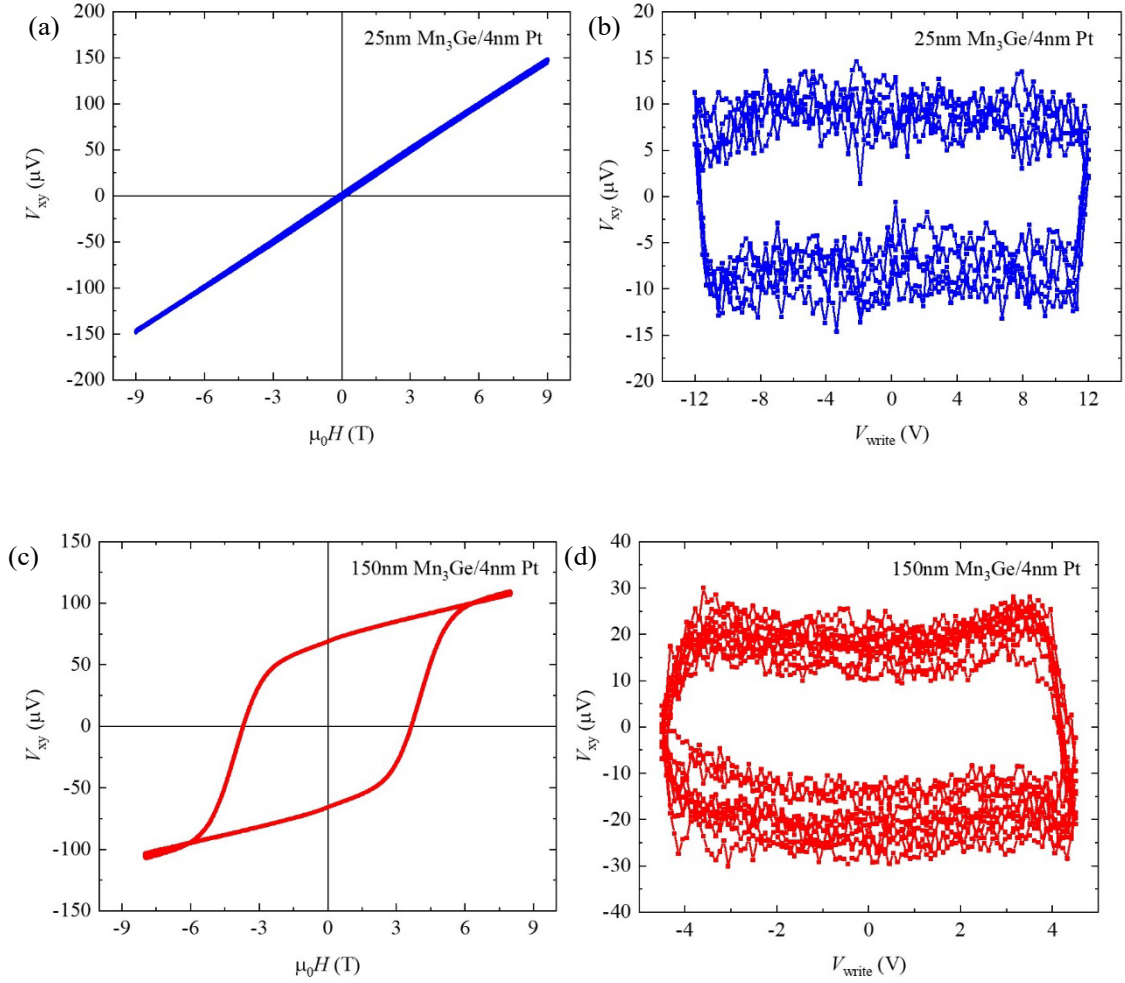


Figure 46: (a)AHE measurement and (b) switching measurement of 25nm Mn₃Ge/ 4nm Pt stack. (c)AHE measurement and (d) switching measurement of 150nm Mn₃Ge/ 4nm Pt stack.

5.3 The origin of the switching mechanism

Next, we are going to discuss the switching experiment and try to analyze the origin of the field-free full switching behavior in the offcut Mn₃Ge sample.

Recently, there are papers published about field-free SOT switching of the wedge FM/HM stack^[59], gated FM/HM stack^[60], SAF stack^[61, 62] and Mn₃Sn/HM stack^[45, 53, 54]. From the experiment introduced above, the interface plays a vital role in the switching. By reviewing the literature, we combine the points of the above papers

and try to explain the mechanism in our research.

First, we believe the switching comes from the interface rather than bulk contribution. The offcut Mn_3Ge film naturally breaks TRS and the inversion symmetry breaks at the interface. The interface DMI effect not only generates SOT switching behavior but also ensures there is no need to use the external field to break the symmetry like in the FM/HM system and $\text{Mn}_3\text{Sn}/\text{HM}$ system. This helps to achieve the field-free switching of the $\text{Mn}_3\text{Ge}/\text{Pt}$ stack. Moreover, short spin-diffusion lengths should limit the thickness of switchable Mn_3Ge layers (usually a few nanometers), while the newly proposed Seeded SOT mechanism^[54] could explain the odd condition. When writing the stack with DC voltage, the SOT from the spin current can only manipulate a few atomic layers of the adjacent Mn_3Ge film. Meanwhile, the power heats the stack for Mn_3Ge to overcome the AF ordering temperature which is expected to be more than 400K in approximately 100ns derived from the experiment on Mn_3Sn stack^[54], the domains which is large in MBE prepared Mn_3Ge are randomized. At the same time, a thin layer of Mn_3Ge will be switched when the current density is high enough. When the sample is cooled down below the ordering temperature in around 10 to 20ns analogical to Mn_3Sn [7] after the injection of the DC write voltage, this layer which can be treated as the seed SOT layer will seed the domain configuration of the whole stack of the AF layer. When the waiting time is 700ms, it is long enough for the sample to cool down thoroughly below the transition temperature. Then with read current flowing through the stack, we can probe the spin rotation of the entire stack. However, when the Mn_3Ge layer is way too thick, say 150nm, the Seed layer generated by the SOT from Pt layer, still fail to switch the whole 150nm stack as thicker film has more

defects which freeze the domains to be switched. From the ratio of the electrical switching magnitude over the field switching magnitude, we can estimate that only 40nm of Mn₃Ge can be switched by the interface-generated SOT. Notably, the temperature caused by injection voltage heating can not be directly measured as the sample could burn out under a long time of injection, and the device can only be safe when the current flow is lower than 4mA for long time measurement.

In summary, the robust interface DMI effect induced SOT is generated at the offset Mn₃Ge/Pt interface, the TRS broken nature of Mn₃Ge ensures the switching can happen in the absence of the external magnetic field. The Seed SOT mechanism ensures that the maximum 40nm thick Mn₃Ge film can be manipulated during the measurement under the current measurement setting.

The experiment shows the advantage of AF spintronics. The Mn₃Ge/Pt switching stack is insensitive to the external field which will ensure the safety of the stored information under complex magnetic conditions. The switching can happen without the existence of an assistance field like FM-based devices which is convenient for data writing and reading. The stack could also be thicker than many ferromagnetic-based devices to have more thermal stability. The full switching behavior and low critical current density of Mn₃Ge ensure the efficiency and energy saving of future applications.



6 Conclusion and outlook

In this thesis, I investigate the fundamental property and potential application of Mn_3Ge film. I have successfully prepared high-quality single crystal hexagonal Mn_3Ge film by MBE for the first time reported. I have investigated the SHE of the Mn_3Ge film by ST-FMR technology to confirm the large spin hall angle of Mn_3Ge . By applying the offcut growth technology, offcut Mn_3Ge film is used for the determination of AHE. By adding Pt layer on Mn_3Ge film, I find the electrical switching behavior of the offcut stack which has yet to be reported so far for Mn_3Ge . The field-free full switching efficiency and high reliability of Mn_3Ge -based devices are promising for future application in AF spintronic industry.

Until now, most of the papers published regarding experimental research of the Mn_3X ($\text{X}=\text{Ge}, \text{Sn}$) family are about Mn_3Sn ^[45, 54-56, 63, 64]. This thesis fills the gap and proves the potential of Mn_3Ge in AF spintronics, for instance, to be used in the AF MTJ^[65].



Bibliography

- [1] Ando, Y. *Journal of the Physical Society of Japan* **2013**, 82, (10), 102001.
- [2] Hasan, M. Z.; Kane, C. L. *Reviews of Modern Physics* **2010**, 82, (4), 3045-3067.
- [3] Wan, X.; Turner, A. M.; Vishwanath, A.; Savrasov, S. Y. *Physical Review B* **2011**, 83, (20).
- [4] Manna, K.; Sun, Y.; Muechler, L.; Kübler, J.; Felser, C. *Nature Reviews Materials* **2018**, 3, (8), 244-256.
- [5] Wehling, T. O.; Black-Schaffer, A. M.; Balatsky, A. V. *Advances in Physics* **2014**, 63, (1), 1-76.
- [6] Yan, B.; Felser, C. *Annual Review of Condensed Matter Physics* **2017**, 8, (1), 337-354.
- [7] Yang, H.; Sun, Y.; Zhang, Y.; Shi, W.-J.; Parkin, S. S. P.; Yan, B. *New Journal of Physics* **2017**, 19, (1), 015008.
- [8] Zhang, Y.; Železný, J.; Sun, Y.; van den Brink, J.; Yan, B. *New Journal of Physics* **2018**, 20, (7), 073028.
- [9] Zhang, Y.; Sun, Y.; Yang, H.; Železný, J.; Parkin, S. P. P.; Felser, C.; Yan, B. *Physical Review B* **2017**, 95, (7).
- [10] Yang, K.-Y.; Lu, Y.-M.; Ran, Y. *Physical Review B* **2011**, 84, (7), 075129.
- [11] Grushin, A. G. *Physical Review D* **2012**, 86, (4), 045001.
- [12] Burkov, A. A.; Balents, L. *Physical Review Letters* **2011**, 107, (12), 127205.
- [13] Xu, G.; Weng, H.; Wang, Z.; Dai, X.; Fang, Z. *Physical Review Letters* **2011**, 107, (18), 186806.
- [14] Shekhar, C.; Kumar, N.; Grinenko, V.; Singh, S.; Sarkar, R.; Luetkens, H.; Wu, S.-C.; Zhang, Y.; Komarek, A. C.; Kampert, E.; Skourski, Y.; Wosnitza, J.; Schnelle, W.; McCollam, A.; Zeitler, U.; Kübler, J.; Yan, B.; Klauss, H. H.; Parkin, S. S. P.; Felser, C. *Proceedings of the National Academy of Sciences* **2018**, 115, (37), 9140-9144.
- [15] Sun, Y.; Wu, S.-C.; Ali, M. N.; Felser, C.; Yan, B. *Physical Review B*

-
- 2015**, 92, (16), 161107.
- [16] Soluyanov, A. A.; Gresch, D.; Wang, Z.; Wu, Q.; Troyer, M.; Dai, X.; Bernevig, B. A. *Nature* **2015**, 527, (7579), 495-498.
- [17] Nakatsuji, S.; Kiyohara, N.; Higo, T. *Nature* **2015**, 527, (7577), 212-215.
- [18] Nayak, A. K.; Fischer, J. E.; Sun, Y.; Yan, B.; Karel, J.; Komarek, A. C.; Shekhar, C.; Kumar, N.; Schnelle, W.; Kübler, J.; Felser, C.; Parkin, S. S. P. *Science Advances* **2016**, 2, (4), e1501870.
- [19] Zhang, D.; Yan, B.; Wu, S.-C.; Kübler, J.; Kreiner, G.; Parkin, S. S.; Felser, C. *Journal of Physics: Condensed Matter* **2013**, 25, (20), 206006.
- [20] Qian, J. F.; Nayak, A. K.; Kreiner, G.; Schnelle, W.; Felser, C. *Journal of Physics D: Applied Physics* **2014**, 47, (30), 305001.
- [21] Zhang, D.; Yan, B.; Wu, S. C.; Kubler, J.; Kreiner, G.; Parkin, S. S.; Felser, C. *J Phys Condens Matter* **2013**, 25, (20), 206006.
- [22] Hong, D.; Anand, N.; Liu, C.; Liu, H.; Arslan, I.; Pearson, J. E.; Bhattacharya, A.; Jiang, J. *Physical Review Materials* **2020**, 4, (9), 094201.
- [23] Cho, A. Y.; Arthur, J. R. *Progress in Solid State Chemistry* **1975**, 10, 157-191.
- [24] Sharma, P.; Tripathi, N.; Gupta, N. *Journal of Materials Science: Materials in Electronics* **2016**, 28, (4), 3891-3896.
- [25] Joyce, B. A. *Reports on Progress in Physics* **1985**, 48, (12), 1637.
- [26] Arthur, J. R. *Surface Science* **2002**, 500, (1), 189-217.
- [27] Joyce, B. A. *Contemporary Physics* **1990**, 31, (3), 195-197.
- [28] Nunn, W.; Truttmann, T. K.; Jalan, B. *Journal of Materials Research* **2021**, 36, (23), 4846-4864.
- [29] Braun, W., *Applied RHEED: reflection high-energy electron diffraction during crystal growth*. Springer Science & Business Media: 1999; Vol. 154.
- [30] Hasegawa, S. *Characterization of Materials* **2012**, 97, 1925-1938.
- [31] Ichimiya, A.; Cohen, P. I.; Cohen, P. I., *Reflection high-energy electron diffraction*. Cambridge University Press: 2004.

-
- [32] Stevie, F. A.; Donley, C. L. *Journal of Vacuum Science & Technology A* **2020**, 38, (6), 063204.
- [33] Benes, E. *Journal of Applied Physics* **1984**, 56, (3), 608-626.
- [34] Khan, H.; Yerramilli, A. S.; D'Oliveira, A.; Alford, T. L.; Boffito, D. C.; Patience, G. S. *The Canadian Journal of Chemical Engineering* **2020**, 98, (6), 1255-1266.
- [35] Perrière, J. *Vacuum* **1987**, 37, (5), 429-432.
- [36] Chu, W. K.; Liu, J. R. *Materials Chemistry and Physics* **1996**, 46, (2), 183-188.
- [37] Giessibl, F. J. *Reviews of modern physics* **2003**, 75, (3), 949.
- [38] Tersoff, J.; Hamann, D. R. *Physical review letters* **1983**, 50, (25), 1998.
- [39] Tersoff, J.; Hamann, D. R. *Physical Review B* **1985**, 31, (2), 805.
- [40] *Physical Property Measurement System-DynaCool User's Manual 14th edition*. Quantum Design, San Diego: 2014.
- [41] *Magnetic Property Measurement System-SQUID VSM User's Manual 13th edition*. Quantum Design, San Diego: 2013.
- [42] Wang, Y.; Ramaswamy, R.; Yang, H. *Journal of Physics D: Applied Physics* **2018**, 51, (27), 273002.
- [43] Liu, L.; Moriyama, T.; Ralph, D.; Buhrman, R. *Physical review letters* **2011**, 106, (3), 036601.
- [44] Baltz, V.; Manchon, A.; Tsoi, M.; Moriyama, T.; Ono, T.; Tserkovnyak, Y. *Reviews of Modern Physics* **2018**, 90, (1), 015005.
- [45] Higo, T.; Kondou, K.; Nomoto, T.; Shiga, M.; Sakamoto, S.; Chen, X.; Nishio-Hamane, D.; Arita, R.; Otani, Y.; Miwa, S.; Nakatsuji, S. *Nature* **2022**, 607, (7919), 474-479.
- [46] Xiang, Y.; Guo, F. W.; Lu, T. M.; Wang, G. C. *Nanotechnology* **2016**, 27, (48), 485703.
- [47] Zhang, W.; Han, W.; Jiang, X.; Yang, S.-H.; S. P. Parkin, S. *Nature Physics* **2015**, 11, (6), 496-502.
- [48] Zhang, W.; Han, W.; Yang, S.-H.; Sun, Y.; Zhang, Y.; Yan, B.; Parkin, S. S. P. *Science Advances* **2016**, 2, (9), e1600759.

-
- [49] Zhou, J. A.-O.; Wang, X.; Liu, Y. A.-O.; Yu, J.; Fu, H.; Liu, L.; Chen, S.; Deng, J.; Lin, W.; Shu, X.; Yoong, H. Y.; Hong, T. A.-O.; Matsuda, M. A.-O.; Yang, P.; Adams, S. A.-O. X.; Yan, B. A.-O.; Han, X.; Chen, J. A.-O. *Science Advance* **2019**, 5, (2375-2548 (Electronic)), eaau669.
- [50] Tsai, H.; Higo, T.; Kondou, K.; Kobayashi, A.; Nakano, T.; Yakushiji, K.; Miwa, S.; Otani, Y.; Nakatsuji, S. *AIP Advances* **2021**, 11, (4), 045110.
- [51] Jungwirth, T.; Marti, X.; Wadley, P.; Wunderlich, J. *Nature Nanotechnology* **2016**, 11, (3), 231-241.
- [52] Suzuki, M. T.; Koretsune, T.; Ochi, M.; Arita, R. *Physical Review B* **2017**, 95, (9), 094406.
- [53] Tsai, H.; Higo, T.; Kondou, K.; Nomoto, T.; Sakai, A.; Kobayashi, A.; Nakano, T.; Yakushiji, K.; Arita, R.; Miwa, S. *Nature* **2020**, 580, (7805), 608-613.
- [54] Pal, B.; Hazra, B. K.; Göbel, B.; Jeon, J.-C.; Pandeya, A. K.; Chakraborty, A.; Busch, O.; Srivastava, A. K.; Deniz, H.; Taylor, J. M.; Meyerheim, H.; Mertig, I.; Yang, S.-H.; Parkin, S. S. P. *Science Advances* **2022**, 8, (24), eabo5930.
- [55] Takeuchi, Y.; Yamane, Y.; Yoon, J.-Y.; Itoh, R.; Jinnai, B.; Kanai, S.; Ieda, J. i.; Fukami, S.; Ohno, H. *Nature Materials* **2021**, 20, (10), 1364-1370.
- [56] Fujita, H. *physica status solidi (RRL) – Rapid Research Letters* **2017**, 11, (4), 1600360.
- [57] Nomoto, T.; Arita, R. *Physical Review Research* **2020**, 2, (1), 012045.
- [58] Gomonay, O. V.; Loktev, V. M. *Low Temperature Physics* **2015**, 41, (9), 698-704.
- [59] Chen, S.; Yu, J.; Xie, Q.; Zhang, X.; Lin, W.; Liu, L.; Zhou, J.; Shu, X.; Guo, R.; Zhang, Z.; Chen, J. *ACS Applied Materials & Interfaces* **2019**, 11, (33), 30446-30452.
- [60] Kang, M.-G.; Choi, J.-G.; Jeong, J.; Park, J. Y.; Park, H.-J.; Kim, T.; Lee, T.; Kim, K.-J.; Kim, K.-W.; Oh, J. H.; Viet, D. D.; Jeong, J.-R.; Yuk, J. M.; Park, J.; Lee, K.-J.; Park, B.-G. *Nature Communications* **2021**, 12, (1), 7111.
- [61] Chen, R.; Cui, Q.; Liao, L.; Zhu, Y.; Zhang, R.; Bai, H.; Zhou, Y.; Xing, G.; Pan, F.; Yang, H.; Song, C. *Nature Communications* **2021**, 12, (1), 3113.

-
- [62] He, W.; Wan, C.; Zheng, C.; Wang, Y.; Wang, X.; Ma, T.; Wang, Y.; Guo, C.; Luo, X.; Steblyy, M. E.; Yu, G.; Liu, Y.; Ognev, A. V.; Samardak, A. S.; Han, X. *Nano Letters* **2022**, 22, (17), 6857-6865.
- [63] Taylor, J. M.; Markou, A.; Lesne, E.; Sivakumar, P. K.; Luo, C.; Radu, F.; Werner, P.; Felser, C.; Parkin, S. S. P. *Physical Review B* **2020**, 101, (9), 094404.
- [64] Higo, T.; Qu, D.; Li, Y.; Chien, C. L.; Otani, Y.; Nakatsuji, S. *Applied Physics Letters* **2018**, 113, (20), 202402.
- [65] Chen, X.; Higo, T.; Tanaka, K.; Nomoto, T.; Tsai, H.; Idzuchi, H.; Shiga, M.; Sakamoto, S.; Ando, R.; Kosaki, H.; Matsuo, T.; Nishio-Hamane, D.; Arita, R.; Miwa, S.; Nakatsuji, S. *Nature* **2023**, 613, (7944), 490-495.



List of Figures

- 1 (a) basic structure of half Heusler alloy (XYZ) and full Heusler alloy(X_2YZ). X(red spheres) and Y(blue spheres) are transition metals, with X being more electropositive than Y, and Z(green spheres) is a main group element. Full Heusler alloy could be one of the two types: regular Heusler and inverse alloy. (b) Illustration of the structure deformation from general cubic structure, by compression or elongation either along the [100] axis of cubic structure to tetragonal lattice with $I4/mmm$ space group, or along the [111] axis to a hexagonal structure with the $P6_3mc$ space group. (c) Due to the large magnetocrystalline anisotropy in tetragonal Heuslers, the preferred magnetization orientation can either be in-plane or out-of-plane by the sign of the magnetocrystalline anisotropy energy. The light blue spheres represent a 3d, 4d or 5d element that is introduced to alter the strength of the magnetocrystalline anisotropy. (d) for certain value of the anisotropy energy, the spin can form in a non-collinear order. Adapted from reference^[4]
- 2 Illustration of phase transition from cubic to tetragonal structure. Adapted from literature^[21].
- 3 (a) Illustration of phase transition from tetragonal to hexagonal structure. (b)-(f) The projection from the cubic-to-hexagonal structures. Adapted from literature^[1, 21].
- 4 (a) Crystal structure showing the two layers of Mn-Ge atoms stacked along the c(z) axis. (b) Calculated 120° antiferromagnetic configuration in the $z = 0$ and $z = c/2$ planes, respectively. The green dashed line indicates the mirror plane (that is, the xz plane). (c) First Brillouin zone and momentum-dependent AHC. (d) Illustration of the rotation of the triangular spin structure with an IP field. Adapted from literature^[18].
- 5 (A to F) Hall resistivity and Hall conductivity as a function of magnetic field measured at four representative temperatures for three different current and magnetic field configurations. Adapted from literature^[18].
- 6 Schematic of a typical electron beam evaporator and K-cell evaporator. From literature^[24].
- 7 Schematic of the various common methods of delivering metal sources in oxide MBE. Adapted from literature^[28].
- 8 The picture of the Quince MBE system.

-
- 9 Schematic diagram of RHEED apparatus. Adapted from literature^[30].
 - 10 Real space and reciprocal space of RHEED. Adapted from literature^[30].
 - 11 Schematic diagrams show the major components of an XPS instrument. Adapted from literature^[32].
 - 12 Illustration of the cryostat control system of the PPMS. Adapted from the literature^[40].
 - 13 SQUID signal detection schematic. Adapted from the literature^[41].
 - 14 (a) Illustration of the spin current generation in Pt/Py system in ST-FMR measurements. Blue arrow denotes the electron flow direction (opposite to the I_{rf} direction). The arrows with green and red balls denote the generated spin polarizations in the Pt layer. (b) A typical ST-FMR signal from a Pt (6 nm)/Py (4 nm) device at 6 GHz. The blue and green curves represent the symmetric Lorentzian ($V_s F_s$) and antisymmetric Lorentzian ($V_A F_A$) components. Adapted from literature^[42].
 - 15 The FMR linewidth and Gilbert damping coefficient α as a function of the DC current, I_{dc} , in the Pt (6 nm)/Py (4 nm) bilayer device at $f = 8$ GHz. Adapted from literature^[43].
 - 16 (a) Physical grounded MgO(111) before annealing. (b) physical grounded MgO(111) after cleaning and annealing test. (c) chemical etched MgO(111) substrate before annealing. (d) chemical etched MgO(111) after cleaning and annealing treatment.
 - 17 The RHEED picture of Mn₃Ge film directly on (a) graphene and (c) LAO and with Ru buffer on (c) graphene and (d) LAO.
 - 18 RHEED pattern of Mn₃Ge(0001) grown (a) directly on YSZ(111) substrate and (b) with Ru buffer layer.
 - 19 AFM of perfect cut YSZ(111) substrate (a) before annealing and (b) after annealing.
 - 20 XRD measurement of the rocking curve of perfect cut YSZ(111) peak.
 - 21 The RHEED pattern of perfect cut YSZ(111) substrate along d (a) YSZ[11-2] and (b) YSZ[10-1] direction.
 - 22 (a) The AFM of annealed 3° offcut YSZ(111) substrate. (b) RHEED pattern of the same piece of substrate.

-
- 23 RHEED pattern of 5 nm Ru(0001) film deposited at 600°C on perfect YSZ(111) substrate, along (a) [10-10] and (b)[11-20] azimuthal direction.
 - 24 *In-situ* XPS spectra of 5 nm Ru(0001) film by the XPS in Quince system.
 - 25 RHEED streaks of Ru(0001) film deposited on YSZ(111) perfect cut substrate. All pictures are taken along the YSZ(111) [10-1] direction. (a) YSZ substrate. (b) 1 UC, (c) 2 UC, (d)4 UC, (e) 8 UC and (f) 12 UC thick Ru(0001) film.
 - 26 (a) XRD peak of Ru(0001) film on perfect cut substrate.(b) RHEED of 5 nm Ru film deposited on YSZ(111) 3° offcut substrate.
 - 27 (a) RHEED, (b) AFM and (c) *in-situ* XPS of 10 nm MgO capping on Mn₃Ge sample.
 - 28 XPS spectra of (a) Ge-2p peak and (b) Mn-2p peak. (c) RBS data of the Mn₃Ge/Ru stack. (d) Mn₃Ge RHEED pattern measurement along the Ru(0001) [11-20] direction.(e) Mn₃Ge RHEED pattern measurement along the Ru(0001) [10-10] direction.
 - 29 (a) XRD 2theta-omega scan spectra of 25 nm Mn₃Ge/5 nm Ru sample with MgO capping. (b) the 41.9139° XRD mix peak with fitted subpeaks of Mn₃Ge(0006) and Ru(0006). (c) STM scan of 50 nm Mn₃Ge/5 nm Ru stack. (d) height of one layer thickness of Mn₃Ge sample chosen from the figure (c).
 - 30 RHEED measured along the Ru(0001) [11-20] direction. (a) Ru film, (b) 2 nm, (c) 5 nm, (d) 25 nm, (e) 40 nm (f) 50 nm Mn₃Ge(0001).
 - 31 RHEED of Mn₃Ge(0001) grown on YSZ offcut substrate, measured along (a) [10-10] and (b) [11-20] direction. (c) STM of 50 nm Mn₃Ge/5 nm Ru sample. (d) XRD of Mn₃Ge sample with different thicknesses from 10 nm, 25 nm and 50 nm.
 - 32 (a) 6-feet hall bar device with 10μm width and 40μm length. (b) 4-feet hall bar width 10μm width and length 60μm length.
 - 33 (a) One design of the ST-FMR device C4 with 75 μm length and 15 μm width. (b) Size of different ST-FMR patterns. L means length and W means width. The values shown are in μm units.
 - 34 RHEED pattern of Mn₃Ge films grown on (a) YSZ(110) and (b) MgO(110) substrates.
 - 35 AHE measurement data. Transverse conductivity as a function of out-of-plane external magnetic field with current (a) along different in-plane directions at

-
- 300K, (b) along [10-10] direction at 5K, 100K, 200K, 300K, (c) along [11-20] direction at 5K, 100K, 200K, 300K. (d) longitudinal resistivity versus external magnetic field of the Mn₃Ge film at 300K with current along [11-20]. (e) comparison of the V_{xy} versus field loop of Mn₃Ge films grown on offcut YSZ(111) substrate and perfect cut YSZ(111) substrate with the sample stack thickness of 50 nm.
- 36 Field dependence of magnetization measured at (a) 5K and (b) 300K along three different directions.
- 37 9T field cooling and zero field cooling measurement of 500 nm offcut Mn₃Ge film along [10-10] direction.
- 38 (a) RHEED pattern of 50 nm Mn₃Ge (0001) film grown on 5 nm Ru buffer layer, along [11-20] and [10-10] direction. (b) XRD spectra of 10nm MgO capped 6 nm Py (111)/50 nm Mn₃Ge (0001)/5 nm Ru (0001) stack on YSZ (111) substrate. (c) STM topography of 50 nm Mn₃Ge (0001) film over 500×500 nm² area with the rms of 3.81 Å. (d) AFM image of the whole stack over 5×5 μm² area showing the rms of 3.6 Å.
- 39 ST-FMR spectra of a 6 nm Py (111)/ 50 nm Mn₃Ge (0001) sample along (a) [10-10] and (b) [11-20] directions. Insert: a device C4 for ST-FMR measurements with a length of 75 μm and a width of 15 μm. ST-FMR spectra of the structure 6 nm Py (111)/0.6 nm Cu (111)/50 nm Mn₃Ge (0001) along the (c) [10-10] and (d) [11-20] directions.
- 40 (a) SHA value and (b) SHC value versus the resonance frequency determined from the ST-FMR spectra of Mn₃Ge/Py stack along [10-10] direction. (c) SHA value and (d) SHC value versus the resonance frequency determined from the ST-FMR spectra of Mn₃Ge/Cu/Py stack along [10-10] direction.
- 41 (a) The RHEED pattern of 4 nm Pt(111). (b) the XRD spectra of the switching sample with different Mn₃Ge thicknesses of 25 nm, 40 nm, 150 nm.
- 42 (a) Optical picture of the fabricated Hall bar devices. Input voltage is applied from left to right along the Hall bar which the x direction. V_{xy} is measured along the y direction. (b) Measurement sequence of the experiment.
- 43 (a) Dependence of the transverse voltage V_{xy} on the input voltage V_{write} in the absence of external magnetic field along [10-10] and [11-20] of Mn₃Ge film. (b) transverse voltage V_{xy} versus input voltage V_{write} for Mn₃Ge/Pt sample and Mn₃Ge/Cu/Pt sample current flows along the [10-10] direction of the sample. Transverse voltage versus input voltage with read current flow along [10-10] direction in the absence of field with (c) different waiting time and (d) with different value.

-
- 44 Transverse voltage as the function of input voltage with read current flow along [10-10] direction, field along (a) [10-10] in-plane direction, (b) out-of-plane [0001] direction, (c) with field in different polarity.
- 45 (a) AHE measurement on 4-ferro switching hall bar with 1mA and 3mA read current and out-of-plane field. (b) switching measurement with 1mA and 3mA read current in the absence of field.
- 46 (a) AHE measurement and (b) switching measurement of 25 nm Mn₃Ge/ 4 nm Pt stack. (c) AHE measurement and (d) switching measurement of 150 nm Mn₃Ge/ 4 nm Pt stack.



List of Tables

- 1 Commonly used substrate data.



Abbreviations

AF	Antiferromagnetic
AFM	Atomic force microscopy
AHE	Anomalous Hall effect
AMR	Anisotropic magnetoresistance
ANE	Anomalous Nernst effect
ARPES	Angle-resolved photoemission spectroscopy
BZ	Brillouin zone
DC	Direct current
DMI	Dzyaloshinskii–Moriya interaction
EB	Exchange bias
EBE	Election beam evaporator
FM	Ferromagnetic
GMR	Giant magnetoresistance
HE	Hall effect
HM	Heavy metal
IP	In-plane
K-cell	Knudsen effusion cell
MBE	Molecular beam epitaxy
MOKE	Magneto-optical Kerr effect

MPMS	Magnetic property measurement system
MRAM	Magnetoresistive random access memory
MTJ	Magnetic tunnel junctions
NM	Non-magnetic
OP	Out-of-plane
PBN	Pyrolytic boron nitride
PID	Proportional–integral–derivative
PPMS	Physical property measurement system
Py	Permalloy
QAHE	Quantum anomalous Hall effect
QH	Quantum Hall
QHE	Quantum Hall effect
QL	Quintuple layer
QSH	Quantum spin Hall
QSHE	Quantum spin Hall effect
RBS	Rutherford backscattering spectrometry
REE	Rashba-Edelstein effect
RF	Radio frequency
RHEED	Reflection high-energy electron diffraction
SAF	Synthetic antiferromagnets
SHA	Spin Hall angle
SHE	Spin Hall effect
SOC	Spin-orbital coupling
SOT	Spin-orbit torque
SQUID	Superconducting quantum interference device

ST-FMR	Spin torque ferromagnetic resonance
STO	Strontium titanate
STT	Spin transfer torque
TI	Topological insulator
TRS	Time reversal symmetry
UHV	Ultra high vacuum
VdP	Van der Pauw
XRD	X-ray diffraction
XRR	X-ray reflectivity
YSZ	Yttria-stabilized zirconia
2D	Two dimensional
3D	Three dimensional



List of publications

1. **Zhang, J.**; Kostanovskiy, I.; Parkin, S. S. P. Investigation of spin hall effect in hexagonal Mn₃Ge thin films. (In preparation).
2. **Zhang, J.**; Kostanovskiy, I.; Jeon, J.; Parkin, S. S. P. Zero-field electrical switching of offcut Mn₃Ge films. (In preparation).
3. Bedoya-Pinto, A.; Liu, D.; Tan, H.; Pandeya, A. K.; Chang, K.; **Zhang, J.**; Parkin, S. S. P. Large Fermi-Energy Shift and Suppression of Trivial Surface States in NbP Weyl Semimetal Thin Films. *Advanced Materials* **2021**, 33, (21), 2008634.
4. Zang, Y.; Küster, F.; **Zhang, J.**; Liu, D.; Pal, B.; Deniz, H.; Sessi, P.; Gilbert, M. J.; Parkin, S. S. P. Competing Energy Scales in Topological Superconducting Heterostructures. *Nano Letters* **2021**, 21, (7), 2758-2765.



Acknowledgments

First of all, I would like to express my sincere gratitude to my Ph.D. supervisor, Prof. Dr. Stuart S.P. Parkin. I am grateful for his instruction on my research projects and his outstanding efforts in providing the state-of-the-art experimental environment here in Halle. When meeting with him, I can always learn from his knowledge of physics and get influenced by his passion for research. As a world-famous scientist, he is truly an example for me to learn how to carry out a research project, communicate with my colleague, and think beyond. I also want to acknowledge support from the China Scholarship Council (CSC) for four years study (No. 201606010347) at the Max Planck Institute of Microstructure Physics and the Martin Luther University Halle-Wittenberg.

Furthermore, I would like to thank Dr. Ilya Kostanovskiy for his support on my project. He taught me how to use the Quince MBE system and guided me to learn the art of MBE. He helped me a lot at the beginning of my career in Halle and carried out the RBS measurement for my samples. I am also thankful for the STM support provided by Dr. Kai Chang and Jingrong Ji. Dr. Winfried Heichler, Dr. Yunyi Zang, Dr. Jue Huang, Dr. Amilcar Bedoya Pinto, and Dr. Defa Liu offered mutual help on the chamber maintenance. I am also thankful for the efforts of the PPMS, MPMS, XRD, AFM, TEM, STM, ST-FMR, RBS managing team, cleanroom managing team, electric workshop, mechanic workshop, Haustechnik team, storage support team and other scientific support from my colleagues. I acknowledge Dr. James Mark Taylor, Dr. Binoy Krishna Hazra, Dr. Banabir Pal, Dr. Tianping Ma, Dr. Xilin Zhou, Dr. Peng Wang, Dr. Fan Li, Dr. Yicheng Guan,

Dr. Luxin Li, Dr. Jae-Chun Jeon, Ke Gu, Tianzhe Chen, Jiho Yoon for valuable scientific discussion. I want to thank Antje Paetzold, Simone Jäger, Michael Strauch, Dr. Ann-Kristin Flieger, and the administration division of the institute for their help on almost everything regarding the Institute administration and me living in Germany. Also thank Mike Borrmann and the IT team of the institute for their support on IT affairs.

Finally, I would like to express my deepest gratitude and love to my family, especially my parents and my wife. Without their emotional support and love, I would not make it today.

The Covid pandemic started in 2020 really changed my life and many other persons' life by taking the loved ones away from us unexpectedly, I hope we can get rid of the sorrow and live strong by carrying the love of the one we lost.

Curriculum Vitae

First name: Jibo

Last name: Zhang

Gender: Male

Education

- 2016 – 2024 Ph.D. in Physics
- Max-Planck Institute of Microstructure Physics, Halle (Saale),
Germany
- Martin Luther University Halle-Wittenberg, Halle (Saale),
Germany
- Supervisor: Prof. Stuart S.P. Parkin
- 2013 – 2016 Master in Physics
- Institute of Physics, Peking University, Beijing, China
- Supervisor: Prof. Furen Wang
- 2008 – 2012 Bachelor in Physics
- Institute of Physics, Shandong University, Jinan, China



Eidesstattliche Erklärung

Ich, Jibo Zhang, erkläre an Eides statt, dass ich die Arbeit selbstständig und ohne fremde Hilfe verfasst, keine anderen als die von mir angegebenen Quellen und Hilfsmittel benutzt und die den benutzten Werken wörtlich oder inhaltlich entnommenen Stellen als solche kenntlich gemacht habe.

Stadt, Datum

Jibo Zhang